UNDERSTANDING THE MECHANISMS OF DISSOLVED OXYGEN TRENDS AND VARIABILITY IN THE OCEAN

A Dissertation
Presented to
The Academic Faculty

by

Yohei Takano

In Partial Fulfillment
of the Requirements for the Degree
Doctor of Philosophy in the
School of Earth and Atmospheric Sciences

Georgia Institute of Technology
May 2016

COPYRIGHT© 2016 BY YOHEI TAKANO

UNDERSTANDING THE MECHANISMS OF DISSOLVED OXYGEN TRENDS AND VARIABILITY IN THE OCEAN

Approved by:

Dr. Takamitsu Ito, Advisor School of Earth and Atmospheric Sciences *Georgia Institute of Technology*	Dr. Annalisa Bracco School of Earth and Atmospheric Sciences *Georgia Institute of Technology*
Dr. Emanuele Di Lorenzo School of Earth and Atmospheric Sciences *Georgia Institute of Technology*	Dr. Curtis Deutsch School of Oceanography *University of Washington*
Dr. Joseph Montoya School of Biology *Georgia Institute of Technology*	

Date Approved: March 16th, 2016

ACKNOWLEDGEMENTS

First and foremost, I am extremely grateful to my advisor Takamitsu Ito for his continuous guidance and support during my graduate studies. He patiently gave me advice not only about conducting research but also about the importance of having my own story and philosophy as a scientist. I also wish to thank my committee members, Emanuele Di Lorenzo, Joseph Montoya, Annalisa Bracco, and Curtis Deutsch for their insights. It was a great honor for me talk and discuss science with all the prestigious people in our fields. I am particularly grateful for the influential collaboration with my co-researcher Curtis Deutsch. Finally, it has been a great pleasure to work with the ocean biogeochemistry group at Georgia Institute of Technology and I thank all the members in our group.

Being a graduate student at Colorado State University had a major influence on my scientific approach. Especially I would like to recognize the assistance that I received from Wayne Schubert, Thomas Birner, and David Thompson. I also thank all my friends in Colorado for sharing enjoyable times with me during my studies there.

Finally, I would like to thank all my family and friends in Japan, especially my parents, Nobuyuki and Hiroko Takano for all their encouragement and support, especially their insights into living in a new culture.

TABLE OF CONTENTS

Page

ACKNOWLEDGEMENTS iii

LIST OF TABLES vi

LIST OF FIGURES vii

SUMMARY xii

CHAPTER

1 INTRODUCTION 1

1.1 Why is dissolved oxygen important? 1

1.2 Basic mechanisms: ocean circulations and biology regulating oceanic oxygen cycle 2

1.3 Climatological descriptions of dissolved oxygen 7

1.4 Temporal characteristics of dissolved oxygen from observations and modeling 10

1.5 Objectives of this dissertation 12

2 INTERPRETING INTRASEASONAL VARIABILITY OF SUBSURFACE TRACERS OBSERVED BY A PROFILING FLOAT 14

2.1 Introduction 15

2.2 Description of the dataset 17

2.3 Causes of the observed intra-seasonal variability 24

2.4 Conclusion and discussion 35

3 MECHANISMS OF CENTENNIAL-SCALE TROPICAL PACIFIC OXYGEN TRANSITION UNDER THE ANTHROPOGENIC CLIMATE CHANGE 38

3.1 Introduction 39

3.2 Data and methods 42

3.3 CMIP5 Multi-Model Projections of global thermocline deoxygenation 52

3.4 Mechanisms of anthropogenic thermocline deoxygenation 61
3.5 Summaries and discussion 86

4 UNCERTAIN RESPONSE OF OPEN-OCEAN OXYGEN REFLECTS THE IMBALANCE BETWEEN VENTILATION AND REMINERALIZATION 88
4.1 Introduction 89
4.2 Apparent Oxygen Utilization balance in a two-box model 91
4.3 Design of sensitivity experiments 94
4.4 Results 95
4.5 Summary and implications to global warming response 106

5 SUMMARY AND FUTURE WORK 108
5.1 What could observations tell us about dissolved oxygen variability? 108
5.2 Understanding the mechanisms of centennial-scale dissolved oxygen transition in the tropical thermocline 110
5.3 Towards the better understanding on temporal spectrum of oceanic oxygen cycle 112

APPENDIX A: DETAILED INFORMATION ON SAMPLING FREQUENCY FROM FLOAT OBSERVATION 5143STNP 114

REFERENCES 115

LIST OF TABLES

Page

Table 2.1: Linear lag-correlation coefficients (from 5-day lag to 30-day lag) between Fast Fourier Transform based high-pass filtered dissolved oxygen in the main thermocline (150m depth) and surface properties. Cut-off frequencies are set to 1/30.4608 days^{-1} for the float data, 1/30 days^{-1} for mean sea level anomaly, and 1/32 days-^{1} for net primary production. 27

Table 2.2: The same as in Table 2.1 except for net primary production (*NPP*) (from 8-day to 48-day lag). 27

Table 3.1: CMIP5 modeling groups, institute ID, and model names. 43

Table 3.2: Spatial correlation coefficients (R) of thermocline oxygen between selected models and World Ocean Atlas 2009 (the first two rows). The bottom two rows show weighted-area mean thermocline oxygen anomalies based on the difference between selected models and World Ocean Atlas 2009. MITgcm is from control experiment. Spatial correlation coefficients and weighted area-mean values in the Pacific Ocean are based on Pacific domain covering the north of 25°S. 53

LIST OF FIGURES

Page

Figure 1.1: Climatological annual mean O_2 distributions on the surface ocean from the *World Ocean Atlas* 2009. 5

Figure 1.2: Climatological annual mean temperature distributions on the surface ocean from the *World Ocean Atlas* 2009. 5

Figure 1.3: Climatological annual mean oxygen saturation state ($O_{2,sat}$) distributions on the surface ocean from the *World Ocean Atlas* 2009. 6

Figure 1.4: Schematic depiction of water mass following the isopycnal layer. The schematic shows how O_2 changes along with ocean circulations through biological processes. 6

Figure 1.5: Annual mean climatology of O_2 at 400m from the *World Ocean Atlas* 2009.8

Figure 1.6: Vertical profiles of dissolved oxygen concentrations from the Pacific (PAC) and Atlantic (ATL) Oceans cited from *Talley et al.*, (2011). Data are from World Ocean Circulation Experiments (WOCE). 9

Figure 1.7: Time and spatial scales of physical oceanographic phenomena adapted from *Talley et al.*, (2011). Blue and red shadings target the temporal and spatial scales of O_2 variability and changes focused on in this research. 12

Figure 2.1: Float trajectory and satellite dynamic topography near the OSP. (a) Float trajectory is shown as black dots remaining very close to the location of OSP (50°N 145°W). Color shading is the depth of bottom topography from ETOPO1. The red line shows the longitude line corresponds to the horizontal axis in the Hovmöller diagram (b). (b) The Hovmöller diagram of mean sea-level anomalies from AVISO gridded satellite data. The Hovmöller diagram is based on daily mean sea-level anomalies and the time in vertical axis is consistent with float observational time (up to January 15th, 2010). Note that daily mean sea-level anomaly is covered up to January 2010. 20

Figure 2.2: Observed temporal variability of dissolved oxygen, nitrate, potential density and *AOU*. The left column (a-d) shows the vertical profile of standard deviation. The black line reflects the variability including all timescales including seasonal cycles, and blue dash-dot line reflects high-pass filtered data based on the Fast Fourier Transform method. The right column (e-h) shows the time-depth cross-sections. Black solid line marks the depth of mixed-layer base using potential density criteria [*de Boyer Montégut et al.*, 2004]. White shading in time-depth cross-sections shows low-quality data with instrumental error and missing values. 23

Figure 2.3: (a) Scatter plot between thermocline oxygen (dissolved oxygen at 150m depth) and isopycnal layer depth at $\sigma_\theta = 26.5$ and (b) oxygen and isopycnal layer depth at $\sigma_\theta = 26.5$. Bottom panels show scatter plot between (c) oxygen and spiciness at $\sigma_\theta = 26.5$ and (d) nitrate and spiciness at $\sigma_\theta = 26.5$. Fast Fourier Transform (FFT) based high-pass filter is applied to all the data in this figure. 30

Figure 2.4: Power spectrum of the observed a) dissolved oxygen in the main thermocline, b) nitrate in the main thermocline, c) salinity in the main thermocline, and d) isopycnal layer depth at $\sigma_\theta = 26.5$. Vertical colored dotted lines show possible aliased frequencies from inertial frequencies (blue dash line), M_2 (purple dash line), and K_2 (green dash line) tidal frequencies. Vertical black dash line is the cut-off frequency of 1/30 day^{-1}, which separates the high- and low-frequency band. Power spectrum is normalized by total variance. The red dashed spectral lines show the 95% significance lines estimated by red-noise spectrum based on *Gilman et al,* [1963]. 34

Figure 3.1: Time series of global mean sea surface temperature (SST) anomaly from selected CMIP5 models. SST anomalies are based on SST relative to the values at 1900 (shown as colored shapes). We used model ensemble mean SST anomaly (ENSEMBLE, black line) to conduct perturbation experiments (see method section for details). 45

Figure 3.2: Centennial changes (i.e. difference between pre-industrial mean (1900-1930) and RCP8.5 mean (2070-2100)) of zonal mean a) evaporation minus precipitation (E-P) [in mm/day] and b) zonal wind stress [in N/m^2] in the Southern hemisphere. c) Temporal evolution of equatorial Pacific zonal wind stress anomalies (relative to pre-industrial mean) [in N/m^2] defined as the weighted area-mean zonal wind stress anomalies in box region shown in d). 10-year low-pass filter is applied to time series in c). d) Centennial changes in tropical Pacific zonal wind stress [in N/m^2] from the ensemble mean of selected CMIP5 models (see main text and Table 3.1). 46

Figure 3.3: Spatial patterns of a) centennial changes (after 200 years) in evaporation minus precipitation (E-P) and b) and c) zonal wind stress (τ_x) used for perturbation experiments. Zonal wind stresses are from SAM regression based zonal wind stress and idealized perturbation for zonal wind stress changes in the tropical Pacific Ocean. 51

Figure 3.4: Comparison of climatological annual mean dissolved oxygen concentration [mmol/m^3] averaged in the depth range of the main thermocline (150m – 600m for CMIP5 models, 160m – 610m for MITgcm) from six selected CMIP5 Earth System Models, a MITgcm control experiment, and the World Ocean Atlas 2009. The model mean shows the multi-model mean dissolved oxygen concentration from the CMIP5 models. Climatology is based on the 30-year mean in the late 20th century (1970-2000). 54

Figure 3.5: Dissolved oxygen concentration changes under the RCP8.5 scenario from 1900-1930 to 2070-2100. Vertically averaged (150m – 600m, 160m – 610m for MITgcm-ALL) oxygen concentrations across the CMIP5 models are plotted. The MITgcm-ALL is based on the sensitivity experiment with all climatic trends forcing that mimics forced changes in the CMIP5 models. The red rectangle is the tropical Pacific domain used for defining our area-mean based metrics. 56

Figure 3.6: Oxygen saturation state changes under the RCP8.5 scenario from 1900-1930 to 2070-2100. Vertically averaged (150m – 600m, 160m – 610m for MITgcm-ALL) oxygen saturation across the CMIP5 models are plotted. MITgcm-ALL is based on sensitivity experiments with all climatic trends forcing mimicking forced changes in the CMIP5 models. 58

Figure 3.7: Apparent oxygen utilization changes under the RCP8.5 scenario from 1900-1930 to 2070-2100. Vertically averaged (150m – 600m, 160m – 610m for MITgcm-ALL) *AOU* across the CMIP5 models are plotted. MITgcm-ALL is based on sensitivity experiments with all climatic trends forcing mimicking forced changes in the CMIP5 models. 60

Figure 3.8: Temporal evolutions of global mean thermocline properties covering all longitude and latitudes, in 160 – 610m based on a suite of perturbation experiments (Red = warming, Blue = freshwater, Magenta = Southern Ocean wind, Dotted Magenta = Tropical trade wind, and Black solid = all forcing). (a) Dissolved oxygen, (b) oxygen saturation, and (c) apparent oxygen utilization (AOU) time series are all relative to the control experiment. All the properties are in the unit of mmol/m^3. Shadings show multi-model range, anomalies relative to average values from 1900-1930. Anomalies at 2100 are based on values relative to the preindustrial (1900-1930) mean from selected CMIP5 models shown as colored shapes. 62

Figure 3.9: The same as in Figure 3.8 except for tropical thermocline (covering the latitudinal range of 15°S to 15°N). 65

Figure 3.10: The same as in Figure 3.8 except for tropical Pacific thermocline (within the domain 159.5°E-80.5°W, 15.5°S-15.5°N shown as the rectangular box in Figure 3.5). 67

Figure 3.11: Fractional changes in the equatorial Pacific Ocean (between 4°S-4°N) export production at 100m (116m for MITgcm). Fractional changes are relative to the average values of export production from 1900-1930 for CMIP5 model outputs (in shadings). For the sensitivity experiments, fractional changes are based on differences from the control (Red = warming, Blue = freshwater, Magenta = Southern Ocean wind, Dotted Magenta = Tropical trade wind, and Black solid = all forcing). We applied 10-years of low-pass filter for all time series to focus on low-frequency changes in export production for CMIP5 model outputs. Fractional changes for selected CMIP5 models at 2100 are shown as colored shapes. 70

Figure 3.12: Global maps of thermocline ideal age tracer (vertical mean from 160m-610m) from a suite of sensitivity experiments. The CTL (top left panel) shows ideal age tracer from the control experiment. The rest of the panels (Warm, EmP, SAM, Trade, and ALL) show ideal age tracer anomalies (difference from CTL) from a suite of sensitivity experiments. 72

Figure 3.13: Ideal age distribution in the tropical and North Pacific Ocean from a suite of perturbation experiments on constant depth (at 435m). CTL (the left top panel) shows ideal age from the control experiment. The rest of the panels (Warm, E-P, SAM, Trade, and ALL) show ideal age anomaly relative to control experiment. 74

Figure 3.14: The same as in Figure 3.13, except for ideal age tracer on isopycnal layer (at $\sigma_\theta = 26.5$). The contour shows the isopycnal layer depth (mean values for CTL and anomaly from CTL for each sensitivity experiments). Note that color scale is different for Warm and ALL experiments. 75

Figure 3.15: Changes in isopycnal layer depth (at $\sigma_\theta = 26.5$, in the unit of meter) from a suite of sensitivity experiments and CMIP5 models (gray shadings). For the sensitivity experiments, isopycnal later depths are based on differences from the control (Red = warming, Blue = freshwater, Magenta = Southern Ocean wind, Dotted Magenta = Tropical trade wind, and Black solid = all forcing). Isopycnal layer depth changes for selected CMIP5 models at 2100 are shown as colored shapes. 77

Figure 3.16: Changes in dissolved oxygen concentration, oxygen saturation, and apparent oxygen utilization from ALL experiment relative to control experiment. Left panels show changes on constant depth (at 435m) and right panels show changes along the isopycnal ($\sigma_\theta = 26.5$). 80

Figure 3.17: Physically (ΔAOU_{phys}) and biologically (ΔAOU_{bio}) driven AOU from ALL experiment (relative to control experiment) after 200 years of model integration. Left panels show ΔAOU_{phys} and ΔAOU_{bio} at 435m and right panels show ΔAOU_{phys} and ΔAOU_{bio} along $\sigma_\theta = 26.5$. 83

Figure 3.18: A phase diagram explaining ΔAOU as the sum of ΔAOU_{phys} (x-axis) and ΔAOU_{bio} (y-axis) in the tropical Pacific Ocean (rectangular domain in Figure 3.4) after 200 years of model integration. Left panel shows ΔAOU_{phys} and ΔAOU_{bio} at 435m and right panel shows ΔAOU_{phys} and ΔAOU_{bio} along the isopycnal (σ_θ = 26.5). Weighted area-mean values from a suite of sensitivity experiments based on two different coordinates are plotted in colored dots. The non-linearity is negligibly small (compare filled and open black circle). Colored contour lines are the total ΔAOU (ΔAOU_{phys}+ ΔAOU_{bio}). The effects of the ocean heating and the trade wind explain most of the total ΔAOU. Note that x-axis ranges are different between the two panels. 84

Figure 4.1: Annual mean climatology of Apparent Oxygen Utilization (AOU) at 400m from the *World Ocean Atlas* 2009. 91

Figure 4.2: A schematic diagram of two-box model representing the O_2 and nutrient cycles. 92

Figure 4.3: Hypoxic (a and b) and suboxic volume (c and d) in the Pacific Ocean (north of 35S) and the Indian Ocean (north of the equator), upper 850m (similar to the analysis of *Duteil and Oschlies*, [2011]) from sensitivity experiments. Hypoxic and suboxic volumes are based on dissolved oxygen concentrations smaller than 20 mmol/m^3 and 5 mmol/m^3 following *Bianchi et al.*, [2012]. Green shadings show observed hypoxic and suboxic volume range from *Bianchi et al.*, [2012]. 96

Figure 4.4: Global maps of ΔO_2, $\Delta O_{2,sat}$, and ΔAOU from a suite of vertical diffusion experiments. Delta (Δ) refers to the anomaly from the control experiment. All the tracers are vertically integrated in the thermocline (160m-610m). Black boxes are the areas we are focusing on for calculating weighted-area mean values. 99

Figure 4.5: Sensitivity of thermocline $\Delta O_{2,sat}$ (red marks) and ΔAOU (blue marks) to various vertical diffusion coefficients in the eastern tropical Pacific Ocean (a) and the Indian Ocean (b). $\Delta O_{2,sat}$ and ΔAOU are base on weighted-area mean values in two regions (black boxes in Figure 4.4, top left panel). 101

Figure 4.6: The same as in Figure 4.5 except for ventilation and remineralization driven ΔAOU (ΔAOU_{phys} and ΔAOU_{bio}). 103

Figure 4.7: The same as in Figure 4.4 except for the thermocline water mass age (Δage), export production at 222m (Δepc), surface phosphate (ΔPO_4), and surface iron (ΔFe). 106

Figure A.1: The observational sampling time interval for float 5143StnP deployed in the Gulf of Alaska. 114

SUMMARY

A widely observed tracer in the field of oceanography is dissolved oxygen (O_2). A tracer crucial to ocean biogeochemical cycles, O_2 plays an active role in chemical processes, marine life, and ecosystems. Recent advances in observation and numerical simulation have introduced opportunities for furthering our understanding of the variability and long-term changes in oceanic O_2. This work examines the underlying mechanisms driving O_2 variability and long-term changes. It focuses on two distinct time-scales: intra-seasonal variability (i.e., a time scale of less than a month) and centennial changes in O_2. The first half of this work analyzes state-of-the-art observations from a profiling float in an investigation of the mechanisms driving the intra-seasonal variability of oceanic O_2. Observations from the float show enhanced intra-seasonal variability (i.e., a time scale of about two weeks) that could be driven by isopycnal heaving resulting from internal waves or tidal processes. Observed signals could result from aliased signals from internal waves or tides and should be taken into account in analyses of the growing observational dataset. The methods proposed in this study may be useful for future analyses of high-frequency tracer variability associated with mesoscale and sub-mesoscale processes.

Using outputs from state-of-the-art earth system models and a suite of sensitivity experiments based on a general circulation and biogeochemistry ocean model, the second half of this work focuses on investigating mechanisms regulating centennial changes in O_2. It explores the aspect of anthropogenic climate change (e.g., changes in the sea surface temperature and wind stress fields) that significantly impacts oceanic O_2, focusing specifically on tropical oxygen minimum zones. Results suggest that ocean heating induces a water mass shift, leads to decrease apparent oxygen utilization (*AOU*) in the tropical thermocline. The *AOU* decrease compensates the effect of decrease in oxygen saturation due to the ocean warming. Our sensitivity experiments show that both physically (i.e., age) and biologically (i.e., the oxygen utilization rate) driven *AOU* will contribute almost equally to controlling changes in oceanic O_2 in the next century. However, additional sensitivity experiments indicate that physically and biologically driven *AOU* balance has regional characteristics. We need to address the unanswered question of how varying large-scale oceanic circulations regulate this balance and answer fundamental questions that lead to a more comprehensive understanding of the mechanisms that control the variability and the future evolution of oceanic O_2.

CHAPTER 1

INTRODUCTION

1.1 Why is dissolved oxygen important?

One of the most widely observed quantities for studying physical and chemical oceanography is dissolved oxygen concentration (hereafter O_2). The third most frequently observed tracer following temperature and salinity, it has a long history of observations and measurements. O_2 reflects both physical and biological processes in the ocean and any changes in O_2 could directly influence the physiology of marine life [*Portner and Knust*, 2007; *Vaquer-Sunyer and Duarte*, 2008] and various redox reactions [*Morel and Price,* 2003], which could impact trace element cycles (e.g., iron (*Fe*), manganese (*Mn*), and molybdenum (*Mo*)) [*Schlesinger and Bernhardt,* 2013]. O_2 also reflects the cumulative effect of biological oxygen consumption and can be used as a non-conservative, passive tracer informing the characteristics of ocean circulation and water mass formation [*Talley et al.*, 2011]. Since the sources and sinks of O_2 in the surface ocean reflect air-sea gas exchange, photosynthesis and respiration, it is also widely used as a tracer of biological production. In the interior ocean, combined analysis of O_2 and other tracer measurements (such as inert gases) could provide a quantitative measurement of how much O_2 is produced by phytoplankton and consumed by microorganisms [e.g. *Emerson.et.al*, 2008, *Emerson and Bushinsky*, 2014]. Despite the various information O_2 provides, quantifying the mechanisms that regulate the temporal variability and changes in O_2 in the ocean remain unclear. This chapter begins by introducing the basic mechanisms and processes regulating O_2 in the ocean. It then attempts to explain the climatological spatial structures of O_2 based on modern observations and raises questions based on both observations and simulations.

1.2 Basic mechanisms: ocean circulations and biology regulating oceanic oxygen cycle

How does O_2 in the ocean change with the variability of ocean circulations? Theoretically, O_2 can be decomposed into two components, changes resulting from thermodynamics and from biological respiration. We first look at the thermodynamic effect. Dry mole fraction of atmospheric O_2 is approximately 21%, which supplies O_2 to the surface ocean through air-sea gas exchanges. O_2 at the surface depends on the ocean temperature and salinity (mainly driven by the temperature through the Henry's law), and it is generally close to saturation at the surface within a few percent. Figure 1.1 shows the annual mean climatology of O_2 at the surface. In brief, surface O_2 is inversely co-varies with the sea surface temperature gradients. Warm temperatures of the low latitudes decreases the O_2 solubility, and low temperatures of the mid to high latitudes increases it because cold water dissolves more gases (Figure 1.2). The annual mean climatology of the surface oxygen saturation ($O_{2,sat}$, calculated from temperature (T) and salinity (S)) [*e.g., Garcia and Gordon,* 1992] is very similar to that of the O_2 distribution at the surface (Figure 1.3).

The second component of O_2 change is biological consumption. Observational oceanographers estimate cumulative biological oxygen consumption (i.e., how much dissolved oxygen is utilized by respiration after the water mass last came into contact with the atmosphere) in the interior ocean using apparent oxygen utilization (*AOU*) [*Redfield*, 1958; *Broecker and Peng*, 1982]. *AOU* is defined as the difference between $O_{2,sat}$ and in-situ measurements of O_2, written as follows.

$$AOU = O_{2,sat} - O_2 \qquad (1.1)$$

Figure 1.4 shows a schematic diagram illustrating the processes changing O_2 following the water mass from the surface into the interior ocean. Again we assume that O_2 is very close to saturation at the surface (often supersaturated at the surface where production is high). In many ocean regions, this assumption is valid because the time scale of the air-sea equilibration of oxygen is relatively faster than the ocean circulation time scale [*Broecker and Peng*, 1982; *Ito et al.*, 2004; *Williams and Follows*, 2011] (Figure 1.4, corresponds to water mass parcel at time = t_1). While water masses are transported to the interior ocean as a result of subduction, dissolved oxygen is gradually depleted through degradation of organic matter (Figure 1.4, corresponds to water masses at time = t_1 to time = t_2, and t_3). The longer (i.e., increase in water mass age) water mass has traveled since its last contact with the atmosphere, the more biological consumption depletes dissolved oxygen in the water mass. Therefore, after removing the solubility effect, *AOU* reflects the accumulative effect of biological oxygen consumption. It is important to note that the concept of *AOU* may include errors in the estimation of biological oxygen consumption due to the degree of air-sea equilibrium at the time of water mass formation at the surface mixed layer [*Ito et al*., 2004; *Emerson and Hedges*, 2008].

Theoretically, the “true” oxygen utilization (*TOU*) rate is an accurate measurement of biological oxygen consumption in the ocean. *TOU* is defined as the difference between “preformed” oxygen and the observed dissolved oxygen concentration [*Broecker and Peng*, 1982; *Ito et al*., 2004, *Duteil et al*., 2013], written as follows.

$$TOU = O_{2,pre} - O_2 \qquad (1.2)$$

Preformed oxygen is the dissolved oxygen concentration just before the time of transportation into the interior ocean. It is basically the O_2 determined by thermodynamics, vertical mixing, and other surface mechanical processes such as the formation of bubbles and the direct injection of gas through these processes (Figure 1.4). Ideally, it will be useful to know the measurement of preformed oxygen, but observations cannot quantify the preformed values of chemical tracers. Despite the possible errors, *AOU* is still a widely used quantity to measure cumulative oxygen consumption using observational and model data. In this research, we frequently use the quantity $O_{2,sat}$ and *AOU* to understand the variability of O_2 in the ocean.

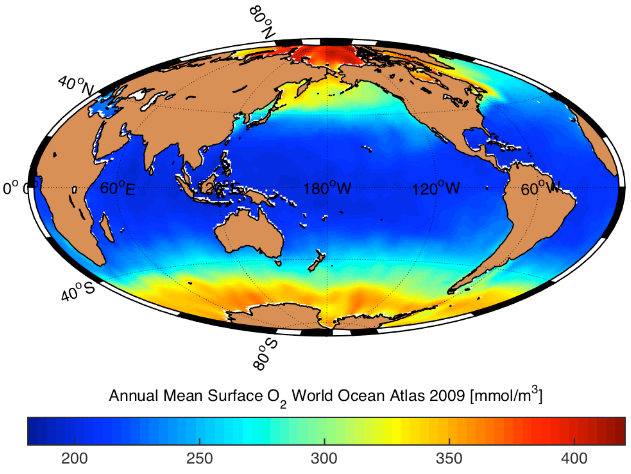

Figure 1.1. Climatological annual mean O_2 distributions on the surface ocean from the *World Ocean Atlas* 2009.

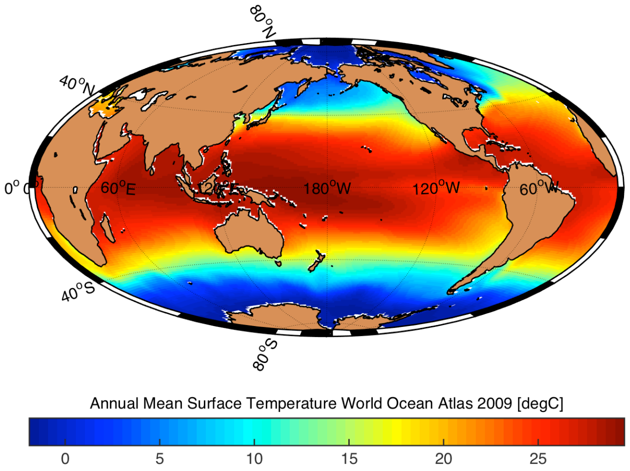

Figure 1.2. Climatological annual mean temperature distributions on the surface ocean from the *World Ocean Atlas* 2009.

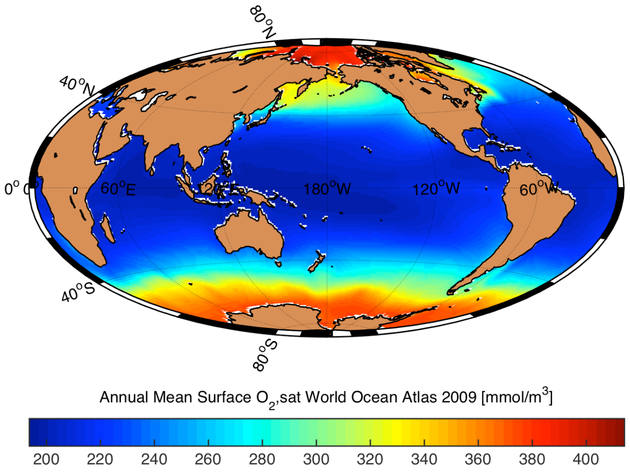

Figure 1.3. Climatological annual mean oxygen saturation state (*$O_{2,sat}$*) distributions on the surface ocean from the *World Ocean Atlas 2009*.

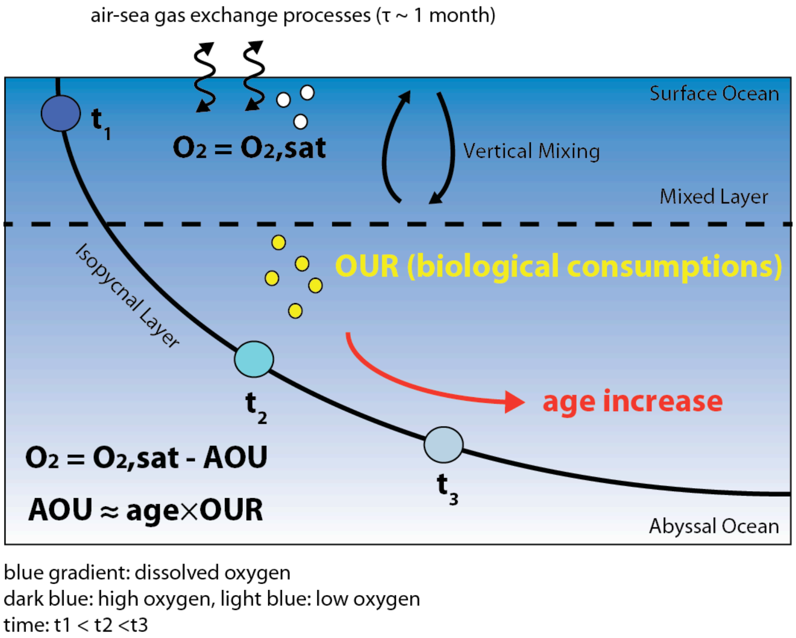

Figure 1.4. Schematic depiction of water mass following isopycnal. The schematic shows how *O_2* changes along with ocean circulations through biological processes.

1.3 Climatological descriptions of dissolved oxygen

Climatological distributions of O_2 at the surface (Figure 1.1) exhibit overall high O_2 in high-latitudes and low O_2 in mid to low-latitudes mainly reflecting the effect of temperature dependent solubility (but salinity also contributes to changes in solubility) in the surface ocean (Figure 1.3). Photosynthesis at the surface ocean also contributes as a source of O_2 in the surface ocean, thus super saturation of O_2 could occur in some regions.

Climatological distributions of O_2 in the interior ocean (here at 400m) show different patterns compared to the surface distributions (Figure 1.5). Low and high latitudes in the North Pacific Ocean are depleted in O_2. These oxygen deficient regions are called oxygen minimum zones (OMZs) and it occurs as a consequence of sluggish ocean circulations and active biological productivity and subsequent export of particulate organic carbon transport from the surface into the interior ocean [e.g., *Keeling et al*., 2010, *Wyrtki*, 1962]. These regions are characterized by high *AOU*, which reflects the long and high cumulative biological consumptions of O_2.

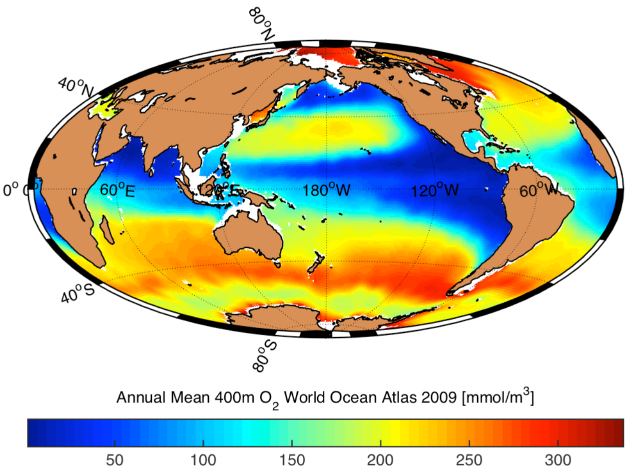

Figure 1.5. Annual mean climatology of O_2 at 400m from the *World Ocean Atlas* 2009.

Vertical structure of O_2 reflects the overall balance between the physical supply of O_2 and biological production and consumptions. Figure 1.6 shows the observed O_2 profiles from Pacific and Atlantic Oceans. The surface ocean is well oxygenated because of air-sea gas exchange and production from photosynthesis as we mentioned in the previous section. Vertical gradient of O_2 varies with latitudes, and minimum O_2 layers exist at about the depths of a few hundred meters. These low O_2 layers are typically the layers with high biological consumptions below the euphotic zone, where photosynthetic activity is prevented by light limitation. Tropical oceans and the North Pacific Ocean exhibit extremely intense O_2 minimum layers compared to other regions because of the old water mass age. Deep circulations supply oxygenated water mass from the polar surface oceans, so newly formed deep waters are generally well oxygenated. Historically Klaus Wyrtki studied a simple balance between vertical transport and simple parameterization of export production [*Wyrki*, 1962]. This study gave us an explanation of one-dimensional steady state balance explaining the vertical profile of O_2. The steady state distributions of O_2 are well studied but the temporal variability of O_2 has not been well sampled and understood yet. In the next sub section, we will briefly review our current understanding on temporal variability of O_2 from observations and numerical simulations.

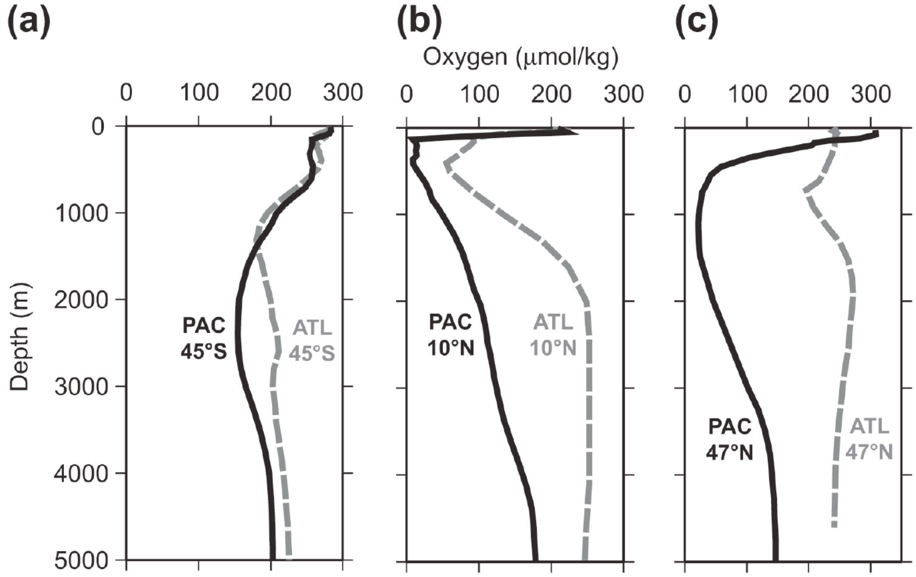

Figure 1.6. Vertical profiles of dissolved oxygen concentrations from the Pacific (PAC) and Atlantic (ATL) Oceans cited from *Talley et al.*, (2011). Data are from World Ocean Circulation Experiments (WOCE).

1.4 Temporal characteristics of dissolved oxygen from observations and modeling

Large-scale measurements of O_2 have been conducted across the major ocean basins [e.g., *Boyer et al*., 2014], and modern climatological maps of O_2 and associated physical biogeochemical quantities (e.g., temperature, salinity, dissolved oxygen, and nutrients) have been constructed using objective analysis methods. Some of the ocean stations in the major ocean basins have a long-term observation for decades of O_2 [e.g., *Whitney et al*., 2007*; Watanabe et al*., 2008]. Previous studies have found a long-term trend in O_2 [e.g., *Helm et al*., 2011; *Stramma et al*., 2008; *Whitney et al*., 2007] and possible connection to low-frequency climate variability from observational measurements [e.g., *Deutsch et al*., 2011*; Watanabe et al*., 2008*; Ito and Deutsch*, 2010]. In centennial time scale, anthropogenic climate changes could affect marine oxygen cycle through modification in both physical processes and biogeochemical processes. Global warming and associated changes in surface temperature is one of the most dominant climatic forcing, which could impact on ocean biogeochemical cycles and stress marine ecosystems over the centuries [*Gruber*, 2011]. The state-of-the-art Earth System Model (ESM) projections exhibit an overall decrease in O_2 in the ocean. The brief explanations on physical and biogeochemical mechanisms regulating so-called ocean deoxygenation are following. Global warming raises temperature in the ocean, leading to a decreasing O_2 solubility of seawater. In addition to this thermodynamic effect, warming of upper oceans increases the stratification, reducing the vertical supply of surface oxygenated water into the deep ocean. The combination of these two factors is hypothesized to cause the global-scale decline of O_2. Ocean deoxygenation could directly stress ocean biogeochemical cycles and marine ecosystem, along with ocean warming and acidification [*Gruber*, 2011]. O_2 constrains the habitat of marine organisms and the expansion of OMZs (and associated increase in hypoxic and suboxic volumes) could stress marine organisms [*Deutsch et al*., 2015; *Keeling et al*., 2010; *Vaquer-Sunyer and Duarte*, 2008]. However, it is challenging to access centennial changes of O_2 and other marine biogeochemical tracers from current observations. Ship-based measurements are still limited in temporal and spatial resolutions and it is difficult to capture various processes influencing the oceanic oxygen variability, including episodic events, impact of meso-scale eddies, the detailed structure of seasonal cycles, intra-seasonal variability, and inter-annual variability. Figure 1.7 shows a schematic diagram representing various oceanic processes and associated time scales. Short-term (within couple of days) to centennial scale climate and oceanic variability could impact on oceanic oxygen cycle in different time scales, which complicates the detection of specific signals from limited observations of marine biogeochemical tracers. Recent development and improvement in observations and numerical models could open a new window to observe and investigate those short time scale and centennial time scale changes in O_2 and other biogeochemical tracers. What is the recent advance in observations? What can we assess from modern observations and model predictions? What are the mechanisms driving short-term variability and centennial changes of O_2 in the ocean?

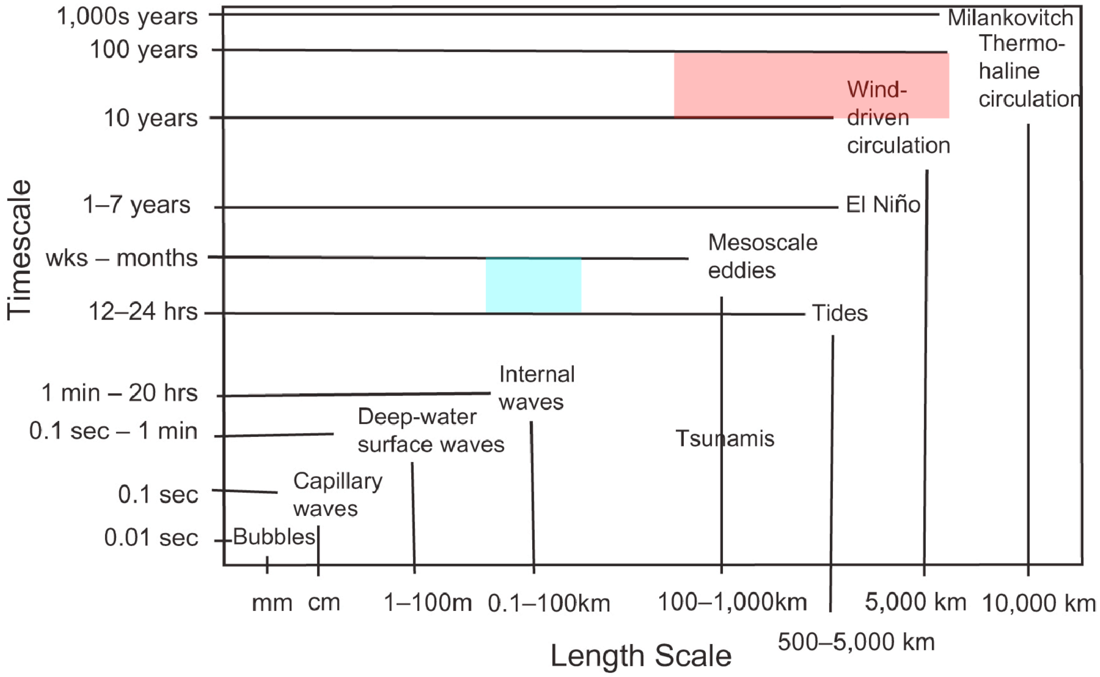

Figure 1.7. Time and spatial scales of physical oceanographic phenomena adapted from *Talley et al.*, (2011). Blue and red shadings target the temporal and spatial scales of O_2 variability and changes focused on in this research.

1.5. Objectives of this dissertation

This work examines the temporal and spatial variability of O_2 using both observations and a hierarchy of models. Here we focus on two distinct time scales. As shown in Figure 1.7, we have new opportunities to investigate the high-frequency variability (corresponds to blue shading in Figure 1.7, time scales less than the seasonal cycle) of O_2 (and other physical and chemical tracers) from recent observations from autonomous platforms. Chapter 2 begins by presenting the results of statistical analyses based on float observations and satellite data, and then discuss what recent observations have revealed about high-frequency variability and possible mechanisms driving the observed variability. Chapter 3 examines O_2 changes on a centennial time scale (corresponds to red shadings in Figure 1.7). To investigate how O_2 responds to centennial time scale climate changes (focusing on the anthropogenic climate changes), we analyze future projections from Earth-system models (ESMs). In addition, to investigate the background mechanisms regulating the centennial transition of O_2, we use a combination of the analysis of state-of-the-art ESM predictions and sensitivity experiments based on ocean biogeochemistry and general circulation model (OBGCM). Our discussion mainly focuses on O_2 changes in the tropical OMZs. To thoroughly understand the behavior of O_2 in the tropical OMZs, Chapter 4 presents the results of several sensitivity experiments with varied background vertical diffusivity. The experiments yield information about how physical and biological AOU changes as vertical diffusivity changes. Chapter 5 summarizes our results and future work.

CHAPTER 2

INTERPRETING INTRASEASONAL VARIABILITY OF SUBSURFACE TRACERS OBSERVED BY A PROFILING FLOAT

Published as

[1] Takano, Y., Ito, T., Deutsch, C., and Johnson, K. S. (2014), Interpreting intraseasonal variability of subsurface tracers observed by a profiling float, *Journal of Geophysical Research: Oceans*, 119(1), 288-296.

Abstract

Recent developments in autonomous biogeochemical instruments can provide new opportunities for investigating biogeochemical variability at unprecedented temporal resolutions. Early studies indicate the importance of relatively rapid and small-scale processes on biogeochemical variability. This chapter focuses on analyzing a profiling float deployed in the eastern subpolar North Pacific, showing significant intra-seasonal variability in potential density, oxygen and nitrate. We find substantial variability for all tracers in the main thermocline at a depth of about 150 m, indicating a common mechanism. A strong linear correlation between the intra-seasonal variability of isopycnal oxygen and nitrate (on $\sigma_\theta = 26.5$ surface) with isopycnal spiciness indicates the role of physical transport and mixing. Power spectrum analysis shows a statistically significant spectral peak of about 1/(18 days) for observed tracers in the main thermocline. This high-frequency variability does not show any significant relationship

with independent satellite measures of relevant physical and biological properties. With approximately five-day sampling periods, this spectral peak could be produced by aliasing of the inertial and tidal frequencies, rather than true intra-seasonal variability. The low-frequency component (>30 days) shows the spectral slope of ω^{-2} consistent with the stochastic null hypothesis. The growing number of autonomous biogeochemical observations will likely open up considerable opportunities for further research, and the analytical approaches in this study will be useful for a further analysis of temporal variability of biogeochemical tracers.

2.1 Introduction

Our understanding of oceanic tracer variability has mostly been based on ship measurements that provide accurate time-series observations on seasonal and longer timescales [e.g., *Ono et al*., 2001, *Whitney et al*., 2007, *Watanabe et al*., 2008]. The recent development of autonomous platforms such as profiling floats and gliders equipped with biogeochemical and bio-optical sensors provide a new opportunity for investigating biogeochemical variability at unprecedented temporal resolutions [*Bishop* 2009; *Roemmich et al*., 2004; *Emerson et al*., 2008; *Nicholson et al*., 2008; *Johnson et al*., 2009; *Ravichandran et al*., 2012]. These platforms will provide new information that can lead to a further understanding of physical and biogeochemical processes, particularly at shorter timescales. With frequent profiling, autonomous sensors can capture episodic events that could be missed by less-frequent ship-based observations. Episodic biological events can be triggered by an injection of macronutrients into the sun-lit euphotic layer

[*McGillicuddy et al*., 1998, 2003, 2016] or by rapid stratification changes in light-limited conditions by mesoscale and sub-mesoscale processes [*Taylor and Ferrari*, 2011; *Mahadevan et al*., 2012, 2016]. Profiling floats with oxygen and nitrate sensors have been used to monitor net community production for several seasonal cycles including episodic injections of macronutrients into the euphotic layer [*Riser and Johnson*, 2008, *Johnson et al*., 2010]. *Nicholson et al.* [2008] used Seagliders equipped with oxygen sensors and identified the response of local biological productivity to the heaving of the isopycnal layer generated from a mesoscale eddy in the oligotrophic subtropical North Pacific ocean. These early studies highlight the importance of high-frequency measurements that capture the impact of relatively rapid and small-scale processes such as mesoscale and sub-mesoscale eddies on the variability of phytoplankton productivity and biogeochemical cycles.

An increasing data stream from ongoing and future deployments of biogeochemical sensors also requires developments in suitable statistical methods for data diagnostics and interpretation. There are a number of high-frequency processes in the oceans whose biogeochemical implications are not fully understood. Here we define high-frequency variability as having a timescale less than a month. What are the characteristics of the high frequency biogeochemical variability? How can we distinguish biogeochemical signals from physical variability? The objective of this study is to analyze and interpret the short-timescale variability of observed tracers in the subsurface ocean. In particular, we focus on the time-series observations of dissolved oxygen, nitrate, temperature, and salinity on a profiling float deployed in the eastern subpolar North Pacific. The float was deployed near the long-term biogeochemical time series at Ocean

Station P (50°N, 145°W) [*Whitney et al*., 2007] and the float data have been validated against those ship-based observations. Furthermore, some aspects of subsurface oxygen variability at this site have been analyzed on the seasonal and longer timescales [*Cummins and Masson*, 2012]. In this study, we apply a sampling theory to the float time-series data and suggest an interpretation for the apparent high-frequency variability. We discuss implications of our results for the interpretation of the observed temporal spectrum.

2.2. Description of the dataset

We investigate observations from an Apex profiling float, equipped with oxygen (Aanderaa) and nitrate (ISUS) instruments, deployed in the Gulf of Alaska, [*Johnson and Coletti*, 2002; *Johnson et al*., 2013]. An ISUS nitrate sensor and an Aanderaa dissolved oxygen optode sensor are integrated into the body of a Teledyne/Webb Research Apex profiling float whose measurement accuracies have been evaluated in previous studies [*Körtzinger et al*., 2005; *Sakamoto et al*., 2009]. We choose one particular float (float #5143) for analysis based on its trajectory, which remained within 150 kilometers of Ocean Station P (hereafter, OSP) for the observed period [*Johnson et al*., 2013]. Thus, we have excellent reference data from OSP. The oxygen data exhibit no evidence of drift, and their climatological profile is consistent with the existing OSP data. Manufacturer measurement accuracy for the optode sensor is 10 μM. The sensors for oxygen and nitrate were recalibrated at deployment by means of a linear regression between the sensor data and data collected on a hydrocast at the same station [*Johnson et al*., 2013].

The recalibrated data appears accurate to within 1 μM for nitrate and 2 μM for oxygen. The data, which contains a three-year time series from September 2008 to August 2011, includes 214 vertical profiles of dissolved oxygen, nitrate, and CTD data collected in approximately five-day intervals with observations at 60 depths. Low-quality data with instrumental error and missing values are removed from our analysis.

Figure 2.1a shows the float trajectory and ocean topography from ETOPO1 [*Amante and Eakins*, 2009]. Although the float stays close to OSP (within a 150 km), this region is characterized by a quasi-stationary zonal gradient in mean sea level anomaly and the east-west slope of the main thermocline (isopycnal layer for $\sigma_\theta = 26.8$ [*White and Tabata*, 1987]). This results in the drift of the float to the west in observed period. The float parks at a depth of about 1,000m and gathers a water column profile as it ascends towards the surface at five days plus four hours (5.17 days) intervals (the float cycle is set for five days and four hours so it samples day and night, but there is some variability in that because the float does not try to control ascent rate exactly). The sampling time period ranges from five days to six days with the mean of 5.0768 days and the standard deviation of 0.18552 days (the variability of the sampling time period is shown in the Appendix A). For each profile, the float takes 60 measurements of dissolved oxygen, and nitrate (5 m resolution in the upper 100 m and 10 m resolution from 100 to 360 m). Temperature and salinity are collected in 2 m resolution, although the analysis reported here used a data set decimated to the same resolution as oxygen and nitrate. When the float reaches the surface, it transmits the data to communications satellites and then backs up to a data center located on the shore. Then the float returns to its parking depth for the next five-day interval. Figure 2.1b shows the variability of near-surface geostrophic circulation during the observation period of the float, as measured by the satellite mean sea level anomaly (*MSLA*) at 50°N, taken from the archiving, validation, and interpretation of satellite oceanographic data (AVISO)-gridded satellite observation data set (http://www.aviso.oceanobs.com/en/**).** The data show that this region is relatively quiescent and that it has no significant sign of an intra-seasonal variability in the *MSLA* data. During the course of observational period, no Rossby wave propagation is detected but quasi-stationary positive anomalies (*MSLA* ~ 6 cm) appear over the 145°W to 140°W longitude every six months. The 145°W line is the boundary between the negative anomaly in the east and the positive anomaly in the west.

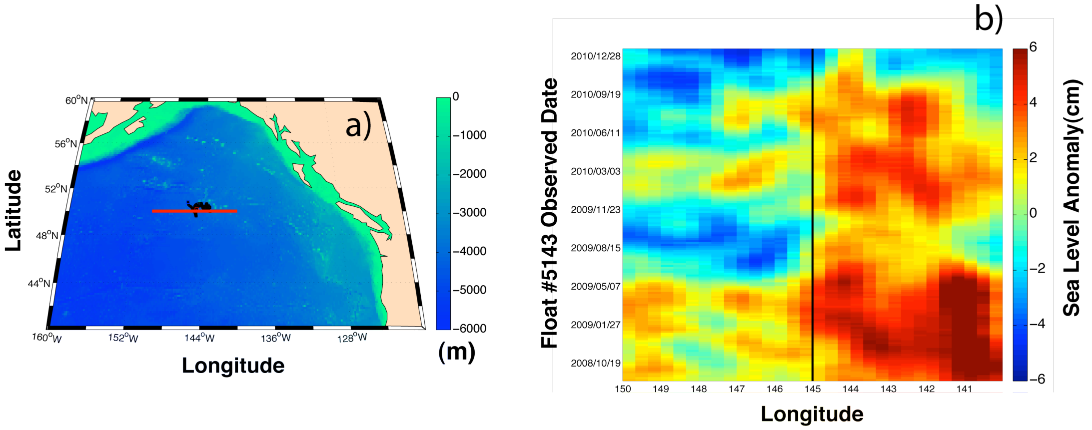

Figure 2.1. Float trajectory and satellite dynamic topography near the OSP. (a) Float trajectory is shown as black dots remaining very close to the location of OSP (50°N 145°W). Color shading is the depth of bottom topography from ETOPO1. The red line shows the longitude line corresponds to the horizontal axis in the Hovmöller diagram (b). (b) The Hovmöller diagram of mean sea-level anomalies from AVISO gridded satellite data. The Hovmöller diagram is based on daily mean sea-level anomalies and the time in vertical axis is consistent with float observational time (up to January 15th, 2010). Note that daily mean sea-level anomaly is covered up to January 2010.

Observed tracers exhibit interesting features, particularly in the main thermocline below the winter mixed-layer base (Figure 2.2). Figures 2.2e – 2.2h show the time-depth cross-sections of dissolved oxygen, nitrate, potential density, and apparent oxygen utilization (*AOU*) in the upper 200 m of the water column. *AOU* is calculated from the temperature, salinity, and oxygen data from the float using the oxygen saturation value of *Garcia and Gordon* [1992]. The black solid line marks the depth of the mixed layer, whose detection is based on potential density criteria ($\sigma_\theta = 0.03$) [*de Boyer Montégut et al.*, 2004]. The Hovmöller diagram reveals the seasonal cycle in the mixed layer. Dissolved oxygen and *AOU* in Figures 2.2e and 2.2h show that during the fall and the winter, all tracers are well homogenized in the mixed layer because of strong vertical mixing. In the winter, the mixed-layer depth can penetrate to a maximum of 114 m.

During the summer, convective mixing is suppressed because of the enhanced stratification, and active photosynthesis depletes nitrate and produces oxygen in the mixed layer. The observed three seasonal cycles are consistent with those of long-term datasets based on ship-based measurements that has been used to analyze seasonal and longer timescale variability [*Whitney et al.*, 2007; *Watanabe et al.*, 2008].

Temporal evolutions of potential density and chemical tracers show the signatures of relatively rapid, intra-seasonal variability below the mixed-layer base at depths of around 100-150 m (see Figures 2.2e-h). This high-frequency variability appears in all tracers and can be quantified using a high-pass filter. We apply two different approaches based on a running mean filter and a filter based on Fast Fourier Transform (FFT) method. A running mean method first calculates the low-frequency component of the data with a moving averaging window. The high-frequency component is then determined as the difference between the full time series and its low-frequency component. Alternatively, the FFT filter can be applied to the time series to extract the high-frequency component. Both methods require a subjective definition of the high-frequency signal. In the FFT method it is the cut-off frequency, and in the moving average method, it's the size of the averaging window for the running mean. In both cases, we choose a 30-day cutoff threshold. Prior to the application of filtering, we remove missing data and slight irregularity in the sampling interval by interpolating the data onto evenly spaced 5.0768 days time intervals based on the statistics of the sampling time interval. The simpler, running-mean method does not perfectly separate the high and low frequency signals. We calculated the standard deviation (hereafter, SD) of tracers as a function of depth (Figures 2.2a-d) for the raw data (including all frequencies) and the high-frequency component of the time series. Comparing the two filtering methods, we find virtually no significant difference in the SD profiles. The largest SD occurs below the mixed-layer base in the main thermocline for all profiles. Hereafter, we use the FFT method for separating low- and high-frequency variability for the statistical analysis. The raw data, including all of the frequencies, exhibit significant variance just below the winter mixed layer in the main thermocline. The maximum SD of dissolved oxygen is 51.5 μmol kg^{-1} and for nitrate is 5.5 μM. Peaks of the SD for both dissolved oxygen and nitrate are observed at around 120 m depths (Figures 2.2a and b, black solid line), near the bottom of the winter mixed layer. The float is drifting westward in the observed period and this region is characterized by a zonal slope of the isopycnals as mentioned in the previous paragraph. This westward drift of the float results in crossing the zonal slope of the main thermocline, which could result in the large magnitude of SD of tracers at around 120 m depth. Calculating SD using the subdivided dataset supports this possibility (SD profiles for subdivided data are in the auxiliary materials). The high-frequency band also shows this peak with a smaller SD of 17.8 μmol kg^{-1} for dissolved oxygen and 2.1 μM for nitrate using the FFT filtering method based on interpolated data, occurring slightly above the peak of the raw data. Running mean filtered data show virtually the same results, shown in Figure 2.2a and b. Approximately 10% of the tracer variance is in the high-frequency band in the main thermocline. Similar to the chemical tracers, the profile of potential density variance in the high-frequency band also peaks in the main thermocline, except another peak at the surface is associated with the seasonal cycle. Next, we will investigate the potential causes of the observed high-frequency variability.

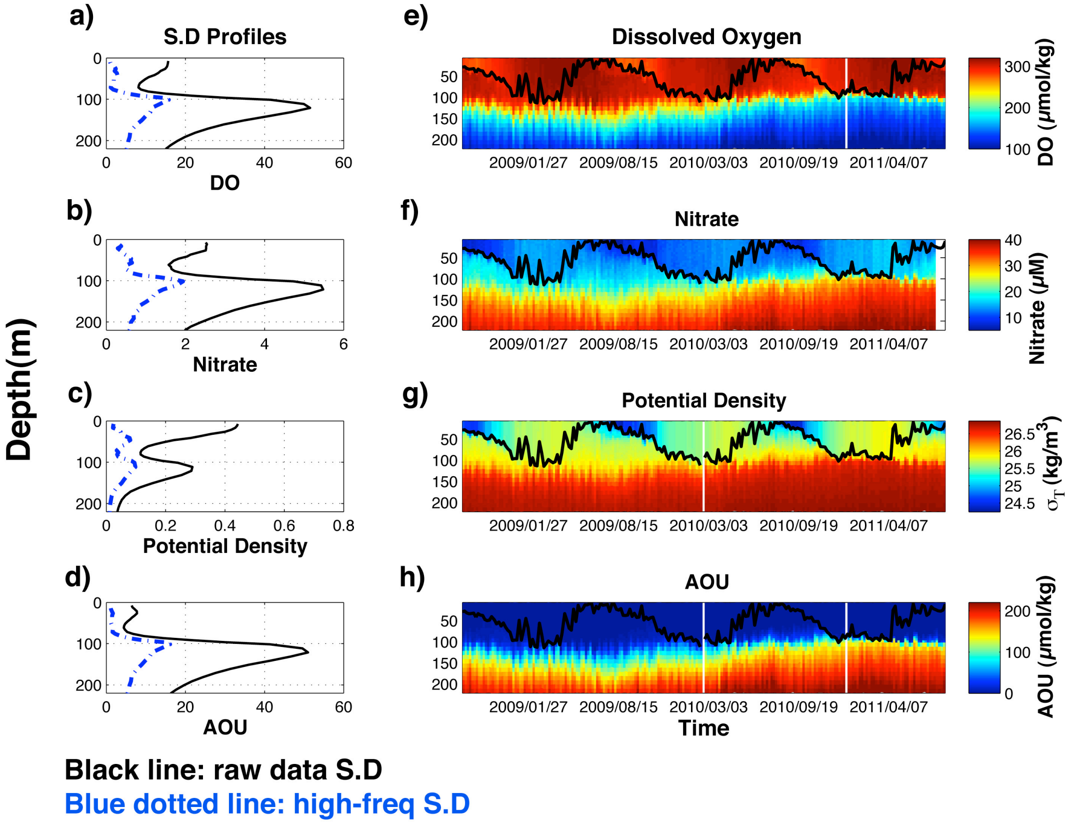

Figure 2.2. Observed temporal variability of dissolved oxygen, nitrate, potential density and *AOU*. The left column (a-d) shows the vertical profile of standard deviation. The black line reflects the variability including all timescales including seasonal cycles, and blue dash-dot line reflects high-pass filtered data based on the Fast Fourier Transform (FFT) method. The right column (e-h) shows the time-depth cross-sections. Black solid line marks the depth of mixed-layer base using potential density criteria [*de Boyer Montégut et al.*, 2004]. White shading in time-depth cross-sections shows low-quality data with instrumental error and missing values.

2.3 Causes of the observed intra-seasonal variability

The high-frequency fluctuation of biogeochemical tracers on timescales less than one month has not yet been identified and characterized in this region. Subsurface oxygen and nutrient variability may be influenced by the circulation and water mass structures and/or by biological processes. Here, we access satellite datasets to diagnose the high-pass filtered time series of tracers in the main thermocline using correlation analysis. Then we perform spectral analysis to characterize the temporal variability.

2.3.1 Attribution of observed variability

Given that this high-frequency variability appears in all tracers in the upper main thermocline, we hypothesize that a common physical mechanism exists. To test this hypothesis, we first conduct linear lag-correlation analyses between the float data and a suite of relevant physical and biogeochemical parameters including satellite-derived net primary production (*NPP*), dynamic topography, sea surface temperature (*SST*), and mixed-layer depth (*MLD*). We employ mean sea level anomalies from the AVISO-gridded dataset and the net primary production based on the vertically generalized production model (hereafter, VPGM) [*Behrenfeld and Falkowski*, 1997], obtained from the Oregon State University Ocean Productivity website (http://science.oregonstate.edu/ocean.productivity/index.php). The *NPP* dataset is based on moderate resolution imaging spectroradiometer (MODIS)-aqua derived surface chlorophyll concentrations, *SST*, and cloud-corrected incident daily photosynthetically active radiation (PAR). We constructed the area mean values of the *MSLA* and *NPP* indices in the vicinity of OSP as a proxy of ocean circulation and biological activity. We also examine correlations with the *SST*, surface oxygen, surface nitrate, and *MLD* anomalies from the float observations, which may influence biological productivity at OSP. Since the time interval of satellite based *NPP* is eight-day, we have binned the float data to a five day-interval to conduct statistical analysis. We applied a high-pass filter to all of the datasets before conducting a linear correlation analysis. We used Student's t-test for estimating statistical significance (testing the null hypothesis whether the correlation coefficient is significantly different from zero) of correlation coefficients using the formula below,

$$t = r\sqrt{\frac{n^* - 1}{1 - r^2}} \qquad (2.1)$$

where r is the correlation coefficient and n^* is the effective sample size estimated using *Bretherton et al*., (1999) formula:

$$n^* = n\frac{1 - r_1 r_2}{1 + r_1 r_2} \qquad (2.2)$$

The n is the number of samples and r_1 and r_2 are the lag-one autocorrelation for each time series. Tables 2.1 and 2.2 present the results of the lag-correlation analyses of the subsurface dissolved oxygen index in the main thermocline (at 150m depth) and the surface properties (*MSLA*, *NPP*, *SST,* surface oxygen, surface nitrate and *MLD*). The results show no statistically significant relationship between the subsurface oxygen and surface properties with lags of up to 30 days (48 days for *NPP*). The lack of correlations with the suite of physical and biological properties indicate that the observed high-frequency variability cannot likely be attributed to changes in ocean productivity or changes in geostrophic circulation, as indicated by satellite productivity and *MSLA* anomalies.

Table 2.1. Linear lag-correlation coefficients (from 5-day lag to 30-day lag) between Fast Fourier Transform based high-pass filtered dissolved oxygen in the main thermocline (150m depth) and surface properties. Surface properties include mixed layer depth (*MLD*), sea surface temperature (*SST*), surface oxygen (O_2), surface nitrate (NO_3), and mean sea level anomaly (*MSLA*). (b) The bottom table is the same as the top table except for *NPP* (from 8-day lag to 48-day lag). Correlation coefficient with underline indicates correlation coefficient significant at the 95% level (or higher) based on Student's t-test. Cut-off frequencies are set to 1/30.4608 days^{-1} for the float data, 1/30 days^{-1} for mean sea level anomaly, and 1/32 days-^{1} for net primary production.

SURFACE PROPERTIES	5-DAY LAG	10-DAY LAG	15-DAY LAG	20-DAY LAG	25-DAY LAG	30-DAY LAG
MLD	-0.13	-0.11	0.18	0.06	-0.22	0.03
SST	-0.04	-0.01	-0.03	-0.03	0.12	0
SURFACE O_2	-0.21	0.07	0.1	0.03	-0.16	0.06
SURFACE NO_3	-0.03	0.09	0.09	-0.1	-0.14	0.13
MSLA	0.03	0	-0.06	0.03	-0.02	0.02

Table 2.2. The same as in Table 2.1 except for net primary production (*NPP*) (from 8-day to 48-day lag).

SURFACE PROPERTIES	8-DAY LAG	16-DAY LAG	24-DAY LAG	32-DAY LAG	40-DAY LAG	48-DAY LAG
NPP(8-DAY)	-0.08	-0.2	0.21	0.16	-0.14	0.09

To investigate the effect of circulation and water mass changes, we conducted statistical analysis on a constant density surface using the time series data from the same float. Observed tracers are linearly interpolated on constant a density layer. Figure 2.3a shows a scatter plot of the high-pass-filtered dissolved oxygen in the main thermocline (150 m) and variation in the isopycnal layer for $\sigma_\theta = 26.5$. The reason we have chosen 150 m depth instead of 125 m depth (where SD peak occurs) is to ensure that we are analyzing the tracer variability in the main thermocline and to completely avoid the mixed layer. The high-frequency variability of dissolved oxygen at the constant depth is strongly correlated with the depth of the constant density ($\sigma_\theta = 26.5$) surface (r = 0.80, 95% significant based on t-test). The regression coefficient between thermocline oxygen and isopycnal depth is 1.32 (μmol kg^{-1}) m^{-1}, reflecting the local, vertical gradient of climatological oxygen, which indicates that the observed variability contains a strong influence of isopycnal heaving [*Cummins and Masson*, 2012]. A downwelling motion can transport relatively well-oxygenated water to a deeper depth where mean oxygen concentration is lower, generating a positive oxygen anomaly. The same circulation also deepens the isopycnal layer, leading to a positive correlation between the layer and the oxygen anomaly. These results also indicate that the correlation diminishes when evaluated on the isopycnal coordinate (Figure 2.3b) (r = -0.13, 95% significant based on t-test but very small correlation). Since it is difficult to directly determine the effect of horizontal transport based on a single float, we use spiciness as a proxy for advection and/or turbulent mixing. Spiciness is equivalent to salinity on the isopycnal layer, which can mark the water masses and also be transported by the circulation along isopycnal layers. Figure 2.3c and d show the scatter plots between high-pass filtered oxygen, nitrate, and spiciness on the isopycnal layer ($\sigma_\theta = 26.5$). There is a weak but significant linear correlation between the high-pass frequency variability of oxygen and spiciness ($r = 0.41$, 95% significant based on t-test) and a significant linear correlation between high-frequency variability of nitrate and spiciness ($r = -0.79$, 95% significant based on t-test). These results indicate that the ocean circulation and/or water mass changes could be the secondary mechanism controlling the high-frequency variability of tracers.

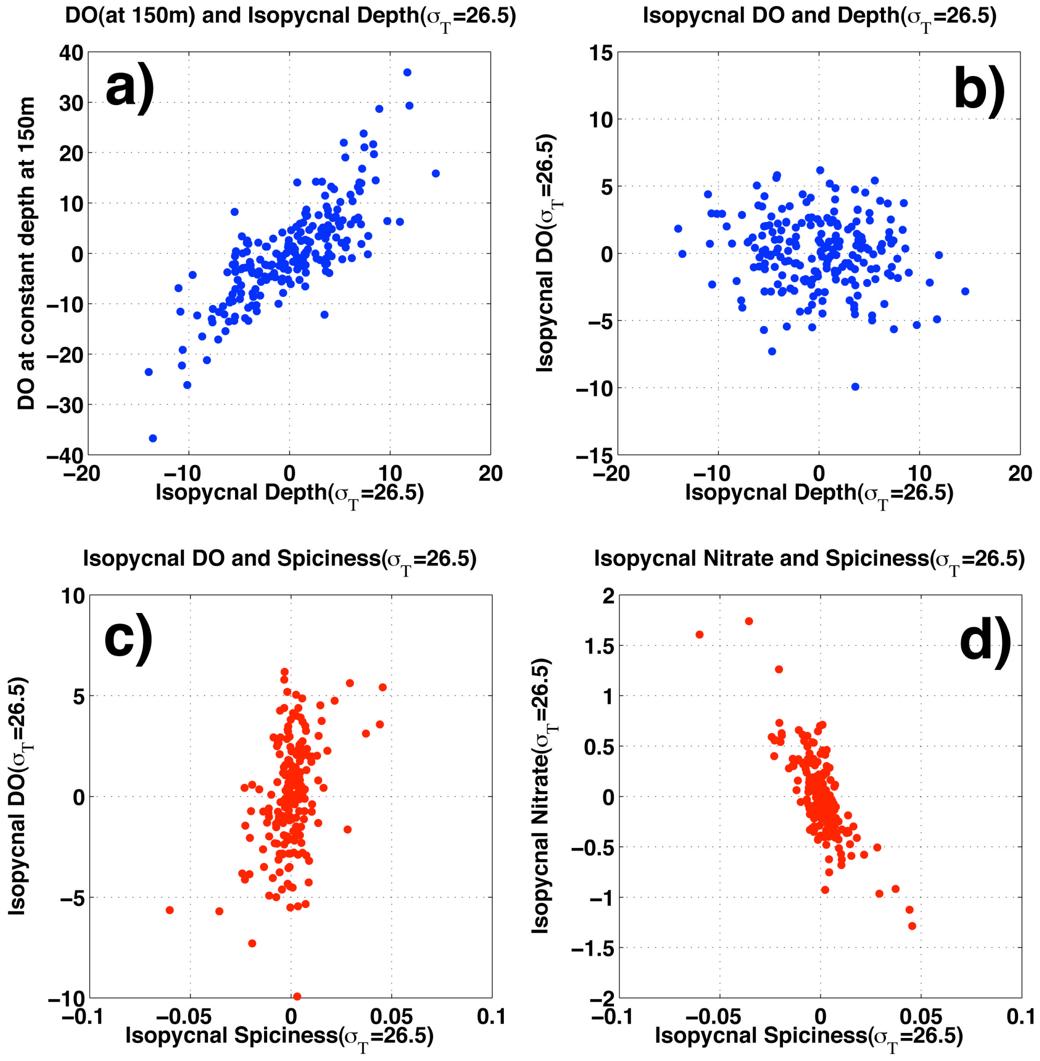

Figure 2.3. (a) Scatter plot between thermocline oxygen (dissolved oxygen at 150m depth) and isopycnal layer depth at $\sigma_\theta = 26.5$ and (b) oxygen and isopycnal layer depth at $\sigma_\theta = 26.5$. Bottom panels show scatter plot between (c) oxygen and spiciness at $\sigma_\theta = 26.5$ and (d) nitrate and spiciness at $\sigma_\theta = 26.5$. Fast Fourier Transform based high-pass filter is applied to all the data in this figure.

2.3.2 Power spectrum analysis of dissolved oxygen

Physical variability that affects the variability of tracers in the main thermocline can potentially cover a wide range of timescales. The profiling float data has time intervals of five days plus four hours, significantly more frequent than the ship-based measurements. However, the 5.17-day time interval is still not frequent enough to capture processes that occur in semi-diurnal, diurnal and inertial frequencies, such as internal waves or tides. Furthermore, these processes can be aliased by the five-day sampling interval and appear in the lower-frequency domain. The sinusoidal signal at a true frequency of f_0 can be subsampled at the interval of Δ to yield aliased frequencies of f_a as follows [*Wunsch*, 1996].

$$f_a = f_0 \pm \frac{n}{\Delta t} \qquad (2.3)$$

To demonstrate the possible importance of aliasing, we apply spectral analysis to the time series of dissolved oxygen, nitrate, salinity at a depth of 150m, and the isopycnal layer of $\sigma_\theta = 26.5$. We used *Gilman et al.,* [1963] method to generate experimental red-noise spectrum based on lag-one and lag-two autocorrelations and then calculate statistical significance on 95% confidence limits on this experimental red-noise spectrum from the F-statistics. Figure 2.4 shows the power spectrum for observed tracers and the isopycnal layer of $\sigma_\theta = 26.5$ with the experimental red-noise spectrum. For comparison, we normalized the power spectrum with total variance. Elevated power is in the low-frequency band, and it declines towards the high-frequency band for all tracers and the isopycnal layer depth. The red spectrum in the low-frequency band is predicted by the finite memory of the subsurface waters in the thermocline [*Ito and Deutsch,* 2010]. A simple thermocline ventilation model reduces to an order one autoregressive model (AR1), and in such a system, spectral power of tracer variability is predicted to scale to ω^{-2} under a white noise forcing. Note that this low-frequency spectrum contains seasonal cycles. However, the seasonal cycles of physical and chemical properties are smaller in the main thermocline than those of the properties near the surface because our analysis was performed below the base of the mixed layer and the euphotic zone.

Observed power spectrum in Figure 2.4 is not as simple as that in the AR1 model in the high-frequency band, showing a spectral peak on the timescale of about 18 days for observed tracers (Figure 2.4a-d). These spectral peaks are overlapping with the aliased inertial frequency, f_a, subsampled at the profiling cycle of approximately five days. The Coriolis parameter depends on the latitude of the float location, which ranged from 49.5°N to 50.8°N. Using equation (3), the possible range of aliased inertial frequencies (18.56 – 28.35 days) are calculated and shown in Figure 2.4, marked by blue dashed lines. A correspondence appears between the spectral peaks in Figure 2.4 and the frequency envelope predicted by the aliasing of inertial frequencies. Note that the maximum high-frequency spectral peak in observed tracers is slightly higher than the inertial frequency of 18.56 days. While the aliased inertial frequencies are closest to the observed spectral peak, aliasing of the semi-diurnal tidal frequencies can also produce somewhat similar frequencies. *Iwasaka et al.,* [2006] pointed out the possible aliasing period from the M_2 tide in Argo float observations. Therefore, aliasing of the semi-diurnal tidal frequencies can also produce somewhat similar frequencies. The aliasing of the K_2 tidal frequency leads to an apparent 28.3545 days periodicity and M_2 tidal frequency leads to an apparent 26.7540 days periodicity. The power spectrum of the isopycnal layer depth also shows similar 18-day peaks, indicating that the aliased inertial frequencies are associated with the vertical displacement of the isopycnal layer. Based on these results, we conclude that the apparent intra-seasonal variability observed in the subsurface tracers can potentially reflect a range of aliased tidal and inertial processes by subsampling these signals at the profiling frequencies of about five days that has important implications for the detection and interpretation of episodic biogeochemical events using profiling floats.

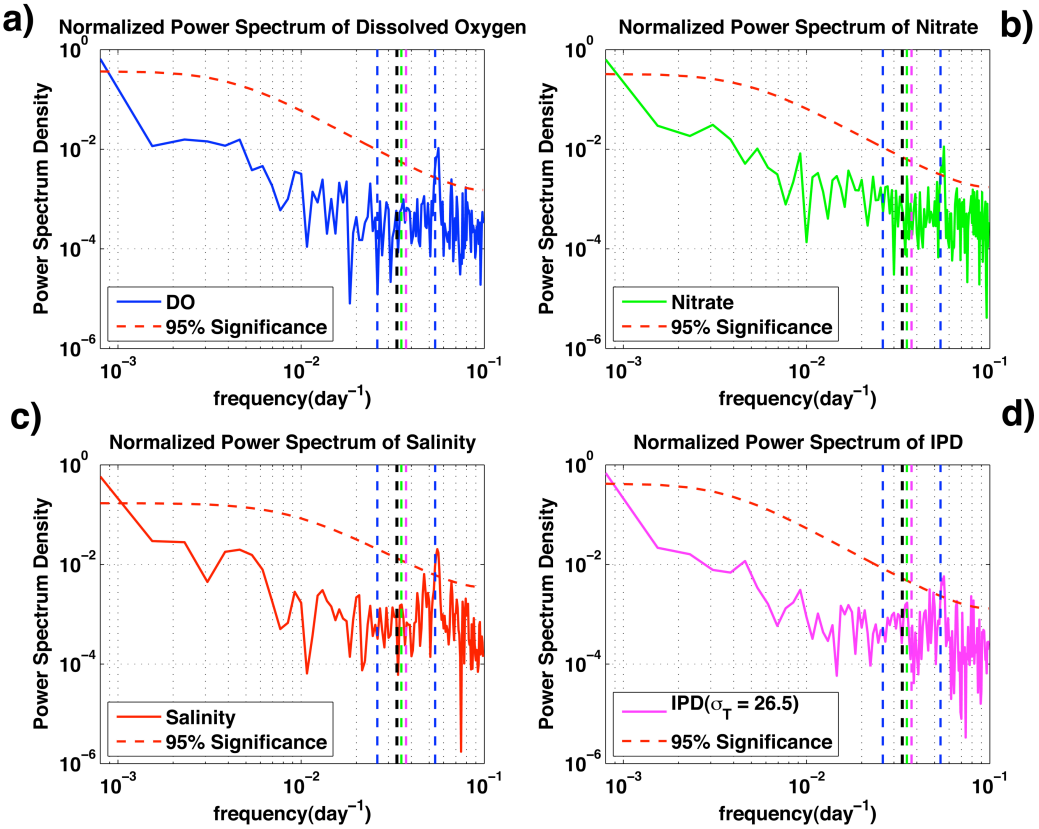

a) Normalized Power Spectrum of Dissolved Oxygen

b) Normalized Power Spectrum of Nitrate

c) Normalized Power Spectrum of Salinity

d) Normalized Power Spectrum of IPD

Black dotted line: 30 day^{-1} line
Blue dotted lines: Aliased Inertial freq: 18.56-28.35 day^{-1} lines
Purple dotted line: Aliased M_2 freq: 26.7540 day^{-1} line
Green dotted line: Aliased K_2 freq: 28.3545 day^{-1} line

Figure 2.4. Power spectrum of the observed a) dissolved oxygen in the main thermocline, b) nitrate in the main thermocline, c) salinity in the main thermocline, and d) isopycnal layer depth at $\sigma_\theta = 26.5$. Vertical colored dotted lines show possible aliased frequencies from inertial frequencies (blue dash line), M_2 (purple dash line), and K_2 (green dash line) tidal frequencies. Vertical black dash line is the cut-off frequency of 1/30 day^{-1}, which separates the high- and low-frequency band. Power spectrum is normalized by total variance. The red dashed spectral lines show the 95% significance lines estimated by red-noise spectrum based on *Gilman et al,* [1963].

2.4 Conclusion and discussion

The development of autonomous biogeochemical sensors can potentially transform the global-scale monitoring of marine chemistry. The grand challenge for the observational community is to develop an accurate description of the present state of biogeochemical tracers and to establish datasets that can be used to test predictions from numerical models. This work is motivated by the improved temporal coverage of biogeochemical tracer variability documented by recently developed biogeochemical profiling floats potentially capable of detecting episodic biogeochemical events in the upper oceans. Our analysis focused on the quality-controlled time-series observation of temperature, salinity, dissolved oxygen, and nitrate from a profiling float deployed in the eastern subpolar North Pacific, sampling at about five days frequency. While the newly observed intra-seasonal variability was not the dominant component of variance, it showed a significant variability in the main thermocline. This high-frequency variability was detected for all tracers, indicating a common physical mechanism whose frequency very closely matched the aliasing of inertial frequencies due to the subsampling at the profiling period. With approximately five-day sampling periods, an aliasing of inertial and tidal frequencies resulted in a suite of spurious intra-seasonal variability. This apparent variability can be isolated by the application of an appropriate high-pass filter. Furthermore, interpolating tracer concentrations on isopycnal surfaces can significantly reduce tracer variance, indicating that approximately 80% of variance observed at a constant depth in the main thermocline could be explained by the effect of isopycnal heaving. However, the variability of isopycnal heaving could also be a result of an aliasing of inertial and tidal frequencies.

The low-frequency component of the data longer than the 30-day timescale showed the characteristic frequency dependence with power of -2, consistent with the stochastic null hypothesis of *Ito and Deutsch* [2010]. *Cummins and Masson* [2012] demonstrated that the AR1 model indeed reproduces the effect of isopycnal heaving on subsurface oxygen variability observed at OSP. The thermocline depth at the OSP responded to atmospheric variability through the integration of the Ekman upwelling and downwelling, leading to the low-frequency variability of the thermocline depth [*Capotondi et al*., 2005, *Cummins and Lagerloef*, 2002]. Our results are in agreement with their analysis. Our results demonstrated the likelihood of what appeared to be episodic biogeochemical events could be spurious on the intra-seasonal timescales. Such spurious signals are indistinguishable from the real ones based on superficial inspection of the data. One must be careful in interpreting intra-seasonal variability of subsurface tracers based on profiling floats. A simple but efficient way to avoid aliasing is to increase the sampling frequency until all relevant processes are resolved. This may not be practical in many situations.

Here, we suggested a few methods of avoiding drawing conclusions from spurious signals. First, correlation between multiple measurements from the same platform will likely inform the existence of a common mechanism for the observed variability. Evaluating tracer measurements on isopycnal layers using CTD data is an effective way to remove the direct effect of isopycnal heaving. Secondly, analyzing multiple sensors and data types can help narrow down the possible causes of the apparent signals. For example, remote sensing products such as ocean color can inform ocean productivity, which has known imprints on biogeochemical tracers. In our case, we did not find any significant synchronous or lag correlations with a suite of physical and biological parameters, which strengthens the case that observed signals originated from aliasing. Given the sampling frequency of the instrument, it is relatively straightforward to calculate the expected range of aliased signals generated from the subsampling of inertial and tidal frequencies. Thus, the existence of spurious signals can be tested using power spectrum analysis. A growing number of autonomous biogeochemical observations and their synthesis with computational models will likely open up new opportunities for future research that clarifies the physical and biogeochemical variability of the oceans. Such model-data synthesis requires further understanding of the observations themselves. It is hoped that the approaches taken in this study may be useful for future analyses of high-frequency tracer variability.

CHAPTER 3

MECHANISMS OF CENTENNIAL-SCALE TROPICAL PACIFIC OXYGEN TRANSITION UNDER THE ANTHROPOGENIC CLIMATE CHANGE

Manuscript in preparation/under revision as

[1] Takano, Y., C. Deutsch and T. Ito (2016), Centennial-scale changes of dissolved oxygen in the Pacific basin under a warming climate, *Geophysical Research Letters*, *under revision*

[2] Takano, Y., T. Ito and C, Deutsch (2016), Mechanisms of centennial-scale tropical Pacific oxygen transition under the anthropogenic climate change, *Global Biogeochemical Cycles*, *manuscript in preparation*

Abstract

In this chapter, we explore centennial changes of the thermocline oxygen (O_2) using a hierarchy of models. Future projections from CMIP5 Earth System Models (ESMs) and a suite of perturbation experiments using a coarse resolution ocean climate and biogeochemistry model illustrate dominant patterns and mechanisms of changes in the thermocline O_2 under a warming climate. Results of the sensitivity experiments highlight the warming of the sea surface temperature as the leading cause of the deoxygenation of the global thermocline. In the extra-tropical thermocline, the warming-induced solubility decrease and the stratification-induced ventilation decrease together

deplete the thermocline O_2. The tropical thermocline exhibits much smaller changes or even a slight increase in O_2 if changes are evaluated at a constant depth. The small O_2 change in the tropics is the consequence of almost complete compensation between warming-induced solubility decrease and decreasing apparent oxygen utilization caused by the deepening of upper ocean isopycnals. By sampling progressively lighter and younger isopycnals at a constant depth, the apparent oxygen utilization appears to decrease but this could not necessarily mean that the tropical water masses are immune from anthropogenic ocean deoxygenation. The effect of weakened ocean ventilation significantly depletes tropical oxygen if changes are evaluated along an isopycnal. We have further quantified the physically (i.e. water mass age) and biologically (i.e. *OUR*) driven *AOU* changes from our sensitivity experiments. The results showed that warming induced decrease in physically and biologically driven *AOU* could equally (~48% for physics and ~52% for biology) contribute to decrease tropical thermocline *AOU*. Combined effect of warming and changes in local winds could enhance decrease in local export production, which could further decrease *AOU* in the tropical thermocline.

3.1 Introduction

Dissolved oxygen (hereafter O_2) is an essential element for marine ecosystems and biogeochemistry with far-reaching influence on the physiological and ecological processes [*Seibel*, 2010; *Vaquer-Sunyer and Duarte*, 2008] and cycling of fixed nitrogen [*Codispoti*, 1995; *Codispoti et al.*, 2001]. Previous modeling studies indicate that global warming could reduce the amount of O_2 on the global scale [*Matear and Hirst,* 2003].

Potential decline of oceanic O_2 under global warming is considered a major threat to the marine ecosystem along with ocean warming and acidification [*Gruber,* 2011]. In a warming climate, the solubility of gases in the ocean decreases as the ocean absorbs heat. Vertical mixing or overturning may also decline as the density stratification of the upper ocean increases due to the combined effects of ocean warming and increased precipitation at high latitudes [*Capotondi et al*., 2012]. These changes will reinforce the solubility-driven O_2 loss by weakening the circulation supply of O_2 to waters below the mixed layer on the global scale.

Since global warming and associated human induced climate change proceeds gradually on the centennial timescale, its impact on ocean biogeochemical tracers is hard to detect from observations because of more fast and energetic interannual and decadal variability which could bury the centennial trend signals [*Long et al*., 2016]. The spatial and temporal coverage of historic observations is sparse and irregular, which fundamentally limits our understanding on anthropogenic transient of ocean biogeochemical tracers [*Lovenduski et al*., 2015].

Numerical simulation can be a useful tool to gain insights into the anthropogenic effects on oceanic O_2. Simulations based on the state-of-the-art Earth System Models (ESMs) predict a global deoxygenation under the human-induced climate change but there are large model-to-model differences in regional projections, especially in the tropical oceans [*Bopp et al.,* 2013; *Cocco et al.,* 2013]. These ESMs are highly complex and inter-model differences are often difficult to interpret due to the numerous differences in model architecture, configurations and parameter choices even if the greenhouse forcing is applied in a consistent way.

The objective of this study is to better understand the mechanisms behind the centennial-scale responses of oceanic O_2 to anthropogenic climate change. The climatic forcing can impose transient changes in the surface buoyancy and momentum boundary conditions for the oceans, which may include numerous processes such as ocean warming, changes in hydrological cycles and atmospheric circulations. In this study, we take a hierarchical modeling approach where we use models of different complexities to achieve a deeper level of understanding. Simpler models can be manipulated to perform illustrative sensitivity experiments, which can help interpret the behavior of more complex ESMs. It is not yet clear how each aspect of atmospheric and oceanic processes impacts on the evolution of oceanic O_2, and one of our objectives is to perform a suite of sensitivity experiments using a simpler ocean circulation and biogeochemistry model to examine the effects of different aspects of the climatic forcing. The results of these sensitivity experiments are hoped to illuminate the complex behavior of the more sophisticated ESM simulations.

The structure of this chapter is following. We describe the data, model setup and experimental design in section 3.2. In section 3.3, we present the validation of the model simulated climatological O_2. We show our results from sensitivity experiments and ESMs interpreting the centennial changes in global and tropical O_2 in section 3.4. We will summarize our study and discuss implications in section 3.5.

3.2 Data and Methods

3.2.1 State-of-the-art Earth System Model (ESM) projections

We analyze the outputs from a subset of ESMs performed as a part of Coupled Model Intercomparison Project Phase 5 (CMIP5) under the historic and future climate scenario with the radiative forcing of approximately $8.5 Wm^{-2}$ at the end of the century (RCP8.5) [*Meinshausen et al.,* 2011; *Taylor et al.,* 2012]. Table 3.1 lists the models used in this study. Briefly, we analyze the ESMs including GFDL-ESM2M, GFDL-ESM2G [*Dunne et al.,* 2012], HADGEM2-ES [*Collins et al.,* 2011], IPSL-CM5A-MR [*Dufresne et al.,* 2013], MPI-ESM-MR [*Giorgetta et al.,* 2013], and CESM1-BGC [*Moore et al.,* 2013]. These models represent a wide range of climate-sensitive marine ecosystem and biogeochemical processes in diverse ways. We focus on analyzing centennial changes in O_2 content in the main thermocline (between 150m – 600m), which includes the core of the OMZs in the tropical oceans [*Karstensen et al.,* 2008; *Cabré et al.,* 2015]. The ESMs represent marine ecosystems and biogeochemical cycles including O_2, CO_2, and nutrients with diverse parameterization of biological production, export and remineralization of organic matter in the water column. The future projections from ESMs could provide broad implications on how marine ecosystems and biogeochemical cycles changes.

Table 3.1. CMIP5 modeling groups, institute ID, and model names.

Modeling Group/Center	Institute ID	Model Name
NOAA Geophysical Fluid Dynamics Laboratory	NOAA GFDL	GFDL ESM2M GFDL ESM2G
Institut Pierre-Simon Laplace	IPSL	IPSL CM5A MR
Met Office Hadley Centre (additional HadGEM2-ES realizations contributed by Instituto Nacional de Pesquisas Espaciais)	MOHC (additional realization by INPE)	HadGEM2-ES
Max-Planck-Institut für Meteorologie (Max Planck Institute for Meteorology)	MPI-M	MPI-ESM-MR
Community Earth System Model Contributors	NSF-DOE-NCAR	CESM1 (BGC)

3.2.2 Climate forcing for the ocean circulation and biogeochemistry

Centennial transitions in the surface climate could significantly influence ocean circulations and associated biogeochemical cycles. In the CMIP5 simulations surface and tropospheric temperature increase as a consequence of increased greenhouse gases [*Vallis et al.,* 2015]. Long-term changes in the energy budget of the Earth could result in a variety of surface climate changes including large-scale atmospheric circulations and surface freshwater fluxes over the global oceans. Common features in centennial scale surface climate change projected in ESM simulations and observations are (1) increase in sea surface temperature, (2) acceleration of hydrological cycles [*Held and Soden,* 2006; *Schneider et al.,* 2010], (3) a trend toward stronger and poleward shifted southern hemisphere jet [*Thompson et al.,* 2000; *Mashall*, 2003*; Gillett and Fyfe,* 2013], and (4) a possible weakening of the Walker circulation and associated tropical Pacific trade wind [*Vecchi et al.,* 2006; *Tokinaga et al*., 2012]. As a reference for increase in sea surface temperature, we calculated centennial changes in global mean sea surface temperature from output of CMIP5 RCP8.5 future projections. Figure 3.1 shows the time series of global mean sea surface temperature from the ESM historic simulations (before 2005) and RCP 8.5 future projections. Increase in sea surface temperature starts to accelerate around 2000 and rise between the range of 2.5 – 4.5 °C by 2100 relative to 1900 (Figure 3.1). Figure 3.2 shows the zonal mean changes in freshwater flux (evaporation minus precipitation (E-P)) and the Southern Hemisphere zonal wind stress from CMIP5 models over the next century. Zonal mean plots exhibit enhanced hydrological cycles and increase in the Southern Ocean zonal wind stress associated with the trend in the Southern Annular Mode (SAM). Tropical Pacific wind stress shows gradual increase (~ 6×10^{-3} N/m^2) over the next century, which could be associated with the weakening of the Walker circulation (Figure 3.2c and d). However, changes in tropical Pacific wind could also be associated with more energetic decadal variability. Based on the analysis of surface atmospheric fields from CMIP5 future projections (Figure 3.1 and 3.2), we designed sensitivity experiments mimicking the centennial scale climate changes. Despite the uncertainties and complicated spatial patterns of surface climate change (especially for tropical Pacific wind changes), we kept our climate forcing as simple as possible including the essence of the processes (1-4) to simplify our interpretation on the results from sensitivity experiments.

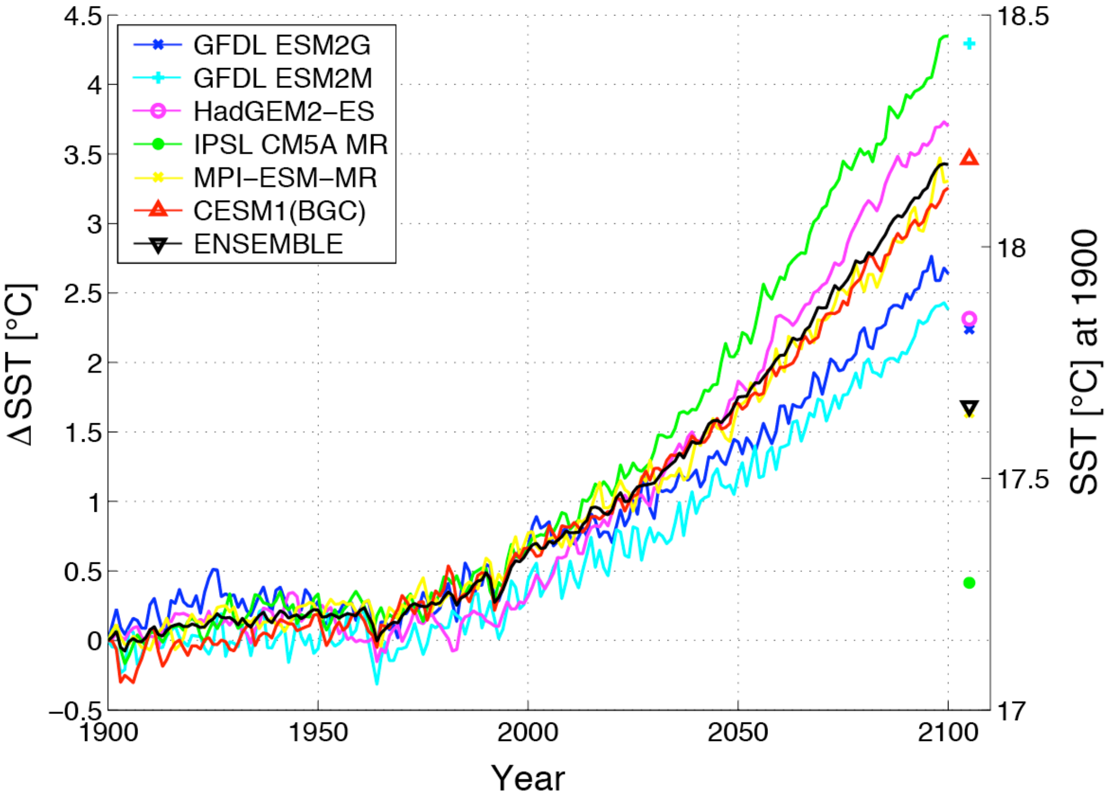

Figure 3.1. Time series of global mean sea surface temperature (SST) anomaly from selected CMIP5 models. SST anomalies are based on SST relative to the values at 1900 (shown as colored shapes). We used model ensemble mean SST anomaly (ENSEMBLE, black line) to conduct perturbation experiments (see section 3.2 for details).

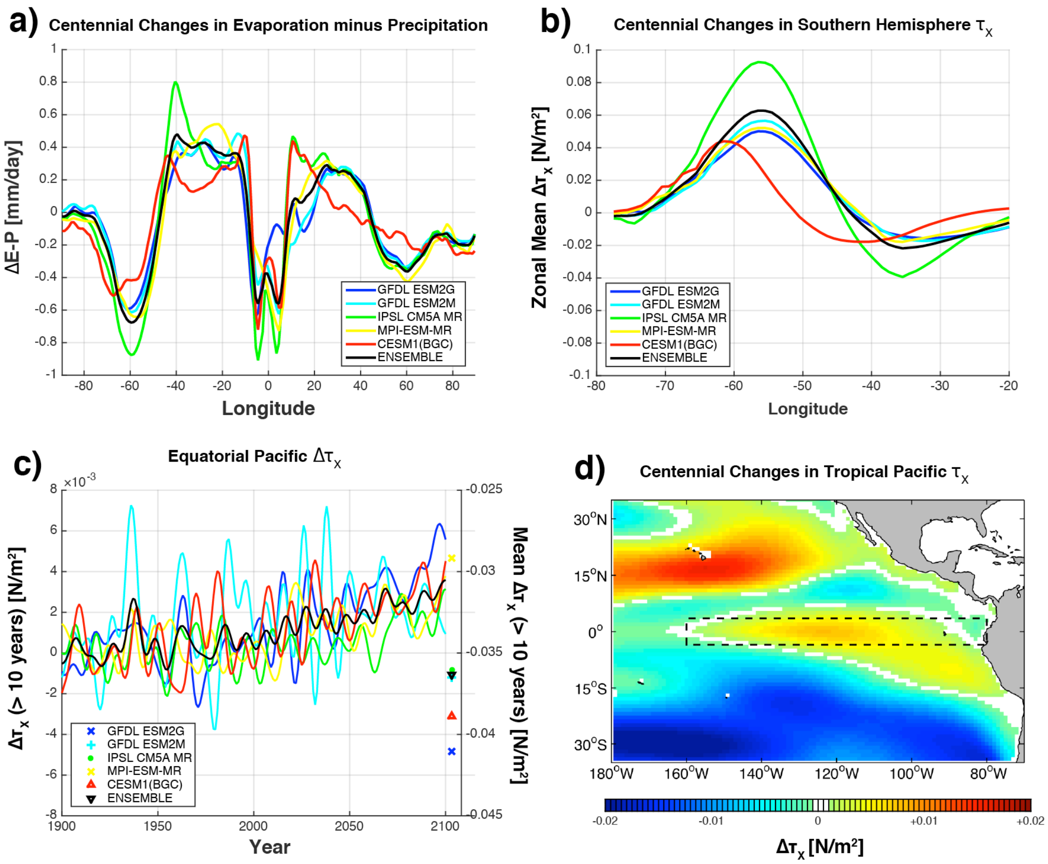

Figure 3.2. Centennial changes (i.e. difference between pre-industrial mean (1900-1930) and RCP8.5 mean (2070-2100)) of zonal mean a) evaporation minus precipitation (E-P) [in mm/day] and b) zonal wind stress [in N/m^2] in the Southern hemisphere. c) Temporal evolution of equatorial Pacific zonal wind stress anomalies (relative to pre-industrial mean) [in N/m^2] defined as the weighted area-mean zonal wind stress anomalies in box region shown in d). 10-year low-pass filter is applied to time series in c). d) Centennial changes in tropical Pacific zonal wind stress [in N/m^2] from the ensemble mean of selected CMIP5 models (see main text and Table 3.1).

3.2.3 Ocean circulation and biogeochemistry model

It is difficult to mechanistically illustrate changes in O_2 cycles from simply analyzing the limited outputs from ESMs, which often lacks some diagnostic information (e.g., ideal age) necessary for full diagnosis of the model output. We conduct a suite of sensitivity experiments to evaluate the impacts of surface climate forcing on oceanic O_2

cycles using a coarse-resolution ocean circulation and biogeochemistry model. The model is essentially identical to the model used by *Ito et al.*, [2015] which is shown to reproduce the CMIP5 projection of performed and regenerated carbon pool in the Southern Ocean. Briefly the model is based on the Massachusetts Institute of Technology general circulation model (MITgcm) [*Marshall et al.*, 1997a, b] with a simple biogeochemistry component [*Dutkiewicz et al.*, 2005; *Parekh et al.*, 2005]. The model has a global bathymetry in a 2.8°×2.8° longitude-latitude grid, and 23 non-uniform vertical levels with increased resolution near the surface. Mesoscale eddies are parameterized using the isopycnal thickness and tracer diffusion scheme [*Gent and McWilliams*, 1990] with a uniform constant isopycnal thickness diffusivity of 10^3 m^2s^{-1}, and tracers are also subject to along-isopycnal diffusion at the same rate [*Redi*, *1982*]. Vertical mixing is parameterized using *Bryan and Lewis* [1979] scheme, in which vertical diffusivity is set to 0.3×10^{-4} m^2s^{-1} in the upper 2000m and increase to 1×10^{-4} m^2s^{-1} in the interior ocean following an arctangent profile. The mixed-layer processes are parameterized using the KPP scheme [*Large et al.*, 1994]. The model carries dissolved phosphorus (PO_4), dissolved organic phosphorus (*DOP*), dissolved oxygen (O_2), and dissolved iron (*Fe*). In addition, the model carries an ideal age tracer to quantify the how long the effects of respiratory oxygen loss is integrated in the interior ocean. We spin up the model with climatological wind stress, freshwater flux, and heat flux fields [*Trenberth et al.*, 1989; *Jiang et al.*, 1999]. To maintain surface temperature-salinity properties close to the observations, we also applied Newtonian relaxation to the sea surface temperature and salinity towards monthly climatology [*Levitus and Boyer*, 1994a,b] with timescales of 60 and 90 days, respectively. Because of the lack of seaice/ice-shelf processes and highly smoothed topography, the model cannot adequately form the Antarctic Bottom Water. To address this issue, we locally raised climatological salinity in the polar Southern Ocean in the restoring boundary condition to maintain the deep ventilation in the southern high latitudes. This modification of salinity restoring accelerated the lower overturning circulation and increased the oxygen concentration of the abyssal Southern Ocean in much better agreement with observations. After spinning up the model for several millennia to achieve a steady state, we performed sensitivity experiments.

3.2.4 Idealized sensitivity experiments

Based on previous studies (see section 3.2.2) and climate forcing projected in the ESM simulations, we perform idealized sensitivity experiments including the following forcing.

A) ***MITgcm-Warm*** A global uniform increase in the sea surface temperature. The rate of temperature increase is set to the CMIP5 multi-model ensemble mean (Figure 3.1).

B) ***MITgcm-EmP*** Intensification of freshwater flux by 10% per century (Figure 3.3a).

C) ***MITgcm-SAM*** Intensification and poleward shift of the zonal wind stress over the Southern Ocean (Figure 3.3b).

D) ***MITgcm-Trade*** Changes in the zonal wind over the Equatorial Pacific (Figure 3.3c).

E) ***MITgcm-ALL*** Inclusion of all forcing patterns (A-D) (ALL).

The warming sensitivity (A) is implemented through the restoring boundary condition of the sea surface temperature where a globally uniform increase of sea surface temperature is superimposed over the mean seasonal cycle. The rate of temperature increase is based on the ensemble mean of sea surface temperature from the selected CMIP5 models (Figure 3.1, black line). The freshwater sensitivity (B) is implemented by globally modulating the amplitude of monthly evaporation minus the precipitation field while maintaining the same spatial pattern as the climatology (Figure 3.3a). We increase the amplitude of the climatological freshwater flux by 10% per century to express intensification of hydrological cycles in a warming climate (similar to what we observe from CMIP5 analysis). We implement the SAM-based zonal wind stress perturbation (C) by adding regression coefficients between 21°S and 88.6°S, based on the normalized monthly SAM index [*Marshall*, 2003] and NCEP-NCAR reanalysis monthly mean zonal wind stress [*Kalnay et al*., 1996] from 1957 to 2013 for each month. We impose a decrease in the trade wind (i.e., positive anomalies of zonal wind stress) as a Gaussian anomaly in the eastern equatorial Pacific Ocean (Figure 3.3c), representing equatorial Pacific wind changes shown in Figure 3.2c and 3.2d to some extent. The trade wind forcing could include signals from both decadal variability and weakening of the Walker circulation under global warming [*Vecchi et al.,* 2006; *Tokinaga et al*., 2012]. The Gaussian patch is centered over the equator in the eastern tropical Pacific Ocean, and the magnitude of the zonal wind perturbation is 3×10^{-5} $Nm^{-2}yr^{-1}$ and its spatial pattern is shown in Figure 3.3c. We also perform a control run (MITgcm-CTL) without perturbation. Comparing results from each sensitivity experiment with the CTL run measures the response to each idealized climate forcing.

We first compare our sensitivity experiments with the CMIP5 model projections to evaluate the representation of long-term changes in O_2 in the main thermocline. Then we further analyze the physical and biogeochemical controls on the long-term changes in the thermocline O_2 content by analyzing the results from the idealized sensitivity experiments.

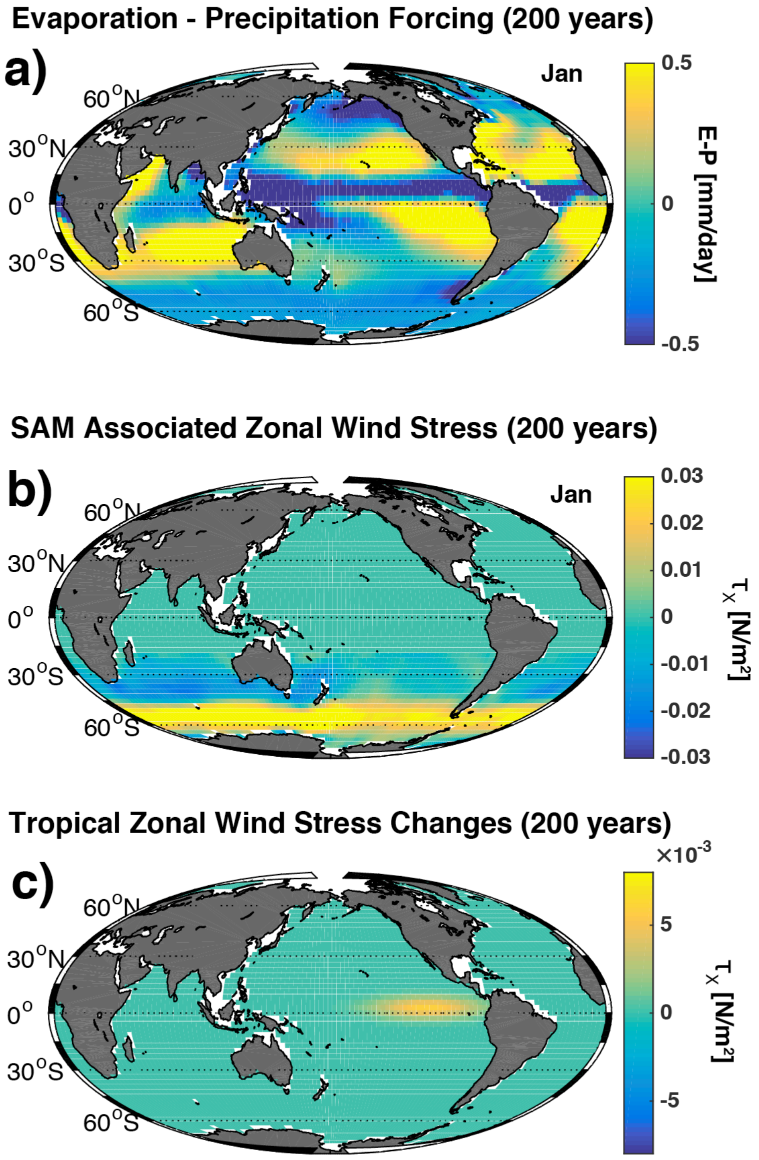

Figure 3.3. Spatial patterns of a) centennial changes (after 200 years) in evaporation minus precipitation (E-P) and b) and c) zonal wind stress (τ_x) used for perturbation experiments. Zonal wind stresses are from SAM regression based zonal wind stress and idealized perturbation for zonal wind stress changes in the tropical Pacific Ocean.

3.3 CMIP5 Multi-Model Projections of global thermocline deoxygenation

3.3.1 Model validation

First, we compare the climatological mean O_2 distribution between CMIP5 ESMs, MITgcm-CTL and World Ocean Atlas 2009 (WOA2009) [*Garcia et al.,* 2010]. Here we focus on analyzing the vertically averaged O_2 from 150m to 600m (160m to 610m for MITgcm) as a metric of thermocline O_2. This depth range covers the core of the O_2 minimum layer, which is typically located within $26.5<\sigma_\theta<27.0$ and $200m<z<700m$ in the tropical Pacific generally overlapping with the upper ocean thermocline [*Karstensen et al.,* 2008; *Stramma et al.,* 2008]. The model climatology is based on the 30-year mean in the late 20th century (1970-2000). CMIP5 ESMs and MITgcm-CTL generally captures the large-scale climatological distributions of thermocline O_2 in WOA2009 (4). Observed climatology shows relatively low O_2 over the tropics, including the eastern tropical Pacific, the tropical Atlantic, and the Indian Ocean. Magnitudes vary but the O_2 minimum in the North Pacific is also reproduced in the models. Among the models analyzed in this study, there is a range in the mean bias (global: -22.8 to 22.7 mmol/m^3, Pacific domain, north of 20°S: -23.4 to 34.2 mmol/m^3) and in the spatial correlation coefficient (R = 0.88 to 0.96) both globally and over the Pacific domain, north of 20°S (Table 3.2). The MITgcm-CTL exhibits reasonable mean oxygen concentration as well as spatial pattern (global: mean bias = 1.11 mmol/m^3, R = 0.92, Pacific domain, north of 20°S: mean bias = 13.5 mmol/m^3, R = 0.91) (Table 3.2). A comprehensive analysis of simulated OMZs in the CMIP5 models is presented in *Cabŕe et al.,* [2015] with detailed examination of the horizontal and vertical structures of OMZs and hypoxic volumes. The horizontal extent of oxygen minimum zones in the tropical Pacific Ocean varies across model simulations.

Table 3.2. Spatial correlation coefficients (R) of thermocline oxygen between selected models and World Ocean Atlas 2009 (the first two rows). The bottom two rows show weighted-area mean thermocline oxygen anomalies based on the difference between selected models and World Ocean Atlas 2009. MITgcm is from control experiment. Spatial correlation coefficients and weighted area-mean values in the Pacific Ocean are based on Pacific domain covering the north of 25°S.

	GFDL ESM2G	GFDL ESM2M	HadGEM2-ES	IPSL CM5A MR	MPI-ESM-MR	CESM1 (BGC)	ENS-EMBLE MEAN	MIT gcm CTL
R global	0.90	0.90	0.91	0.93	0.94	0.88	0.96	0.92
R Pacific	0.90	0.84	0.88	0.91	0.94	0.94	0.96	0.91
ΔO_2 global mean [mmol/m^3]	-9.70	0.23	17.5	22.7	-4.7	-22.8	-0.58	1.11
ΔO_2 Pacific mean [mmol/m^3]	-7.16	12.3	30.0	34.2	-12.6	-23.4	4.16	13.5

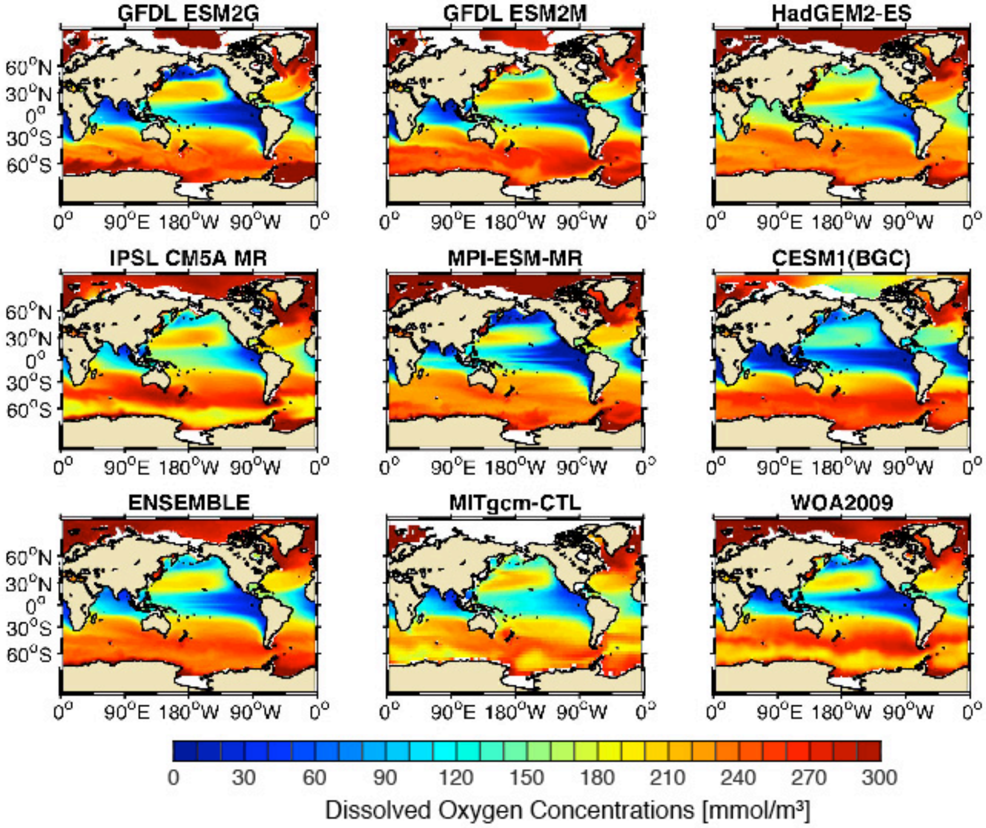

Figure 3.4. Comparison of climatological annual mean dissolved oxygen concentration [mmol/m^3] averaged in the depth range of the main thermocline (150m – 600m for CMIP5 models, 160m – 610m for MITgcm) from six selected CMIP5 Earth System Models, a MITgcm control experiment, and the World Ocean Atlas 2009. The model mean shows the multi-model mean dissolved oxygen concentration from the CMIP5 models. Climatology is based on the 30-year mean in the late 20th century (1970-2000).

3.3.2 Centennial Changes from CMIP5 Multi-Model Projections

Figure 3.5 shows long-term changes in the thermocline O_2 (as we defined in Figure 3.4) from the CMIP5 ESMs and MITgcm-ALL. Estimates of long-term change are calculated as the difference between the 30-year temporal means at the beginning (1900-1930) and the end (2070-2100) of the period of analysis. Most of the high-latitude regions, including the North Pacific and the Southern Ocean, show decreases in the thermocline O_2 except for the sub-polar North Pacific from GFDL ESM2G, which shows an increase. The magnitude of changes in O_2 differs among the models over the range of approximately 10-40 mmol/m^3 but the centennial decrease in extra-tropical thermocline O_2 is a robust feature of these models as previously discussed [*Bopp et al.*, 2013; *Cocco et al.*, 2013]. However, the behavior of tropical oceans differs from that of high-latitude regions. The majority of CMIP5 model projections shows no change or even increases in the thermocline O_2 over the tropical oceans. Previous modeling studies also showed the existence of similar increases in the tropical thermocline O_2 under global warming [*Mater and Hirst,* 2003]. MITgcm-ALL also shows similar behavior of the tropical thermocline O_2 even though simulations are conducted with relatively simple climate trend forcing. In the eastern tropical Pacific Ocean and Indian Ocean, MITgcm-ALL shows moderate increases of about 10 mmol/m^3. Despite differences among the detailed spatial patterns among the CMIP5 ESMs and MITgcm-ALL, tropical ocean inventories are relatively stable in the warming world. This is encouraging as the idealized experiments with MITgcm may provide useful insights into some of the mechanisms at work in the CMIP5 ESMs.

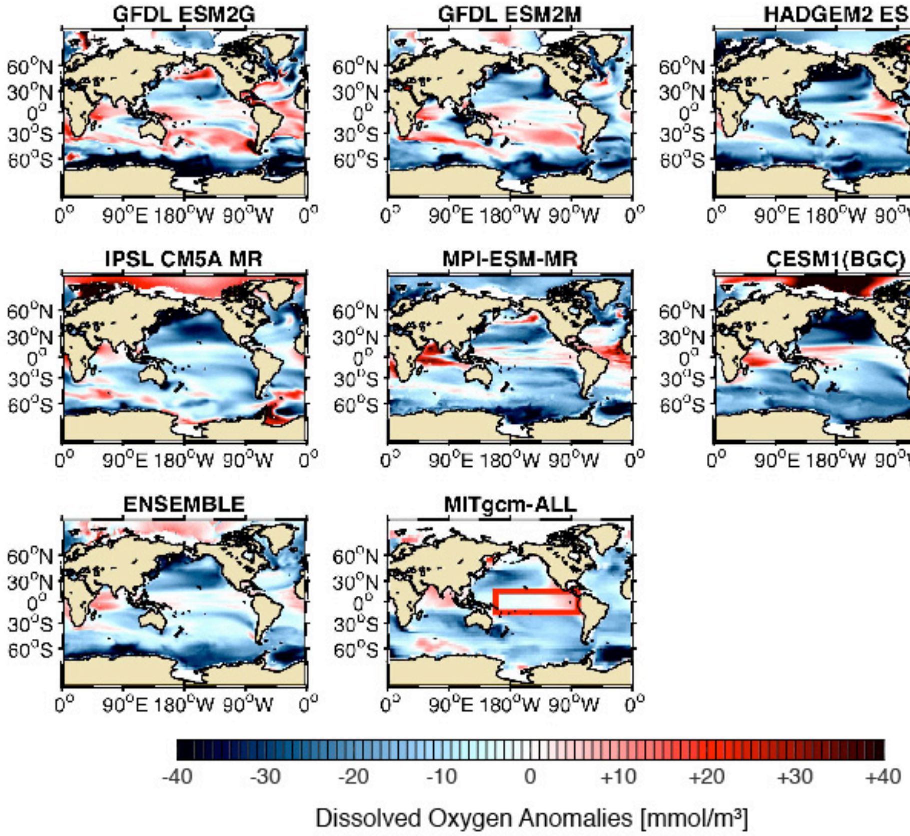

Figure 3.5. Dissolved oxygen concentration changes under the RCP8.5 scenario from 1900-1930 to 2070-2100. Vertically averaged (150m – 600m, 160m – 610m for MITgcm-ALL) oxygen concentrations across the CMIP5 models are plotted. The MITgcm-ALL is based on the sensitivity experiment with all climatic trends forcing that mimics forced changes in the CMIP5 models. The red rectangle is the tropical Pacific domain used for defining our area-mean based metrics.

3.3.3 Decomposition of O_2 into solubility and AOU

Changes in O_2 could be partitioned into two effects driven by thermodynamics and biology. The thermodynamically driven component, oxygen saturation, primarily depends on temperature, and the biologically driven component, apparent oxygen utilization (*AOU*), represents the cumulative loss of O_2 due to respiration.

$$O_2 = O_{2,sat}(S,\theta) - AOU \qquad (3.1)$$

Oxygen saturation ($O_{2,sat}$) depends on potential temperature (θ) and salinity (S), and AOU is the difference between $O_{2,sat}$ and O_2. While this decomposition is useful, it is important to note that AOU can only approximate the effect of cumulative biological utilization as it may also include the effects of air-sea disequilibrium and diapycnal mixing [*Ito et al.,* 2004].

Figure 3.6 presents long-term changes in thermocline $O_{2,sat}$ similar to Figure 3.5. An increase in the temperature results in a decrease in $O_{2,sat}$. While both the CMIP5 ESM projections and the MITgcm-ALL simulation depict decreased $O_{2,sat}$ in most of the regions, the GFDL models show increased $O_{2,sat}$ in parts of the Southern Ocean. $O_{2,sat}$ in water mass formation and subduction regions, such as Southern Ocean and North Pacific Ocean, exhibit intense centennial decrease compared to sub tropical oceans and tropics. The centennial changes in O_2 are small or close to zero in the tropical oceans (Figure 3.5) but $O_{2,sat}$ decrease significantly in these regions.

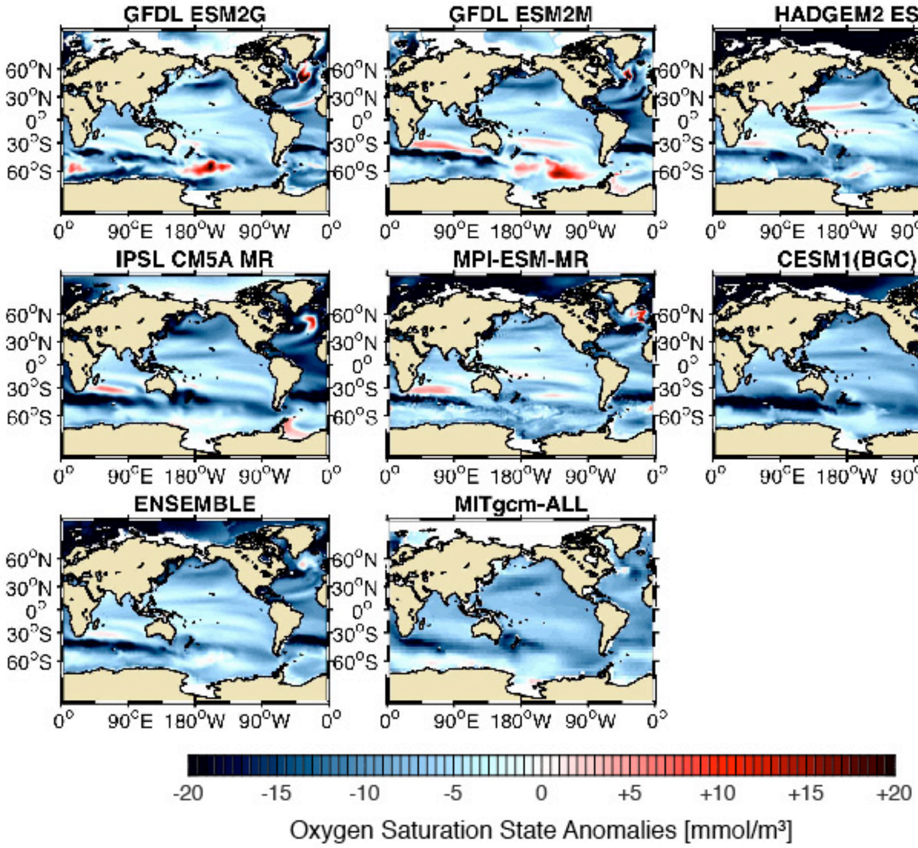

Figure 3.6. Oxygen saturation state changes under the RCP8.5 scenario from 1900-1930 to 2070-2100. Vertically averaged (150m – 600m, 160m – 610m for MITgcm-ALL) oxygen saturation across the CMIP5 models are plotted. MITgcm-ALL is based on sensitivity experiments with all climatic trends forcing mimicking forced changes in the CMIP5 models.

Figure 3.7 shows centennial-scale changes in the thermocline *AOU* similar to Figure 3.5. Both versions of the GFDL models show different pattern in the South Pacific gyre, but most of the models exhibit similar patterns of *AOU*. CMIP5 ESM projections generally show an increase in *AOU* in mid- to high-latitude oceans likely due to the reduced ventilation from the surface to the interior ocean consistent with previous studies [*Cabŕe et al*., 2015, *Dore at al*., 2009, *Keeling et al*., 2010]. All of the models also show relatively stable or decreasing *AOU* in the tropics (Figure 3.7). This confirms that the changes in $O_{2,sat}$ and AOU compensate one another so that the centennial changes in O_2 are small or close to zero in the tropical oceans (Figure 3.5). In the following section, we examine changes in the ventilation and biological processes that affect the response of AOU in the tropical oceans, with emphasis in the Pacific Ocean.

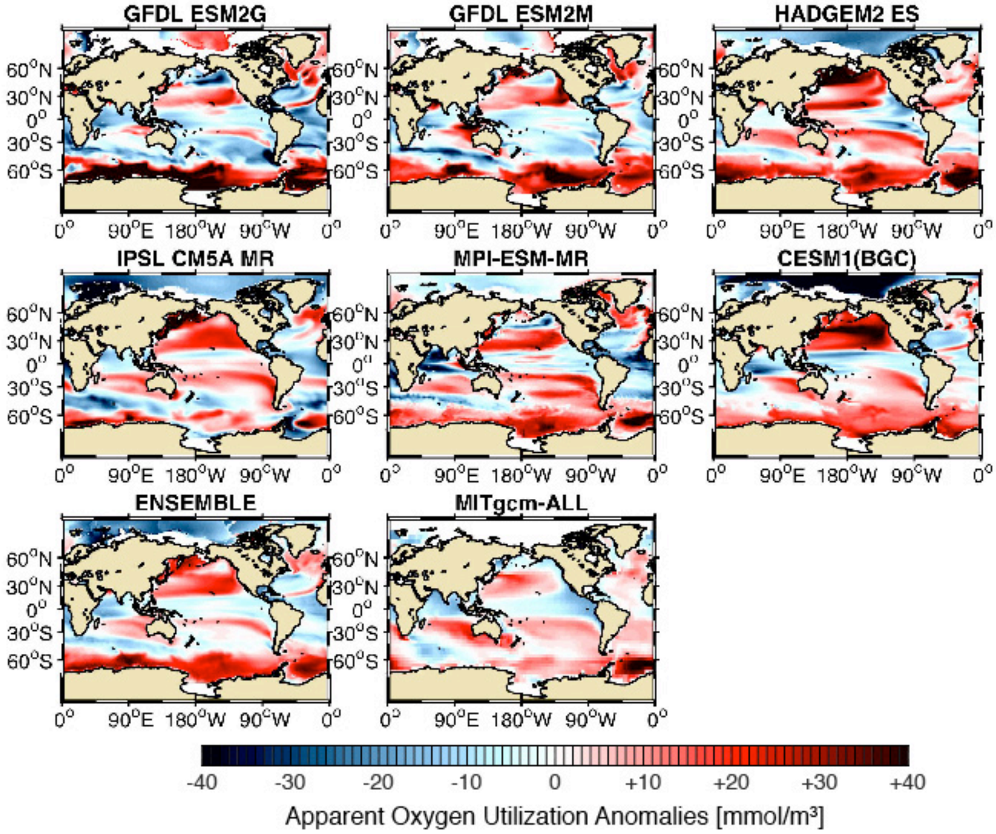

Figure 3.7. Apparent oxygen utilization changes under the RCP8.5 scenario from 1900-1930 to 2070-2100. Vertically averaged (150m – 600m, 160m – 610m for MITgcm-ALL) *AOU* across the CMIP5 models are plotted. MITgcm-ALL is based on sensitivity experiments with all climatic trends forcing mimicking forced changes in the CMIP5 models.

3.4 Mechanisms of anthropogenic thermocline deoxygenation

3.4.1 Global thermocline O_2 change

Results from the idealized sensitivity experiments illustrate the effect of various climatic forcings on the thermocline O_2. Figure 3.8 shows the time series of the global thermocline O_2, $O_{2,sat}$ and AOU simulated by each of the sensitivity experiments superimposed over the range of CMIP5 ESMs. The CMIP5 ESM projections show diverse rates of centennial-scale deoxygenation from 6 to more than 10 mmol/m^3 averaging over the depth range of 150 – 600m. MITgcm-ALL shows a decrease (~10 mmol/m^3) in the global thermocline O_2 within the range of the CMIP5 models. Results from idealized sensitivity experiments indicate relative importance of each climate forcing mechanism. Ocean warming contributes the largest amount of decrease to the thermocline O_2 inventory, partially compensated by the effect of enhanced ventilation from the southern hemisphere.

The time series of $O_{2,sat}$ and AOU (Figure 3.8b and c) shows the separation between thermally and biologically driven O_2 declines reinforcing each other under the global warming. The increase in ocean heat content decreases the solubility of gases. The warming of the upper ocean also increases thermal stratification, reducing the ventilation of thermocline water. Weakened ventilation increases the cumulative effect of biologically O_2 consumption as measured by the increase in AOU.

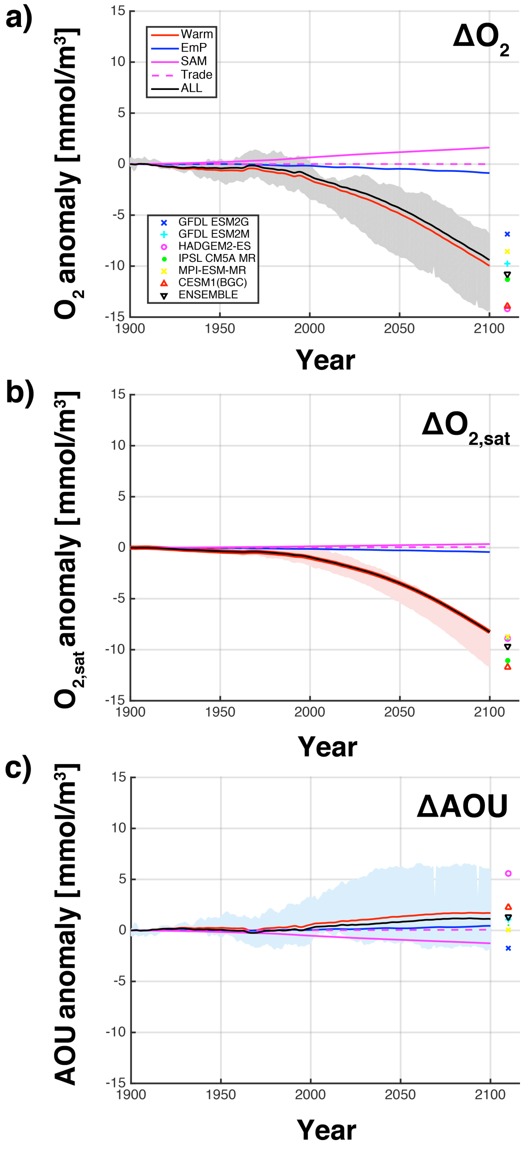

Figure 3.8. Temporal evolutions of global mean thermocline properties covering all longitude and latitudes, in 160 – 610m based on a suite of perturbation experiments (Red = warming, Blue = freshwater, Magenta = Southern Ocean wind, Dotted Magenta = Tropical trade wind, and Black solid = all forcing). (a) Dissolved oxygen, (b) oxygen saturation, and (c) apparent oxygen utilization (AOU) time series are all relative to the control experiment. All the properties are in the unit of mmol/m^3. Shadings show multi-model range, anomalies relative to average values from 1900-1930. Anomalies at 2100 are based on values relative to the preindustrial (1900-1930) mean from selected CMIP5 models shown as colored shapes.

When globally averaged, the majority of the thermocline deoxygenation is driven by the solubility decrease in the CMIP5 ensemble as well as in MITgcm-ALL. The increase in *AOU* (i.e. decrease in O_2 due to cumulative biological O_2 consumption) is relatively small compared to solubility decrease. This is due to the averaging of regionally positive and negative changes in *AOU*, while solubility change is generally negative globally. Enhanced hydrological cycles have relatively little effect on the deoxygenation of the thermocline waters, but the freshwater forcing is more important for the ventilation of the deep waters. The intensification of the Southern Ocean wind decreases *AOU* (i.e. increases O_2), partially compensating the global thermocline deoxygenation. In summary, the global thermocline deoxygenation is mostly driven by the warming-induced solubility decline, which is reinforced by the effect of weakened ventilation on cumulative biological oxygen utilization.

3.4.2 Low-latitude thermocline O_2 change

Spatial patterns of *AOU* change in Figure 3.7 show regionally significant changes. The CMIP5 ESMs and MITgcm-ALL simulations both show increasing *AOU* in the extra-tropics and decreasing *AOU* in tropics. In mid- and high-latitudes, the increasing *AOU* reinforces thermally induced decline of $O_{2,sat}$ but in tropics the two components are cancelling out one another. Previous studies have shown that the CMIP5 model projections show significant model to model differences in the tropical O_2 changes on the centennial timescale where even the sign of the changes is not in agreement [*Bopp et al.*, 2013; *Cocco et al.*, 2013; *Cabré et al.*, 2015]. Sensitivity experiments provide some insights into the mechanism behind the changes in tropical *AOU*. Figure 3.9 shows the time series of O_2, O_{2sat} and *AOU* averaged over the low latitude (between 15°S to 15°N) thermocline. For both CMIP-5 ESMs and MITgcm-ALL, *AOU* in the tropical thermocline decreases towards the late 21st century, and the sensitivity experiments show that ocean warming plays the dominant role for the decline of *AOU* at low latitudes. Due to the compensating changes between $O_{2,sat}$ and *AOU* (both ranging from ~5 to 10 mmol/m^3 decrease), the net O_2 change is a relatively small residual between the two components. Intensification of freshwater fluxes slightly decreases *AOU* but the magnitude is small (<1 mmol/m^3) compared to warming induced changes.

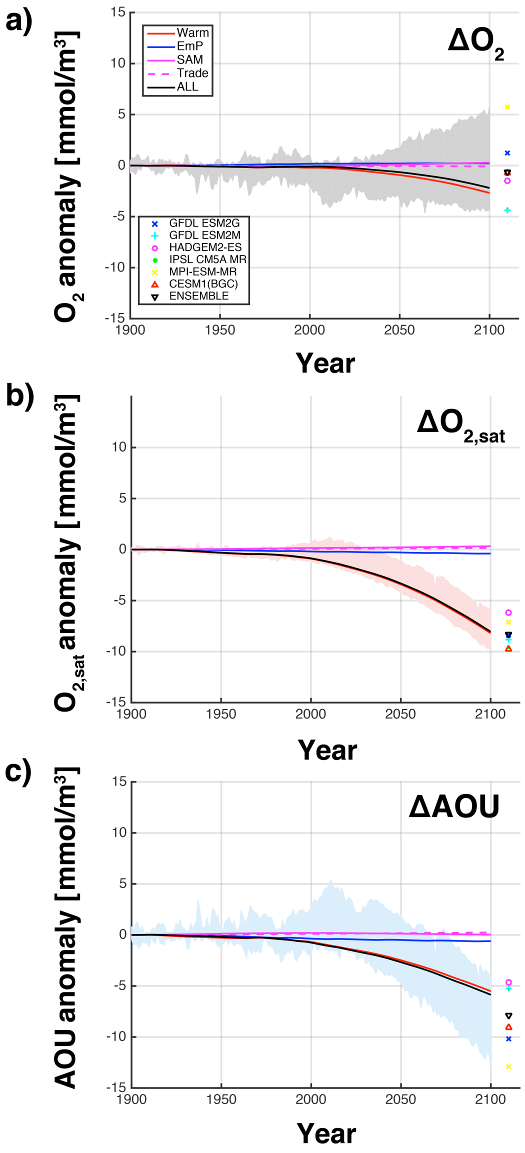

Figure 3.9. The same as in Figure 3.8 except for tropical thermocline (covering the latitudinal range of 15°S to 15°N).

Figure 3.10 shows the time series of O_2, $O_{2,sat}$ and *AOU* averaged over the tropical Pacific thermocline. Similar to the tropical thermocline (Figure 3.9), changes in thermocline O_2 show compensating changes in the $O_{2,sat}$ and *AOU*. Ocean warming is the main driver of decline in $O_{2,sat}$ and *AOU* but changes in the other climatic factors also plays a secondary role in decreasing *AOU* (~ 2 mmol/m^3) in the tropical Pacific Ocean.

The secondary effect of other climatic factors, such as changes in winds, could also enhance decrease in *AOU* from combined effect (Figure 3.10c). In the next section, we focus on the mechanistic link between the ocean warming and the decline of *AOU*.

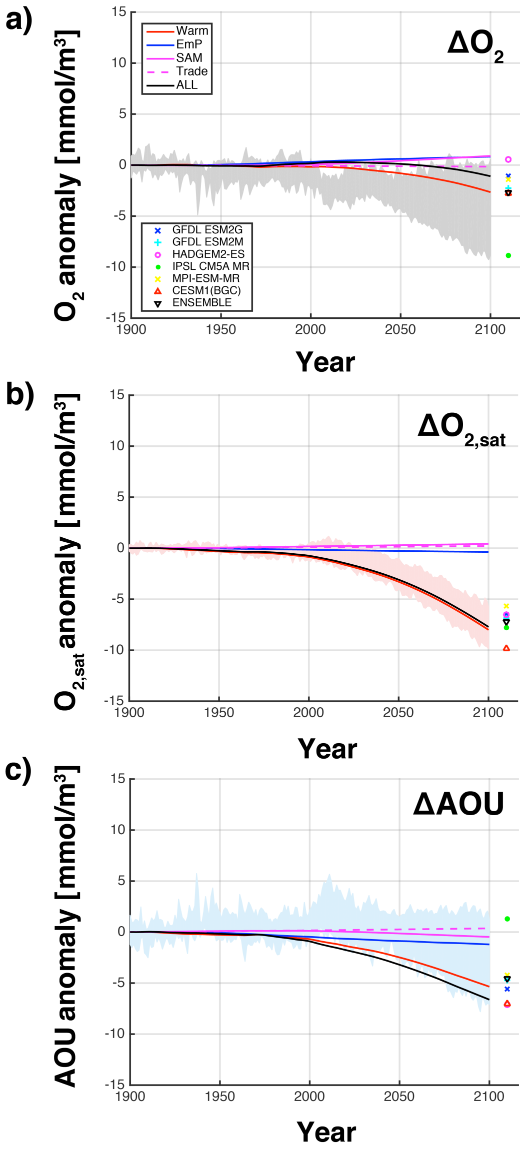

Figure 3.10. The same as in Figure 3.8 except for tropical Pacific thermocline (within the domain 159.5°E-80.5°W, 15.5°S-15.5°N shown as the rectangular box in Figure 3.5).

3.4.3 Causes of the centennial decline in the low-latitude AOU: Export Production

A reduction in *AOU* can potentially occur through two mechanisms; (1) reduced rates of organic matter decomposition and (2) shorter transit times of waters circulating into the tropical thermocline from the surface. The former mechanism (1) decreases the rate of biological oxygen consumption, Oxygen Utilization Rate (*OUR*), and the latter mechanism (2) decreases the age of the water in the tropical thermocline. The water age measures the length of time the parcel has spent in the interior ocean since the last contact with the surface mixed layer.

As a metric of *OUR*, we examine the export of particulate organic matter at around 100m depth. Since most sinking organic matter is oxidized at depths shallower than 1000m, the reduction of particle flux translates into slower respiration rates. Both in the CMIP5 ESMs and MITgcm-ALL simulations, the export production exhibits a remarkably consistent reduction across models, from 10 - 30% reduction by 2100 (Figure 3.11). The cause of reduced *AOU*, at least partially, lies in the declining biological productivity and subsurface respiration. The upwelled nutrient is fully utilized within approximately 4°S-4°N, so changes in the equatorial upwelling can regulate the productivity and export of organic matter averaged over these latitudes. In the Pacific Ocean, the long-term changes in upwelling are associated with the slackening of the easterly trade winds in a warming climate [*Ridder and England*, 2014; *Vecchi et al.*, 2006]. This is confirmed by the sensitivity experiment with the weakening of the trade winds show ~ 1% decrease in export production, due to the reduced upwelling and nutrient supply from the interior ocean. Ocean warming alone does not significantly contribute to the decrease in export production in the sensitivity experiment (see Figure 3.11, Warm), but when all the climatic forcing are applied together export production decreases about 10% in MITgcm-ALL, significantly larger than sole effect of the weakening of the tropical trade wind, which indicates a combined non-linear effect.

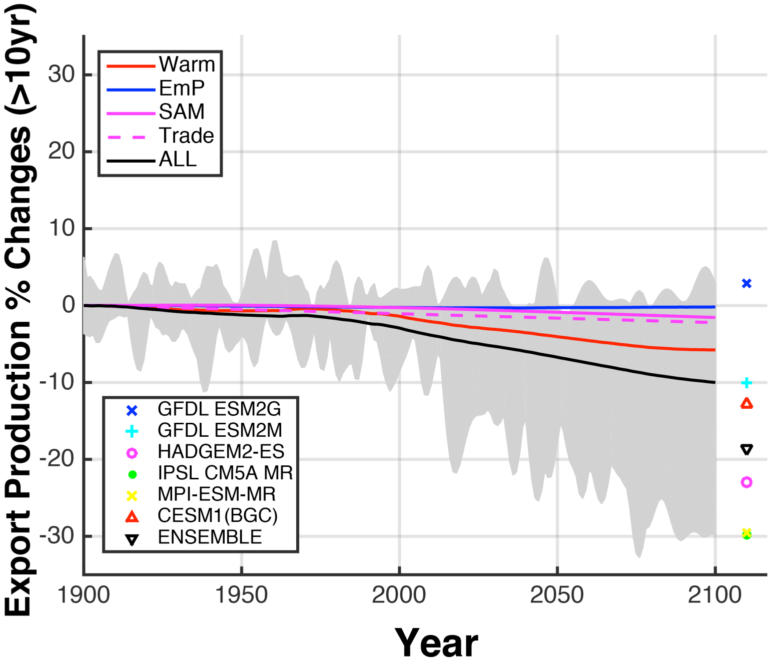

Figure 3.11. Fractional changes in the equatorial Pacific Ocean (between 4°S-4°N) export production at 100m (116m for MITgcm). Fractional changes are relative to the average values of export production from 1900-1930 for CMIP5 model outputs (in shadings). For the sensitivity experiments, fractional changes are based on differences from the control (Red = warming, Blue = freshwater, Magenta = Southern Ocean wind, Dotted Magenta = Tropical trade wind, and Black solid = all forcing). We applied 10-years of low-pass filter for all time series to focus on low-frequency changes in export production for CMIP5 model outputs. Fractional changes for selected CMIP5 models at 2100 are shown as colored shapes.

3.4.4 Causes of the centennial decline in the low-latitude AOU: Water mass age

In this section, we examine the age of the water in the tropical thermocline. The coarse-resolution configuration of MITgcm is computationally efficient, allowing long integrations of the ideal age tracer to reach a full steady state. Figure 3.12 shows the global maps of ideal age tracer in the main thermocline from the sensitivity experiments. In the mean state, tropical oceans (especially in the tropical Pacific Ocean) are characterized by relatively old water age (~500 years) compared to the other regions (Figure 3.12, CTL). Greater water age reflects relatively weak ventilation allowing biological oxygen utilization to deplete O_2 there.

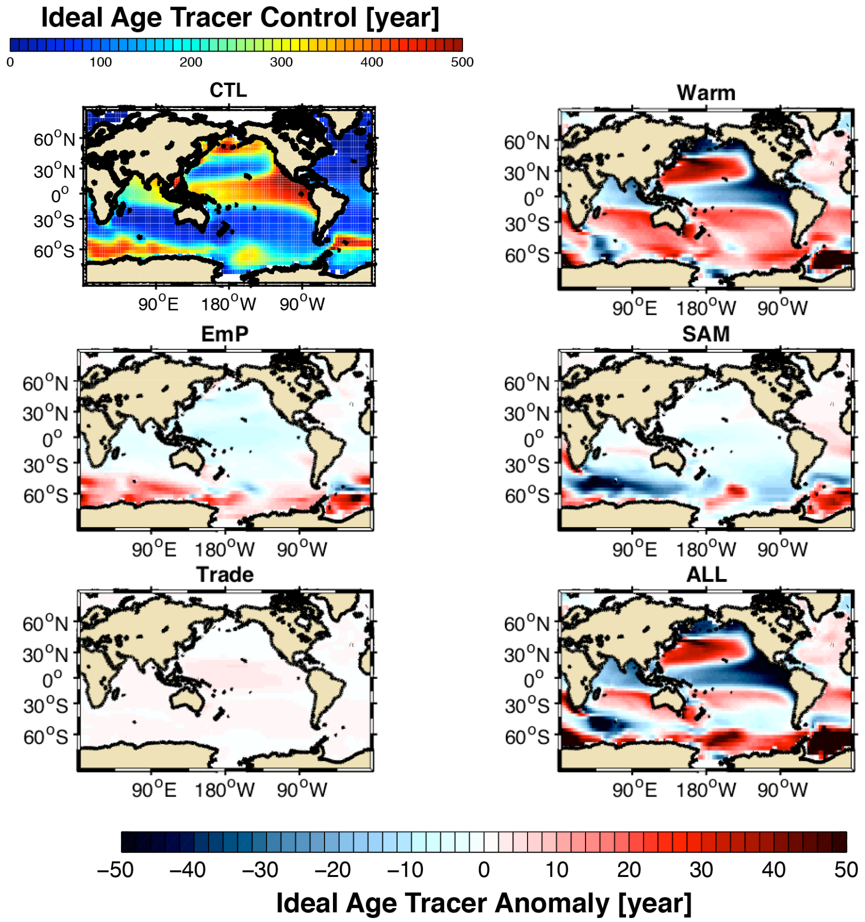

Figure 3.12. Global maps of thermocline ideal age tracer (vertical mean from 160m-610m) from a suite of sensitivity experiments. The CTL (top left panel) shows ideal age tracer from the control experiment. The rest of the panels (Warm, EmP, SAM, Trade, and ALL) show ideal age tracer anomalies (difference from CTL) from a suite of sensitivity experiments.

When all climatic perturbations are imposed, strong negative anomalies of ideal age tracer occur over the tropical thermocline (Figure 3.12, ALL). In contrast, positive anomalies occur in mid latitudes and in the Southern Ocean. The strongly negative changes in the tropical thermocline are due to the combined effects of ocean warming, enhanced freshwater forcing and the Southern Ocean winds (Figure 3.12, Warm, EmP, and SAM). The age anomalies from freshwater forcing experiment (EmP) also exhibit increase in Southern Ocean age, which could be the effect of changes in deep convection also mentioned by previous studies (e.g., *de Levergne et al*., 2014). The model could be in an unstable equilibrium and the small freshwater changes are efficient enough to change convection in the Weddell Sea. The effect of reduced trade wind slightly increases the ideal age tracer in the tropical Pacific Ocean, which partially compensates the effects of other climatic forcing. Ocean warming contributes the most to the decrease in ideal age tracer, which needs explanation. One possible explanation could be the weakened upwelling of deep water, possibly caused by the slowdown of deep overturning circulation induced by increased thermal stratification and enhanced freshwater forcing [*Gnanadesikan et al.,* 2007] and the changes in the ventilation pathway [*Gnanadesikan et al.*, 2012]. In addition, a stronger, poleward-shifted westerly wind increases the subduction and ventilation of thermocline from the southern mid latitudes. The net effect of all the climatic forcing is a net decrease in the ideal age and *AOU* averaged over the tropical thermocline. The other possible explanation could be the effect of the deepening of the isopycnal layers. Analyzing the changes along an isopycnal surface could further illustrate the causes of decline of the age and *AOU* in the tropical thermocline.

We compare the changes in ideal age tracer at a constant depth (at 435m, Figure 3.13) and isopycnal coordinates (along the constant density at $\sigma_\theta = 26.5$, Figure 3.14). We chose these depth and potential density due to its proximity to the core of the oxygen minimum zones of the tropical Pacific Ocean [*Karstensen et al.,* 2008]. Overall the basin-scale structures of the ideal age tracer are similar between the two coordinates, where the ventilated subtropical thermocline is significantly younger than the unventilated tropical thermocline [*Luyten et al.,* 1983] as shown by the CTL experiment in Figure 3.13 and 3.14. The strong gradient of the ideal age tracer exists at about 20°S and 20°N.

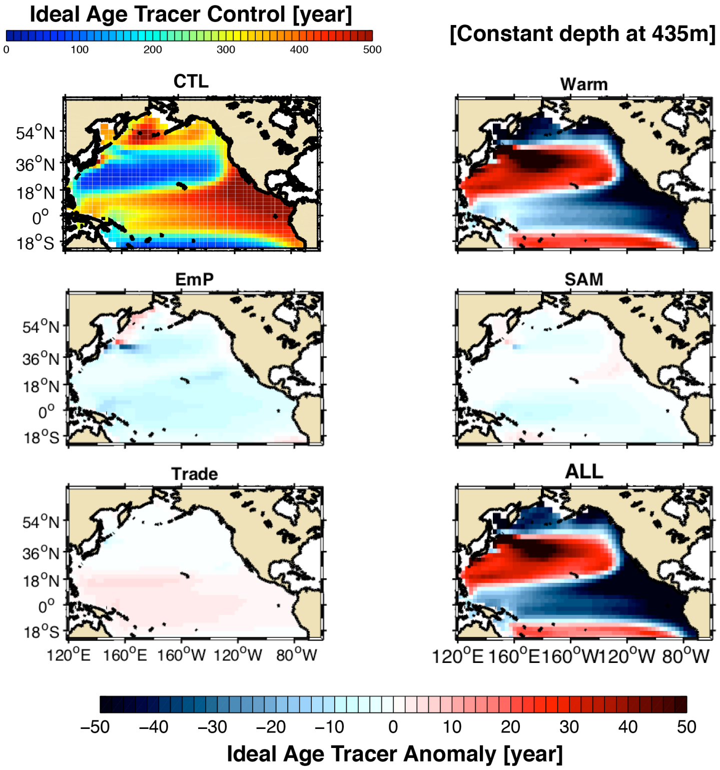

Figure 3.13. Ideal age distribution in the tropical and North Pacific Ocean from a suite of perturbation experiments on constant depth (at 435m). CTL (the left top panel) shows ideal age from the control experiment. The rest of the panels (Warm, E-P, SAM, Trade, and ALL) show ideal age anomaly relative to control experiment.

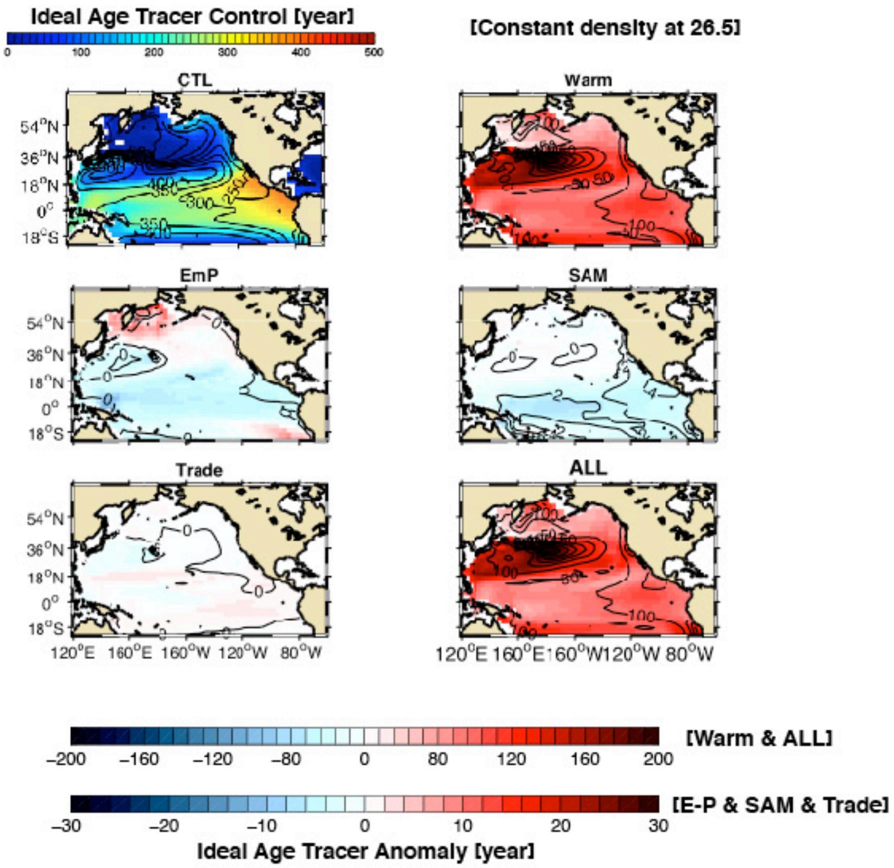

Figure 3.14. The same as in Figure 3.13, except for ideal age tracer on isopycnal layer (at $\sigma_\theta = 26.5$). The contour shows the isopycnal layer depth (mean values for CTL and anomaly from CTL for each sensitivity experiments). Note that color scale is different for Warm and ALL experiments.

The ocean warming causes the most pronounced effect on the ideal age tracer in the tropical Pacific Ocean (Figure 3.13, Warm). Ocean warming results in more than 50 years of decrease in ideal age tracer at 435m in the tropical Pacific Ocean, consistent with the vertically averaged changes (Figure 3.12). Enhanced hydrological cycles (Figure 3.13, E-P) and the Southern Ocean wind (Figure 3.13, SAM) also contribute to the decrease in ideal age tracer (~ 10 years) in the tropical Pacific Ocean but the magnitudes are small compared to the effect of ocean warming. Weakening of trade wind results in an increase in the ideal age tracer (~ 10 years). The net effect is a decrease in the ideal age tracer in the tropical Pacific Ocean when evaluated at 435m-depth.

In contrast, the ideal age tracer on the isopycnal layer increases at all latitudes (Figure 3.14, ALL). The sensitivity experiments reveal that the effect of ocean warming contributes the most to the increase in the ideal age tracer. The magnitude of increase in the ideal age tracer is enhanced in the subtropical gyre regions (150-200 years) close to the region of water mass formation [*Suga et al.,* 1997; *Hanawa and Talley,* 2001; *Xu et al.,* 2012]. The weakening of trade wind reinforces the effect of ocean warming effect in increasing the ideal age tracer in the eastern tropical Pacific. Enhanced hydrological cycles (Figure 3.14, E-P) and stronger Southern Ocean wind (Figure 3.14, SAM) together decrease the ideal age tracer (~ 5 years) in the tropical Pacific Ocean, but their magnitudes is much smaller compared to the ocean warming effect.

The changing depth of the isopycnal surface must explain the different response of the ideal age tracer to the ocean warming. Reduced ventilation tends to increase the ideal age tracer on the isopycnal surface. The changes at a constant depth are due to the shift in the position of the isopycnal layer. Following a constant potential density surface, the effect of warming shifts the position of isopycnal layers deeper into the interior ocean. This indicates that relatively lighter and younger water masses from the upper ocean subside into the intermediate depth, leading to the decreasing ideal age when the changes are measured at a constant depth. CMIP5 model projections as well as MITgcm-ALL show about 100m of deepening isopycnal layers in the tropical Pacific Ocean (for σ_θ = 26.5, see Figure 3.14 and 3.15). The mean isopycnal layer depth (for σ_θ = 26.5) varied between 165m – 360m for selected CMIP5 models and the mean values of about 300m for our control experiments (see Figure 3.14). Sensitivity experiments confirm the dominant role of ocean warming in deepening the isopycnal layers. Thus the simplest explanation for the decreasing age of the tropical thermocline at 435m-depth may be the downward shift of the relatively younger water masses.

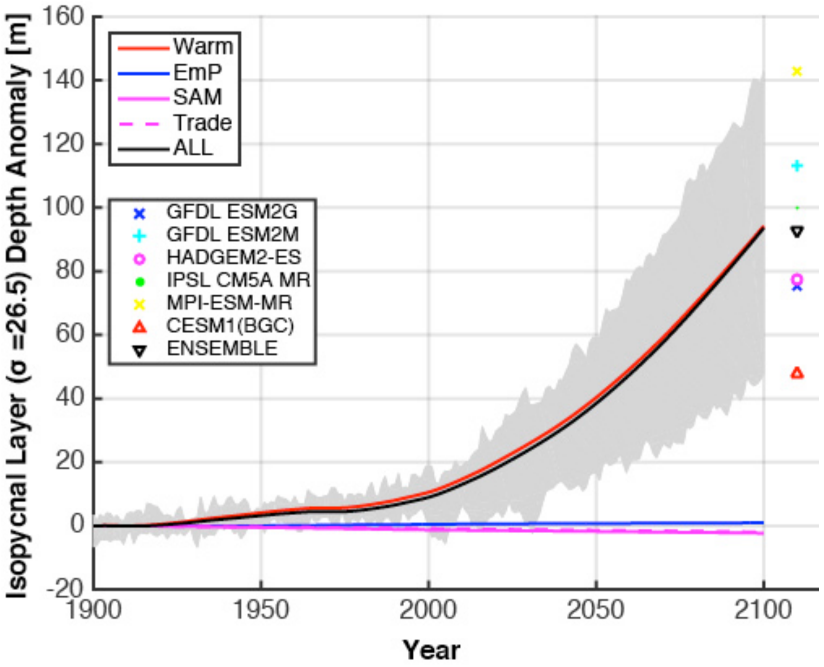

Figure 3.15. Changes in isopycnal layer depth (at $\sigma_\theta = 26.5$, in the unit of meter) from a suite of sensitivity experiments and CMIP5 models (gray shadings). For the sensitivity experiments, isopycnal later depths are based on differences from the control (Red = warming, Blue = freshwater, Magenta = Southern Ocean wind, Dotted Magenta = Tropical trade wind, and Black solid = all forcing). Isopycnal layer depth changes for selected CMIP5 models at 2100 are shown as colored shapes.

3.4.5 Isopycnal analysis of the thermocline O_2

The analysis of the ideal age tracer indicates the critical importance of the vertical coordinates in evaluating long-term ocean deoxygenation as isopycnals can shift significantly over the centennial timescales. Water mass age and *AOU* have strong vertical gradients in the tropical thermocline, and the vertical displacement of the isopycnals can cause apparent change at constant depth. Thus we revisit the centennial O_2 changes contrasting the two vertical coordinates at 435m depth and at $\sigma_\theta = 26.5$ surface. Figure 16 shows side-by-side comparison of the changes in O_2, $O_{2,sat}$, and *AOU* at 435m depth and at $\sigma_\theta = 26.5$ in the Pacific basin. In the Kuroshio extension region O_2 decreases and AOU increases both at 435m depth and at $\sigma_\theta = 26.5$, reflecting the effect of reduced ventilation due to the upper ocean warming. $O_{2,sat}$ at 435m gradually decreases (~ 10 mmol/m^3) over the Pacific basin because of the increasing temperature. In contrast $O_{2,sat}$ along the isopycnal increases moderately (~ 5 mmol/m^3) due to the temperature decrease in the tropical and subtropical regions. Increased upper ocean stratification decreases the subduction of thermocline water masses from the subtropical surface into the interior ocean [*Xu et al*., 2012], and the reduced subduction of relatively warm and saline mode waters decrease the temperature of isopycnal surface. This leads to a slight increase in the $O_{2,sat}$ along the isopycnal surface. The $O_{2,sat}$ in subpolar region, in contrast, decreases due to the temperature increase there.

In low latitudes, changes in O_2 exhibit an opposite response between the two vertical coordinates. O_2 increases by about 15 mmol/m^3 at 435m depth but decreases by about 30 mmol/m^3 at $\sigma_\theta = 26.5$ in the eastern tropical Pacific Ocean. These contrasting changes are dominated by the changes in *AOU* (see Figure 3.16, bottom panels). The opposite responses of *AOU* between the two coordinates can be explained by the downward shift of the isopycnal (Figure 3.15), consistent with the changes of ideal age tracer in the previous section (Figure 3.14). Along the isopycnal layer, the ideal age tracer increases because of reduced ventilation of the thermocline water masses. However, the effect of ocean warming deepens the relatively less dense and young water masses downwards in the water column. The long-term change evaluated at constant depth therefore shows the progressive decline of water age even if the rate of along-isopycnal ventilation is decreasing. Similarly, *AOU* along the isopycnal layer increases under ocean warming but its expression at constant depth can show the opposite response (Figure 3.16, bottom panels). *AOU* changes along the isopycnal layer from CMIP5 future projections show similar behavior (figure not shown).

As we discussed in section 3.4.3, the export production in the tropical Pacific region also decreases primarily due to the ocean warming (see Figure 3.11), which reduces the oxygen utilization rate (*OUR*). Vertical shift of isopycnal layers (Figure 3.15) also change the *OUR* along the isopycnal because the concentration of sinking organic matter generally decreases downward. Reduction in the export of organic matter from the surface and the downward displacement of isopycnal layers together decreases *OUR*, which could partially compensate the effect of weakened ventilation. The biological and physical changes are compensating one another. The net effect is dominated by the ventilation effect in increasing in the *AOU* along the isopycnal surface (Figure 3.16). What are the quantitative changes in *AOU* arising from physical (i.e. ventilation) and biological (i.e. *OUR*) changes? In the next section we quantify the physically and biologically driven *AOU* changes for further evaluations.

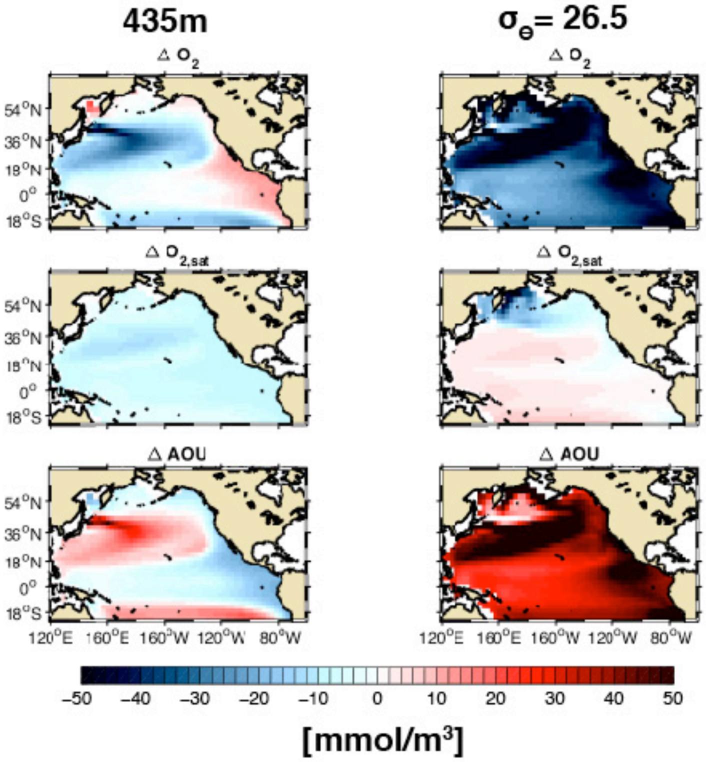

Figure 3.16. Changes in dissolved oxygen concentration, oxygen saturation, and apparent oxygen utilization from ALL experiment relative to control experiment. Left panels show changes on constant depth (at 435m) and right panels show changes along the isopycnal ($\sigma_\theta = 26.5$).

3.4.6 Quantification of Physically and Biologically driven AOU

We conduct additional sensitivity experiments using MITgcm to separate and quantify the physical and biological control on the *AOU* change of the tropical thermocline. The *AOU* decomposition is similar to the method from *Deutsch et al*., [2006] but slightly different approach. For each sensitivity run (A-E), an additional simulation is performed with a reference constant biological productivity (i.e., biological productivity from control experiment). By fixing the biological productivity, the climate change impacts on the biological O_2 consumption are suppressed in these additional sensitivity experiments. To implement this, we record the monthly climatology of *OUR* from the control simulation. Then, the additional sensitivity runs are performed with the climatological *OUR*, thus allowing us to isolate the circulation-driven *AOU* changes, ΔAOU_{phys}. Biologically driven *AOU* changes, ΔAOU_{bio}, can then be estimated by taking the residual between the total and the circulation-driven *AOU* change assuming the linearity between the physically and biologically driven *AOU*.

$$\Delta AOU^{n} = \Delta AOU^{n}_{phys} + \Delta AOU^{n}_{bio} \qquad (3.2)$$

where the superscript *n* indicates the climate forcing (A-E) described in section 3.2. Figure 3.17 shows the spatial pattern of ΔAOU_{phys} and ΔAOU_{bio} at 435m depth and at $\sigma_\theta =$ 26.5 surface. The pattern of ΔAOU_{phys} shows a strong increase in the subtropical oceans reflecting the weakened subduction of thermocline waters (Figure 3.17, top panels). ΔAOU_{phys} in the tropical Pacific Ocean shows a clear difference between depth (at 435m) and isopycnal ($\sigma_\theta = 26.5$) coordinates. At 435m, ΔAOU_{phys} decreases but it increases in the $\sigma_\theta = 26.5$ surface in the tropical thermocline. The patterns of ΔAOU_{phys} (Figure 3.17) essentially mirror that of ideal age tracer shown in Figure 3.14 and 3.15. The apparent decrease of ΔAOU_{phys} at 435m is explained by the deepening of isopycnal layers. In contrast, ΔAOU_{bio} uniformly decreases both at at 435m depth and at $\sigma_\theta = 26.5$ surface, due to the reduced biological oxygen consumption. Generally the magnitude of ΔAOU_{bio} is smaller than the ΔAOU_{phys} so the net change in AOU is physically driven.

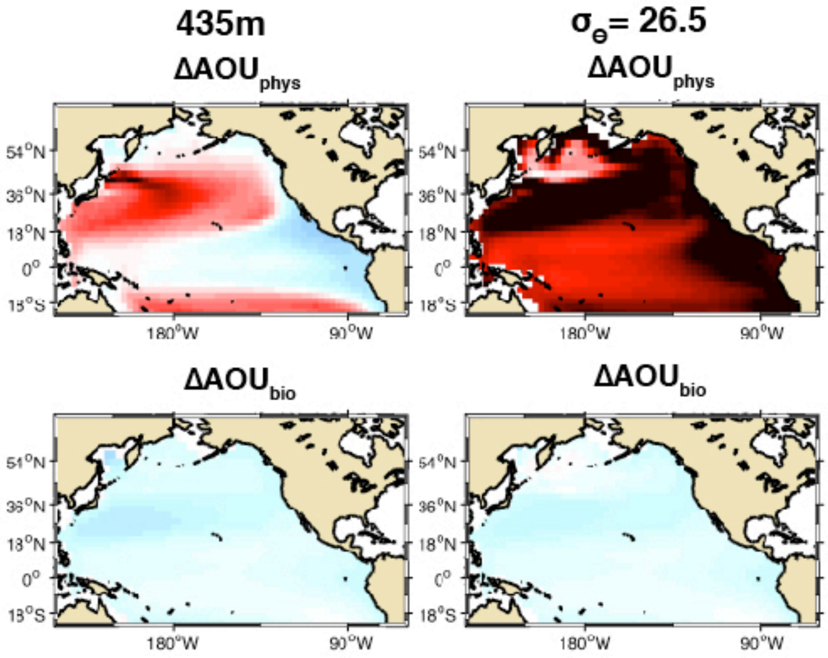

Figure 3.17. Physically (ΔAOU_{phys}) and biologically (ΔAOU_{bio}) driven *AOU* from ALL experiment (relative to control experiment) after 200 years of model integration. Left panels show ΔAOU_{phys} and ΔAOU_{bio} at 435m and right panels show ΔAOU_{phys} and ΔAOU_{bio} along $\sigma_\theta = 26.5$.

Relative magnitude of ΔAOU_{phys} and ΔAOU_{bio} can be visualized in a phase diagram (Figure 3.18) where the horizontal and vertical axis measures spatially averaged ΔAOU_{phys} and ΔAOU_{bio} in the tropical Pacific Ocean. At 435m, ocean warming mainly drives the ΔAOU decrease (Figure 3.17, top left panel). The weakening of the tropical Pacific trade wind has almost no effect. The effect of ocean warming primarily reduces both ΔAOU_{phys} (about 3.6 mmol/m^3) and ΔAOU_{bio} (about 4 mmol/m^3), leading to the total ΔAOU decrease of about 7.6 mmol/m^3 averaged over the tropical Pacific Ocean. Physically and biologically driven *AOU* almost equally contributes to decrease in *AOU*.

The combined effect slightly decreases ΔAOU_{phys} above the linear sum of the individual effects, which could be from changes in tropical Pacific winds.

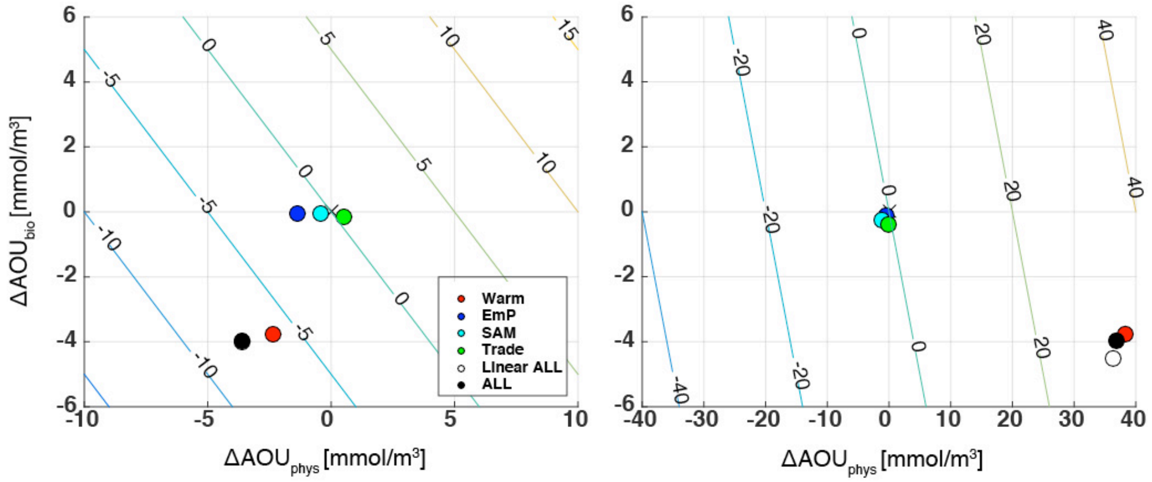

Figure 3.18. A phase diagram explaining ΔAOU as the sum of ΔAOU_{phys} (x-axis) and ΔAOU_{bio} (y-axis) in the tropical Pacific Ocean (rectangular domain in Figure 3.4) after 200 years of model integrations. Left panel shows ΔAOU_{phys} and ΔAOU_{bio} at 435m and right panel shows ΔAOU_{phys} and ΔAOU_{bio} along the isopycnal ($\sigma_\theta = 26.5$). Weighted area-mean values from a suite of sensitivity experiments based on two different coordinates are plotted in colored dots. The non-linearity is negligibly small (compare filled and open black circle). Colored contour lines are the total ΔAOU ($\Delta AOU_{phys}+\Delta AOU_{bio}$). The effects of the ocean heating and the trade wind explain most of the total ΔAOU. Note that x-axis ranges are different between the two panels.

At $\sigma_\theta = 26.5$ surface, the effect of ocean warming strongly increases ΔAOU_{phys} (about 40 mmol/m^3), an order of magnitude larger than that at 435m (Figure 3.17). The effect of ocean warming decreases ΔAOU_{bio}, as a result of reduced export production. Intensification in hydrological cycles (E-P) and westerly wind over the Southern Ocean (SAM) almost has no effect on changing both ΔAOU_{phys} and ΔAOU_{bio} in the tropical

Pacific Ocean. Weakening of trade wind could reduce export production in the equatorial Pacific region but it does not result in robust decrease in basin wide ΔAOU_{bio} in the tropical Pacific Ocean. In summary, the warming-induced ΔAOU_{phys} primarily controls the change in *AOU*, but different aspect of the circulation change is emphasized depending on the vertical coordinate. At constant depth, the effect of the isopycnal deepening dominates the ΔAOU_{phys} whereas at constant potential density the effect of weakened ventilation dominates. The overall magnitude of ΔAOU is significantly greater on the isopycnal surface. The effect of warming could decrease ΔAOU_{bio} about 4 mmol/m^3.

3.5. Summary and Discussion

We investigated centennial changes in the thermocline O_2, especially focusing on the underlying mechanisms using a hierarchy of models. Future projections from CMIP5 ESMs and a suite of sensitivity experiments using MITgcm illustrate the dominant patterns in the evolution of thermocline O_2 under a warming climate. Tropical thermocline O_2 exhibits small changes in centennial time scales as shown by several previous studies [*Bopp et al.*, 2013; *Cabré et al.*, 2015; *Cocco et al.*, 2013]. We conducted a suite of sensitivity experiments to decompose and quantify the simulated O_2 changes into the effects of various climatic forcing, mimicking the centennial climate change projection under the global warming based on previous observations and modeling studies. The small changes in O_2 are primary driven by warming induced decrease in *AOU*. However, this does not necessary mean that tropical oceans are immune from the climate-induced deoxygenation. The apparent compensation between decreasing solubility and decreasing *AOU* results in a relatively small O_2 change in the thermocline. The decreasing *AOU* in the tropical thermocline could be the results of the deepening of upper ocean isopycnals. By sampling progressively lighter isopycnals, the *AOU* appears to decrease (~48% of total *AOU* decrease), and counteracts the effect of warming-induced solubility decrease. Biological productivity decreases under a warming climate, which could almost equally contribute to decrease tropical thermocline *AOU* (~52% of total *AOU* decrease).

The application of hierarchical model approach is able to develop a consistent scenario for the tropical ocean oxygen changes under a warming climate, but our experiments using a coarse-resolution model includes some caveats. The coarse resolution of the sensitivity experiments may not fully represent detailed structures of the equatorial current systems and the effects of ocean eddies and small-scale mixing processes on the distribution of thermocline O_2. It is not yet clear to what extent these unresolved physical processes impact on ocean biogeochemistry on the centennial timescale. Crude representation of biological process and export production can introduce biases in our calculations. For example, *Oschlies et al.,* [2008] illustrates the sensitivity of nutrient stoichiometry to the partial pressure of CO_2 can alter the long-term changes in tropical O_2 in a high-CO_2 climate. Further studies with more sophisticated ecological and biogeochemical model may change the future O_2 projections in unexpected ways.

Significant decreases in the tropical O_2 and the expansion of OMZs are documented in historic datasets from the past several decades [*Helm et al*., 2011, *Keeling et al*., 2010, *Stramma et al*., 2008], which may be due to the interannual and decadal climate variability could be dominating trends in the historic data [*Czeschel et al.*, 2012; *Deutsch et al.,* 2011, 2014]. The decadal-scale trends in the observations should not be confused with the century-scale projection of the ESMs that are potentially driven by different sets of mechanisms. Natural climate variability could significantly modulate the O_2 concentrations on an inter-annual to decadal timescale [*e.g., Ito and Deutsch,* 2013], which makes it a challenging task to detect the long-term change observationally [*Long et al.,* 2016]. Finally, the later half of this study focused on the tropical Pacific Ocean but other tropical oceans require further investigation with regionally specific climatic forcing patterns such as spatial patterns of ocean warming and winds.

CHAPTER 4

UNCERTAIN RESPONSE OF OPEN-OCEAN OXYGEN REFLECTS THE IMBALANCE BETWEEN VENTILATION AND REMINERALIZATION

Abstract

Classic box model studies show that once preformed nutrient is determined, the oxygen deficit relative to saturation (i.e. Apparent Oxygen Utilization, *AOU*) is also set, independent of the rates of ocean ventilation or export production. The balance between ocean vertical exchange and the export and remineralization of organic matter facilitate this remarkable stability. In a more realistic simulation, this balance may be violated, at least regionally through changes in climate and ocean circulations. We analyze the results from a suite of sensitivity experiments using an ocean biogeochemistry model to quantify the competing effects of ventilation and remineralization using the thermocline O_2 as a metric. We perform sensitivity experiments systematically changing vertical tracer diffusivity and evaluate its impact on the mean state as well as the deoxygenation under a warming climate. We separate simulated changes in *AOU* into two parts: a component driven by ventilation and another component driven by remineralization. We find that the two components generally compensate with one another, qualitatively consistent with the box model. However, there are significant regional imbalances that control the evolution of the thermocline *AOU*. One of the prominent regions of this imbalance is the tropical oxygen minimum

zone (OMZ). A highly diffusive thermocline is more susceptible to thermally driven deoxygenation due to stronger heat uptake. *AOU* change plays more important roles under a low diffusivity. In our calculation, the ventilation strength as well as upwelling supply of limiting nutrients controls the regional ventilation-remineralization imbalance. Predicting future deoxygenation in tropical thermocline is highly uncertain as it likely reflects relatively small residuals among multiple physical and biogeochemical processes.

4.1 Introduction

Classic two-box modeling studies show that with the active biological processes, dissolved oxygen concentration (O_2) could be completely depleted in the interior ocean [e.g., *Emerson and Hedges*, 2008]. In modern oceans, anoxic conditions are rare but hypoxic and suboxic conditions still occurs mainly in tropical oceans. One of the key processes maintaining the OMZs in the tropical oceans is the integrated biological consumption of O_2 which maintains the oxygen minimum layer as discussed in early studies [*Sverdrup,* 1938*, Wyrtki,* 1962]. As we introduced in the first chapter, we use Apparent Oxygen Utilization (*AOU*) to estimate the integrated biological consumption of O_2 in the ocean. The *AOU* is defined as the difference between oxygen saturation and in-situ oxygen distributions [*Broecker*, 1974, *Broecker and Peng*, 1982],

$$AOU = O_{2,sat}(T,S) - O_2 \qquad (4.1).$$

Here $O_{2,sat}$ is the oxygen saturation (known function of temperature (T) and salinity (S)) and O_2 is the in-situ dissolved oxygen concentration. Here we are assuming that $O_{2,sat}$ is close to equilibrium at the surface. *AOU* is the measurement of O_2 consumed in the interior ocean by respiration since it was last contact with the atmosphere. The *AOU* depends on both ventilation (i.e. water mass age) and local biological productivity and remineralization rate (i.e. Oxygen Utilization Rate (*OUR*)). Therefore, *AOU* is related to both water mass age and *OUR* expressed as follows.

$$AOU \simeq age \times OUR \qquad (4.2)$$

Pytkowicz [1971] discussed the interpretation of *AOU* that it is not only determined by the biological oxygen utilization but also mixing of water masses. In a most precise sense, *AOU* is a path integral of *OUR* along the ventilation pathway. Equation (4.2) is an approximation assuming the *OUR* reflects its Lagrangian mean. While this is a useful decomposition for theoretical exploration, in practical terms water mass age and Lagrangian mean *OUR* are not directly observable.

Figure 4.1 shows the global map of annual mean climatology of *AOU* in the intermediate depth (400m) close to the core of the OMZs. High *AOU* is dominating in the tropical oceans, indicating the dominant role of integrated biological consumption.

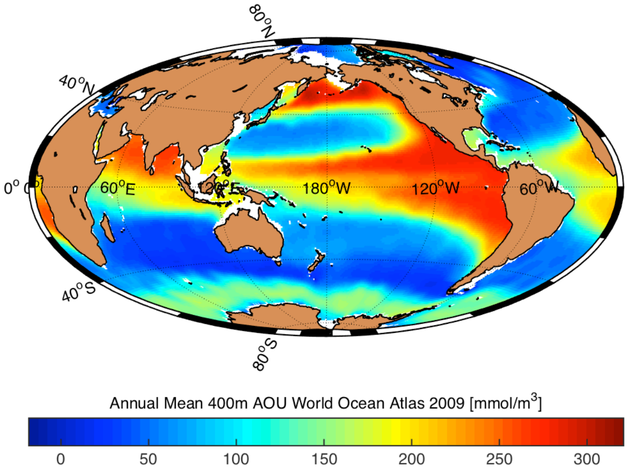

Figure 4.1. Annual mean climatology of Apparent Oxygen Utilization (*AOU*) at 400m from the *World Ocean Atlas* 2009.

What are the key-processes regulating the size and intensity of the OMZs in the tropical oceans? What are the characteristics of interplay between ventilation and remineralization controlling the low oxygen environment? We first illustrate some of the fundamental balances regulating O_2 and *AOU* changes based on a simple box model [e.g., *Broecker and Peng*, 1982*, Emerson and Hedges*, 2008].

4.2 Apparent Oxygen Utilization balance in a two-box model

We first derive macronutrient (here we think of phosphate) and O_2 balance in the two-box system describing the tracer concentrations in the surface and interior oceans

(Figure 4.2). The two well-mixed reservoirs exchanges nutrient and oxygen via vertical transport and export production (i.e. sinking organic matter). We assume that sinking organic matter is fully remineralized and produces inorganic nutrients in the interior box. In this system the surface nutrient is equal to the preformed nutrient for the deep reservoir, which is prescribed to a specific value.

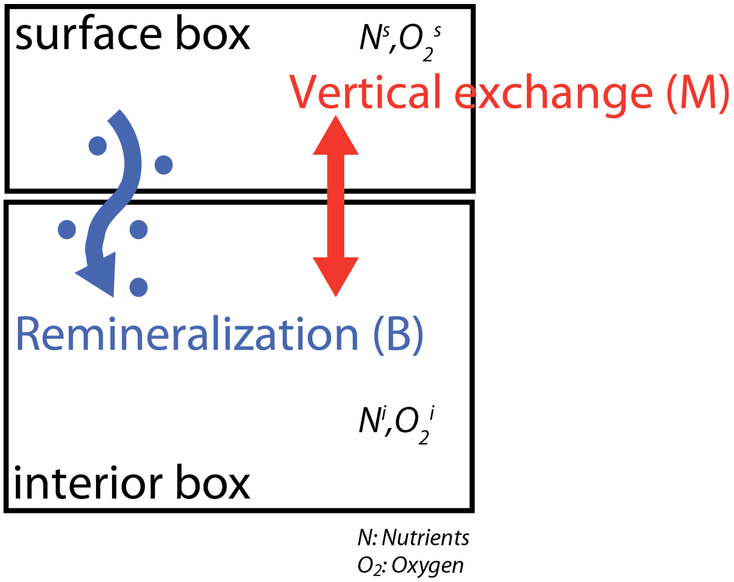

Figure 4.2. A schematic diagram of two-box model representing the O_2 and nutrient cycles.

The temporal evolution of nutrients and O_2 in the interior box could be written as,

$$\frac{dN^i}{dt} = M(N^s - N^i) + B \qquad (4.3)$$

$$\frac{dO_2^i}{dt} = M(O_2^s - O_2^i) + RB \qquad (4.4)$$

In equations (4.3) and (4.4), N and O_2 represent macronutrient and dissolved oxygen, respectively. M represents the vertical transport (in the unit of m^3/s), and B represents the export production, and R is the stoichiometric ratio between oxygen and macronutrient. Superscript s and i represent the surface and interior box ocean, respectively. For the steady state, we can write AOU in the interior box as,

$$AOU^i = R(N^i - N^s) \qquad (4.5)$$

$$AOU^i = R(N_{total} - N_{pre}) = RN_{reg} \qquad (4.6)$$

In equation (4.6), N_{pre} and N_{reg} are the preformed nutrient and regenerated nutrient, respectively. If we think of the case that surface nutrients are completely depleted (i.e. N^S $N_{pre} = 0$, oligotrophic regime) by biological processes, equation (4.5) can be written as,

$$AOU^i = RN^i = RN_{reg} = constant \qquad (4.7)$$

In this limit the nutrients in the interior box is completely regenerated which maximizes AOU [*Ito and Follows*, 2005]. When surface nutrients (i.e. preformed nutrients) are not completely depleted, it will lead to reduce the amount of AOU. Thus AOU in the interior box is essentially controlled by the preformed nutrient, rather than detailed changes in vertical transport or remineralization. Preformed nutrient in turn depends on the surface nutrient in the water mass formation regions. At steady state, the global O_2 deficit relative to saturation (i.e. AOU) can be considered independent of the rates of ocean ventilation (M) or export production (B).

This link between preformed nutrient and *AOU* holds for the constant uniform stoichiometry and the constant nutrient inventory. Under these conditions, the ventilation supply and remineralization loss of O_2 fully cancel out one another. Obviously, these constraints do not apply regionally. This raises further questions: Can this principle apply for a regional ocean biome within a relatively uniform oceanographic condition? What are the mechanisms stabilizing the *AOU*? In this chapter, we evaluate the regional balance of the physically and biologically driven *AOU* from a suite of sensitivity experiments based on ocean circulation and biogeochemistry model.

4.3 Design of sensitivity experiments

The basic model setting is the same as in studies from Chapter 3 and *Ito et al.,* [2015]. We employ the Massachusetts Institute of Technology general circulation model (MITgcm) [*Marshall et al*., 1997a, b] with a simple biogeochemistry component [*Dutkiewicz et al*., 2005; *Parekh et al*., 2005]. The model additionally carries an ideal age tracer to diagnose water mass age. The model has a global bathymetry in a 2.8°×2.8° longitude-latitude grid, and 23 non-uniform vertical levels with increased resolution near the surface. Here we conduct a suite of sensitivity experiments by purposefully changing the vertical diffusion coefficients (i.e. which may be analogues to changing the vertical transport (*M*) in two-box model system). Vertical diffusion coefficient is prescribed by the scheme from *Bryan and Lewis* [1979]. We perturb background vertical diffusion coefficients (*Kv*) in the upper 2000m. Values of *Kv* used in sensitivity experiments ranges from 0.05 – 1.3 cm^2/s. The control value of *Kv* is set to 0.3 cm^2/s, the same as the experimental settings in Chapter 3. We mainly focus on discussing the difference in response relative to the control experiment.

We spin-up the model with a wide range of background vertical diffusion coefficients and then evaluated thermocline O_2 at new steady states. Similar to the method used in Chapter 3, we have again separated AOU into physically (ΔAOU_{phys}) and biologically (ΔAOU_{bio}) driven AOU for further analysis.

4.4 Results

4.4.1 Dependence of dissolved oxygen concentrations on vertical mixing

Tropical Pacific OMZ show particularly interesting sensitivities to perturbation of vertical mixing [*Duteil and Oschlies*, 2011]. Figure 4.3 shows the dependence of hypoxic and suboxic volume on vertical diffusion coefficients based on a suite of sensitivity experiments. Sensitivities in hypoxic and suboxic volumes with respect to vertical diffusion coefficients show differences between the Pacific Ocean and Indian Ocean as indicated by *Duteil and Oschlies*, [2011]. Hypoxic and suboxic volumes maximize around $Kv = 0.3$ cm^2/s in the Pacific Ocean, while hypoxic and suboxic volumes shows increase with respect to enhanced vertical mixing in the Indian Ocean. What are the underlying mechanisms regulating low O_2 in the OMZs? What are the differences in regulating mechanisms in these two regions?

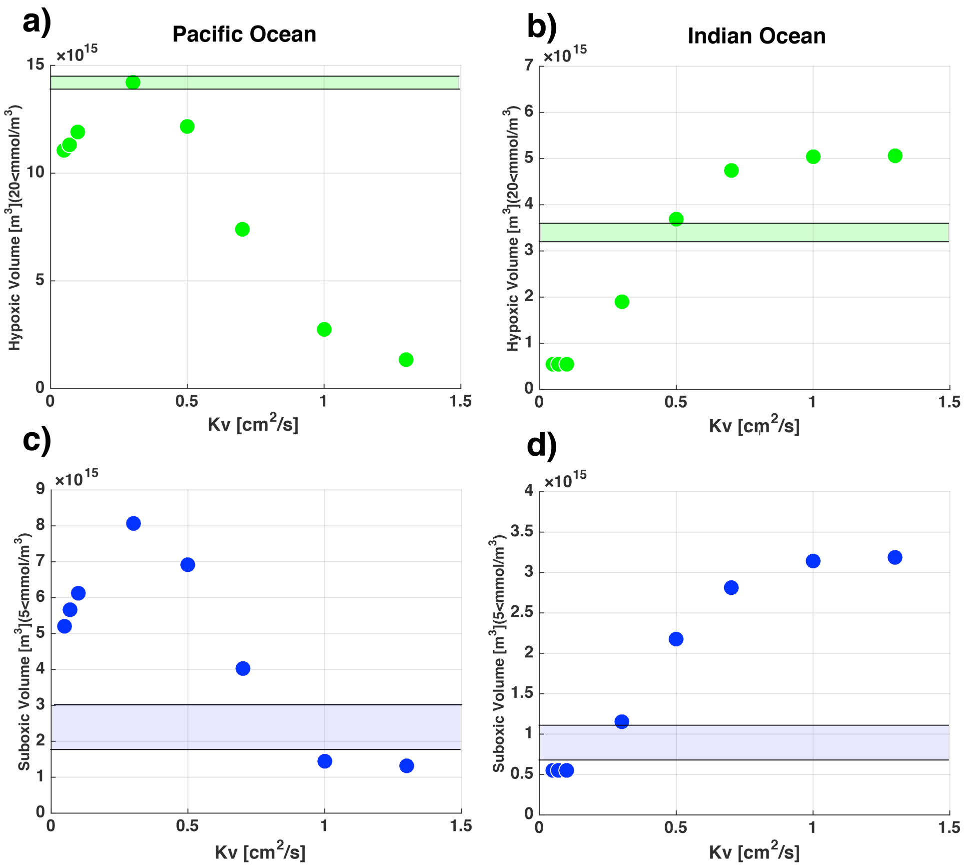

Figure 4.3. Hypoxic (a and b) and suboxic volume (c and d) in the Pacific Ocean (north of 35S) and the Indian Ocean (north of the equator), upper 850m (similar to the analysis of *Duteil and Oschlies*, [2011]) from sensitivity experiments. Hypoxic and suboxic volumes are based on dissolved oxygen concentrations smaller than 20 mmol/m^3 and 5 mmol/m^3 following *Bianchi et al*., [2012]. Green shadings show observed hypoxic and suboxic volume range from *Bianchi et al*., [2012].

Figure 4.4 shows the global maps of ΔO_2, $\Delta O_{2,sat}$, and ΔAOU from a suite of vertical diffusion experiments. Hereafter Δ represents the difference between the sensitivity experiments and the control experiment (Kv = 0.3 cm^2/s). The tropical Pacific Ocean exhibits O_2 increase in the main thermocline for both low and high vertical diffusivity. For the case of intermediate vertical diffusivity (Kv = 0.5 cm^2/s), ΔO_2 exhibit almost no change or slight decrease in the tropical Pacific Ocean, indicating a shift in ΔO_2 sensitivity around CTL value (Kv = 0.3 cm^2/s). This is consistent with the previous modeling studies by *Duteil and Oschlies* [2011]. Thermocline ΔO_2 linearly increases with decreasing vertical diffusions (i.e. low vertical diffusivity leads to increase in ΔO_2 and vise versa), which is opposite to other tropical oceans (Figure 4.4, left panels). Tropical Atlantic Ocean shows similar response as in the Indian Ocean but the changes in thermocline ΔO_2 is much smaller compared to the Indian Ocean. The high latitudes Southern Ocean also behaves differently from tropical oceans. Thermocline ΔO_2 increases with vertical diffusivity in the southern high latitudes, which could be a result from enhanced ventilations.

The response of thermocline O_2 to the variation in vertical mixing is non-linear, in particular for the tropical Pacific Ocean. What makes the tropical Pacific Ocean unique and different from other tropical oceans? We address this question by first decomposing changes in ΔO_2 into solubility-driven component ($\Delta O_{2,sat}$) and biologically-driven component (ΔAOU) which could be written as,

$$\Delta O_2 = \Delta O_{2,sat} - \Delta AOU \qquad (4.13).$$

Middle panels in Figure 4.4 show changes in $\Delta O_{2,sat}$ from a suite of vertical diffusion experiments. Thermocline $\Delta O_{2,sat}$ decreases when vertical diffusion increases due to enhanced heat uptake into the interior ocean. Low vertical diffusion leads to decrease in heat uptake from the upper ocean, decreasing temperature and increasing $\Delta O_{2,sat}$ of the main thermocline. The changes in $O_{2,sat}$ are almost spatially uniform across the three basins, suggesting that changes in *AOU* determines ΔO_2.

Right panels from Figure 4.4 show ΔAOU. In the tropical Pacific Ocean, ΔAOU shows a non-linear response: it decreases under both low and high vertical diffusivity. On the other hand, ΔAOU monotonically increases with vertical diffusivity in the Indian Ocean. The magnitudes of ΔAOU are generally greater than that of $\Delta O_{2,sat}$, determining the net ΔO_2 in the tropical thermocline. The remaining question is what causes ΔAOU to behave differently between the tropical Pacific Ocean and the Indian Ocean? What are the mechanisms behind the non-linear response of ΔAOU in the tropical Pacific Ocean? We further investigate the factors driving ΔAOU changes in the eastern tropical Pacific Ocean and the Indian Ocean.

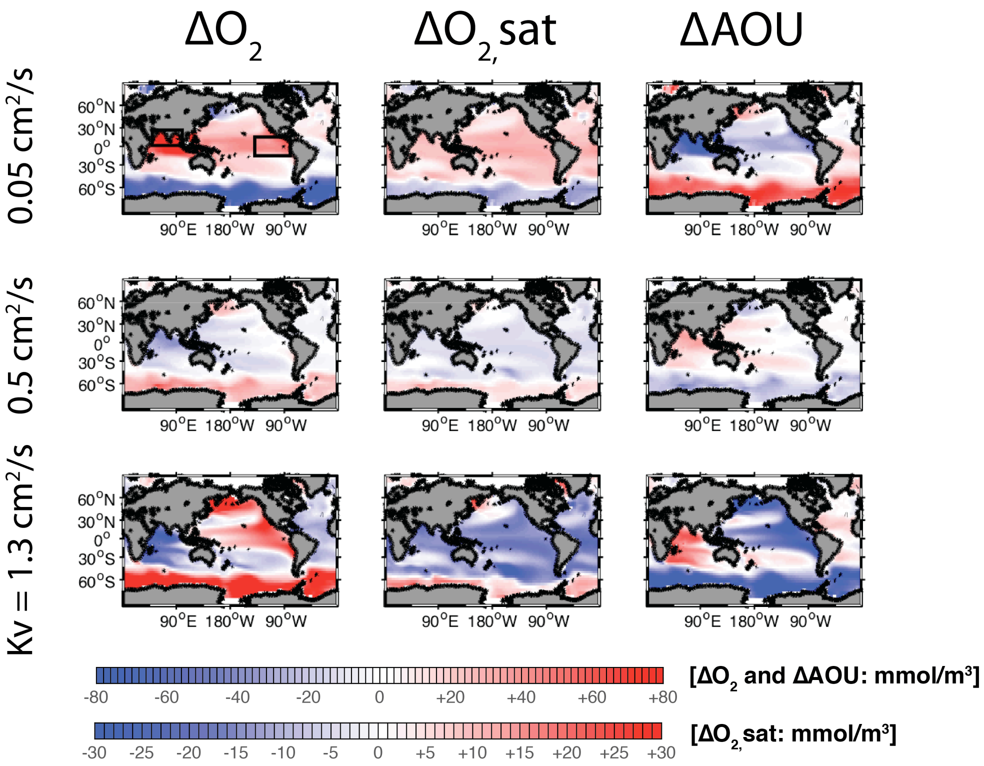

Figure 4.4. Global maps of ΔO_2, $\Delta O_{2,sat}$, and ΔAOU from a suite of vertical diffusion experiments. Delta (Δ) refers to the anomaly from the control experiment. All the tracers are vertically integrated in the thermocline (160m-610m). Black boxes are the areas we are focusing on for calculating weighted-area mean values.

4.4.2 Regional dependence of oxygen saturation and *AOU* on vertical mixing

To further diagnose the sensitivity of thermocline $\Delta O_{2,sat}$ and ΔAOU in the eastern tropical Pacific Ocean and the Indian Ocean, we conducted analysis of volume-weighted averages in the two regions. Horizontal extent of the control volumes are shown in Figure 4.4, top left panel and their depth range is set to 160-610m covering the main thermocline where core of the oxygen minimum zones (OMZs) exists [*Karstensen et al.*, 2008]. The $\Delta O_{2,sat}$ and ΔAOU shows almost no changes for $Kv = 0.5$ cm^2/s in the eastern tropical Pacific Ocean. The case of vertical diffusion coefficients close to CTL case ($Kv =$

0.3 cm^2/s) could be a tipping point where ΔO_2 shows almost no change. Figure 4.5 shows the compensation between $\Delta O_{2,sat}$ and ΔAOU. As expected $\Delta O_{2,sat}$ (Figure 4.5, red marks) monotonically decreases with vertical diffusivity. ΔAOU (Figure 4.5, blue marks) shows the non-linear behavior where it tends to decrease under both low and high diffusivity, responsible for the non-linear response of ΔO_2 in the eastern tropical Pacific Ocean. $\Delta O_{2,sat}$ in the Indian Ocean increases with enhanced vertical diffusivity similar to the eastern tropical Pacific Ocean, but the ΔAOU does not show the tipping point there. Thus we conclude that different sensitivity of AOU in the two regions caused the different sensitivity of $O_{2.}$ Then what are the mechanisms driving ΔAOU in these two regions?

The cause of ΔAOU changes comes from the combined effects of ventilation (which may be measured by water mass age) and remineralization (i.e. Oxygen Utilization Rate (*OUR*)). Low vertical diffusivity could reduce the supply of nutrients from the deep ocean, reducing biological productivity and *OUR*. High vertical diffusivity could increase it. However, changes in vertical diffusivity could also alter the rate at which O_2-rich surface waters mix into the interior ocean. These two factors likely compensated one another as predicted by the simple box model. The sensitivity experiment shows the non-zero ΔAOU, suggesting that the compensation is not complete. What are the conditions that the system can deviate from the full compensation? Can we explain the imbalance between changes in water mass age and nutrients supply? To address these questions, we next analyzed physically- and biologically-driven ΔAOU from the sensitivity experiments.

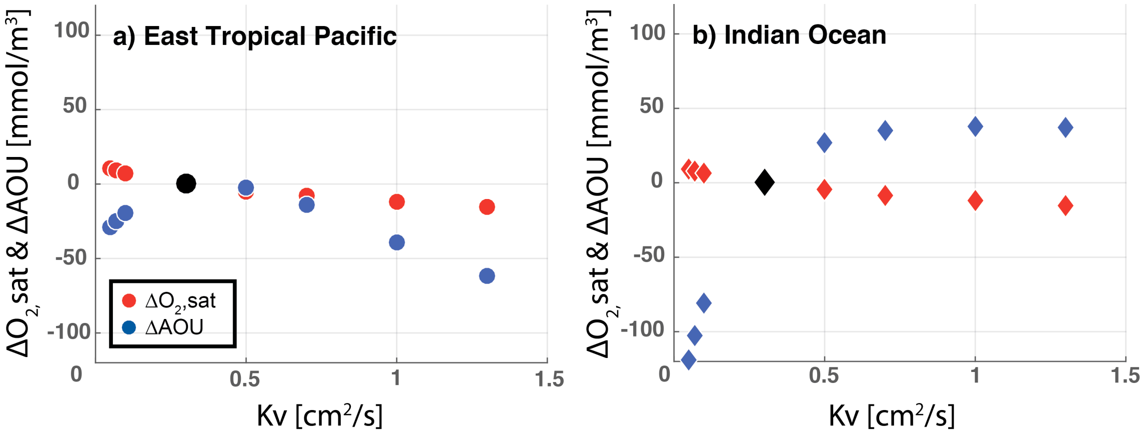

Figure 4.5. Sensitivity of thermocline $\Delta O_{2,sat}$ (red marks) and ΔAOU (blue marks) to various vertical diffusion coefficients in the eastern tropical Pacific Ocean (a) and the Indian Ocean (b). $\Delta O_{2,sat}$ and ΔAOU are base on weighted-area mean values in two regions (black boxes in Figure 4.4, top left panel).

4.4.3 Ventilation vs. remineralization driven AOU

We now examine the response of physically and biologically driven ΔAOU (ΔAOU_{phys} and ΔAOU_{bio}) in the eastern tropical Pacific Ocean and the Indian Ocean. Figure 4.6 shows the thermocline ΔAOU_{phys} and ΔAOU_{bio} dependence on vertical diffusivities. ΔAOU_{phys} shows decrease with increasing vertical diffusivity for both eastern tropical Pacific Ocean and the Indian Ocean. This indicates that water mass age is decreasing in tropical oceans and results in decreasing ΔAOU_{phys} in these regions. Large vertical diffusion ($Kv \sim 1.3$ cm^2/s) will lead to about decreasing ~100 mmol/m^3 of ΔAOU_{phy} in the two regions. In contrast, changes in biologically driven ΔAOU_{bio} are in the opposite sense. ΔAOU_{bio} increase in high vertical diffusivity up to ~50 mmol/m^3 in the eastern tropical Pacific Ocean and ~ 150 mmol/m^3 in the Indian Ocean. Physically and biologically driven ΔAOU compensate each other but the effect of decrease in ΔAOU_{phys} is larger compared to the ΔAOU_{bio} resulting in decreasing overall ΔAOU in the eastern tropical Pacific Ocean. Contrastingly, ΔAOU_{bio} dominates the overall changes in ΔAOU in the Indian Ocean.

The balance between ventilation and remineralization driven AOU shows distinct differences between two regions. The eastern tropical Pacific Ocean is dominated by ventilation but reminarlization dominates in the Indian Ocean. Enhanced vertical mixing decreases ΔAOU_{phys} in both regions and magnitudes are similar (~ 100 mmol/m^3). However, ΔAOU_{bio} in the eastern tropical Pacific Ocean peaks at around ~ 50 mmol/m^3 while ΔAOU_{bio} continuously increasing with vertical diffusivity (~ 150 mmol/m^3). What leads to a limitation in ΔAOU_{bio} in the eastern tropical Pacific Ocean?

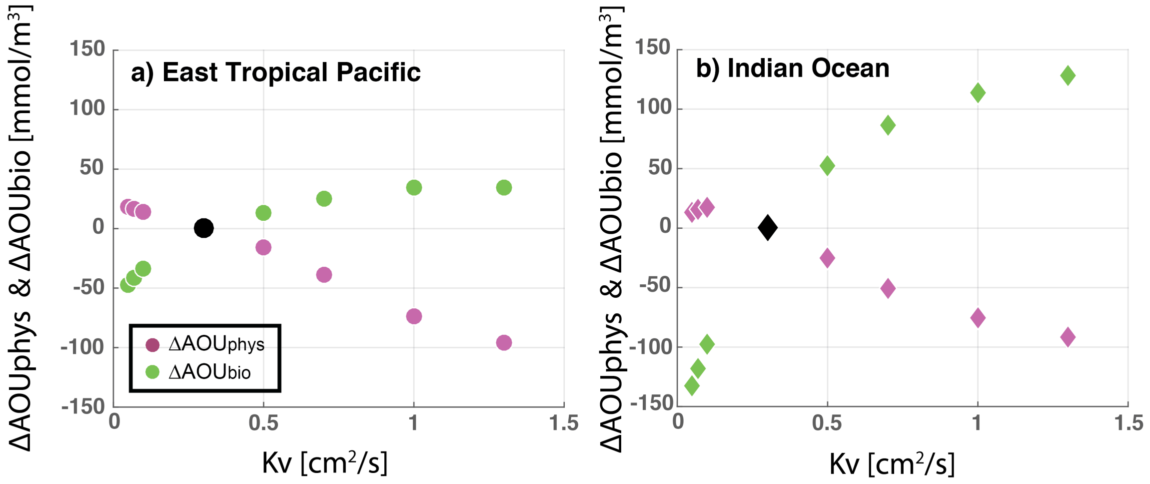

Figure 4.6. The same as in Figure 4.5 except for ventilation and remineralization driven *ΔAOU* (*ΔAOU_{phys}* and *ΔAOU_{bio}*).

4.4.4 What controls ventilation and remineralization driven *AOU* changes in tropical oceans?

Changes in water mass age (Figure 4.7, left panels) show decrease in tropical oceans with respect to increase in vertical diffusivity. Both the tropical Pacific Ocean and the Indian Ocean exhibit decrease in water mass age but the magnitudes are larger in the Pacific Ocean. Decrease in water mass age could be explained by the mechanism proposed by *Gnanadesikan et.al*, [2007]. Increase in vertical diffusivity leads to change the fraction of upper water mass and deep-water mass in tropical oceans. Results indicate the enhanced supply for surface water mass into the main thermocline, leading to decrease in water mass age. This will significantly influence the *ΔAOU* as shown in Figure 4.4 and 4.5.

Changes in export production and nutrients (i.e. phosphorus and iron) will provide us a clue to understand how remineralization changes under various vertical diffusivity. Figure 4.7 (right three panels) show the changes in export production (Δepc at 225m), surface phosphate (ΔPO_4), and iron (ΔFe). The Indian Ocean exhibits increase in export production with increase in vertical diffusivity, driven by the vertical supply of macronutrients shown in Figure 4.7 (right two panels). Phosphate and iron both increases with enhanced mixing in the Indian Ocean. However, export production and nutrients change differently in the eastern tropical Pacific Ocean. Export production increases with enhanced vertical mixing but the changes are weak compared to that of the Indian Ocean. Changes in the export production do not show large differences between the two high vertical diffusivity cases ($Kv = 0.5$ cm^2/s and $Kv = 1.3$ cm^2/s). One possible explanation could be the role of micronutrient (i.e., iron) limitation in the eastern tropical Pacific Ocean. Tropical Pacific Ocean is limited in iron supply and biological productivity may not scale linearly with the supply of macronutrient from the interior ocean. This is evident from the changes in surface phosphate (Figure 4.7, see ΔPO_4 for high vertical diffusivity case) where large positive anomalies of ΔPO_4 appear in the tropical Pacific Ocean, indicating that biological production could not use up the macronutrient supplied from the deep ocean.

Iron limitation could also be important on limiting remineralization-driven AOU (i.e. ΔAOU_{bio}) in eastern tropical Pacific Ocean. In contrast, the Indian Ocean is dominated by the effect of remineralization because there is no limitation by the micronutrient (Figure 4.7, right two panels).

The overall increase in ΔAOU in the Indian Ocean could be a result of enhanced biological production due to the enhanced supply of macronutrient from the deep ocean and it has adequate supply of micronutrients (Figure 4.7). Water mass age decreases but the effect of biological consumption overwhelms this effect, leading to an increase in ΔAOU (i.e. decrease O_2) in the Indian Ocean. On the other hand, tropical Pacific Ocean shows decrease in ΔAOU (Figure 4.4) and this could be a result of large amount of decrease in water mass age in this region. Changes in export production are weaker in the eastern tropical Pacific Ocean compared to the Indian Ocean and this leads to a large decrease in ΔAOU.

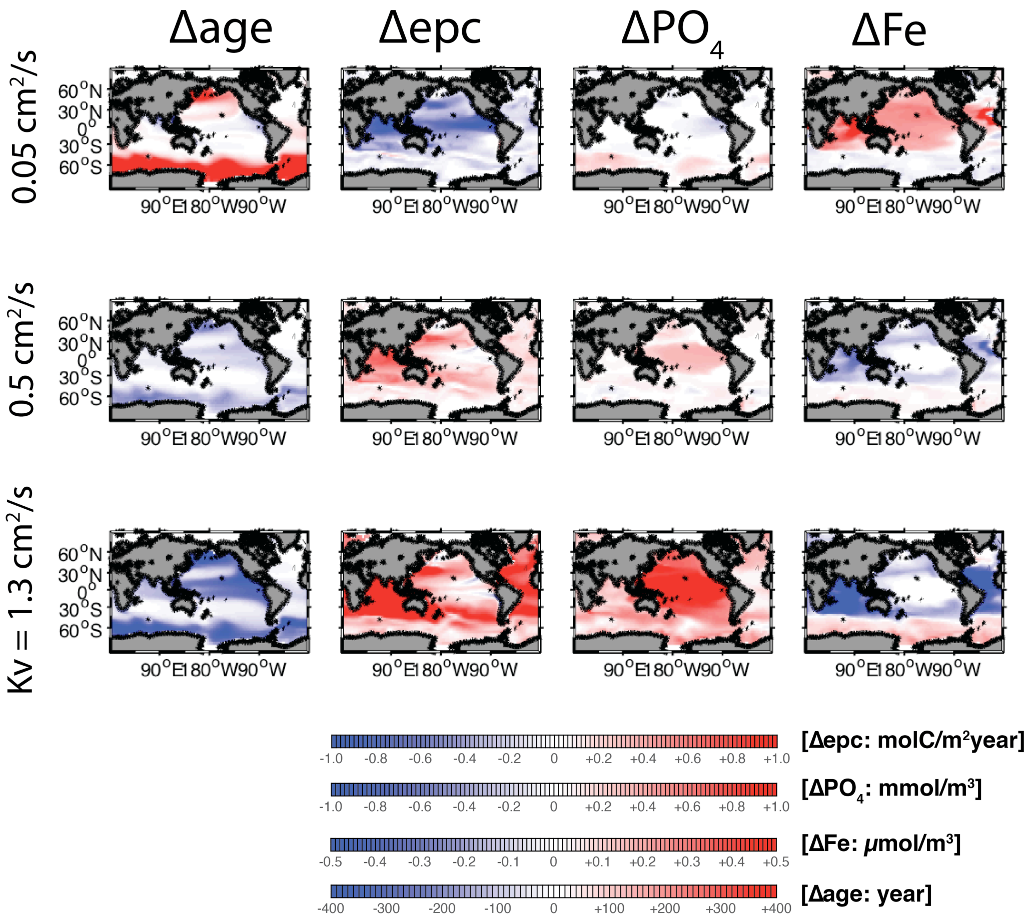

Figure 4.7. The same as in Figure 4.4 except for the thermocline water mass age (*Δage*), export production at 222m (*Δepc*), surface phosphate (*ΔPO_4*), and surface iron (*ΔFe*).

4.5 Summary and implications to global warming response

We examined the role of ventilation and remineralization driven *AOU* in the tropical oceans. Changes in *AOU* plays a crucial role in both the eastern tropical Pacific Ocean and the Indian Ocean but the mechanisms regulating the *AOU* changes are different between two regions. The changes in *AOU* overwhelm the effect of changes in oxygen saturation, regulating the O_2 levels in the tropical oceans. Our sensitivity experiments revealed the importance of iron limitation in the tropical Pacific Ocean, suppressing the effect of reminalization-driven AOU with enhanced vertical mixing.

It is important to note that differences in regional response in *AOU* could also be crucial for understanding the *AOU* changes in the tropical oceans under the anthropogenic climate changes. Previous studies have also indicated that differences in background vertical mixing could lead to different estimates in future projections of O_2 and further more differences in climate sensitivities **[***Duteil and Oschlies*, 2011; *Ross et al.*, 2012]. Additional sensitivity experiments to understand the tropical O_2 and *AOU* response to global warming on top of varying vertical diffusivity could provide us important implications on understanding the uncertainty in future projections from Earth System Model simulations. We need further investigation on combined vertical mixing and warming effects on O_2 evolutions in tropical OMZs.

CHAPTER 5

SUMMARY AND FUTURE WORK

This study aimed to understand the mechanisms behind temporal variability of dissolved oxygen in observations and a hierarchy of models, focusing on two widely different time scales: intra-seasonal variability (i.e. time-scale less than a few month) and centennial transitions associated with anthropogenic climate change. Here we summarize our main results and discuss implications for possible future work.

5.1 What could observations tell us about dissolved oxygen variability?

Recent measurements of physical and biological properties from autonomous platforms provide new opportunities to study high-frequency variability of tracers. In particular autonomous floats can measure oxygen variability associated with meso- and submeso-scale dynamics in the ocean [e.g. *Green et al.*, 2014]. These relatively small-scale and high frequency physics could strongly impact primary production and biogeochemical cycles in the ocean [*Mahadevan*, 2016; *McGillicuddy*, 2016]. In Chapter 2, we analyzed a profiling float deployed in the eastern subpolar North Pacific (in the Gulf of Alaska). We found substantial high-frequency variability for both physical and chemical tracers in the main thermocline at a depth of about 150m, where approximately 80% of this high-frequency variability of observed variability in the main thermocline could be explained by the isopycnal heaving. The observed thermocline tracers exhibit a statistically significant spectral peak of about 1/18 days but this could be produced by the aliasing of the inertial and tidal frequencies. Our results indicated that the likelihood of what appeared to be episodic biogeochemical events could possibly be spurious on the intra-seasonal timescales, thus we must be cautious on analyzing and interpreting the intra-seasonal variability of subsurface tracers based on profiling float. Combining information from physical oceanographic and meteorological observations (e.g. temperature, salinity, mixed layer depth, etc) may provide support for interpreting the signals profiling floats are detecting.

The statistical approach presented in this study could be applicable to other float observations. Increasing biogeochemical observations from the Argo array [e.g., *Riser et al*., 2016] will provide a valuable opportunity to conduct broader, large-scale survey of physical and biogeochemical variability based on the methods we proposed in this research. Recent observations from the Southern Ocean (from the Southern Ocean Carbon and Climate Observations and Modeling (SOCCOM) project; http://soccom.princeton.edu/) could also open a new opportunity to understand the intra-seasonal variability in the polar oceans. Understanding the regional differences in high-frequency tracer variability is an interesting topic. Emerging float datasets, with the aid of regional and process based modeling studies, could reveal underlying physical and biogeochemical processes. Another interesting topic is the further study on the seasonal cycle. To separate the signals of tracer variability, we need a robust understanding on the climatological structure of the seasonal cycle. Detailed structure of seasonal cycle could depend on regions and time period of interest. Revisiting the seasonal cycles based on modern observational data set could be another fruitful topic for better interpretation on float observations.

5.2 Understanding the mechanisms of centennial-scale dissolved oxygen transition in the tropical thermocline

In Chapter 3, we focused on understanding the mechanisms of centennial-scale changes in oceanic oxygen levels, especially focusing on the tropical thermoclines where oxygen minimum zones (OMZs) exist. We used a hierarchy of models to investigate the impact of centennial-scale climate changes on thermocline oxygen levels. Our results highlight the importance of the ocean warming as the leading cause of thermocline oxygen changes. Future projections from state-of-the-art Earth System Models (ESMs) and our simulations exhibit relatively small changes or even an increase in the tropical thermocline oxygen. These changes could be explained by the near-complete compensation between warming-induced solubility and apparent oxygen utilization (*AOU*) decrease. We quantified the effect of physical (i.e. water age) and biological (i.e. remineralization) control on *AOU* from the sensitivity experiments, and found that the two mechanisms equally contribute to the decrease in tropical thermocline *AOU*. Deepening of the isopycnal layers could force lighter and younger water mass down into the thermocline, supplying surface oxygenated water mass into the interior ocean. Warming could also lead to reduce export production (i.e. remineralization) because of the decrease in nutrient supply from the deep ocean. These effects contribute to decrease *AOU* in the tropical thermocline.

To further illustrate the underlying causes of oxygen changes, we performed a suite of sensitivity experiments. A simplified representation of climatic changes was used to force an ocean climate and biogeochemistry model with different patterns of atmospheric and oceanic properties (i.e. sea surface temperature, wind stress, and hydrological cycles) and their influences on the distribution of dissolved oxygen concentrations were studied. The results highlighted the importance of centennial warming effect in altering the oxygen solubility and *AOU*.

There are some caveats about the sensitivity experiments. Coarse resolution ocean model could not fully represent the detailed structures of the equatorial current systems and the effects of ocean eddies and small-scale mixing processes. Future, higher resolution studies are warranted to resolve complex interplay between tropical atmosphere and equatorial ocean dynamics and their role in supplying oxygen and nutrients to the equatorial thermocline [e.g. *Stramma et al*., 2013]. A simple biogeochemical model was used in our sensitivity experiments, which could lead to biases in the representation of export production and remineralization processes. Additional sensitivity experiments using more complicated type of ecosystem models could provide us an additional insight on how these processes responds to centennial-scale climate changes. Wide range of improvements are possible to better represent the biological production, export production of sinking organic materials, and remineralization in an ocean model. Even though the computational power continues to increase it is still necessary to develop efficient parameterization of biological processes suitable for long-term simulations to evaluate climate change impacts on centennial-scale to millennium-scale ocean biogeochemical processes.

Challenges still remain to detect the signals of anthropogenic climate changes from observed biogeochemical tracers because of its limitation in temporal frequency and number of observations we have [*Long et al*., 2016; *Lovenduski et al*., 2015]. Moreover, the observed signals could be more dominated by energetic inter-annual to decadal climate variability. Natural climate variability, such as the El Niño Southern Oscillation (ENSO) and Pacific Decadal Oscillations (PDO) could significantly impact on the tropical thermocline oxygen levels on inter-annual to decadal timescale [*e.g., Deutsch et al.,* 2011*; Ito and Deutsch,* 2013], which makes it challenging to detect the long-term changes from observations [*Long et al.,* 2016]. Some type of sensitivity experiments based on these well known climatic forcing could be an interesting topic to investigate how climate variability impacts on ocean biogeochemical tracers.

5.3 Towards the better understanding on temporal spectrum of oceanic oxygen cycle

State-of-the-art ESMs includes biases on representing the mean state of oxygen, especially in the tropical oceans [*Bopp et al.,* 2013; *Cabré et al*., 2015]. After all, it is still difficult to accurately simulate modern climatological distributions of dissolved oxygen, suggesting that fundamental mechanisms regulating the oceanic oxygen is not yet well represented in ESMs. In Chapter 4, we conducted a suite of sensitivity experiments to better understand the role of ventilation and remineralization regulating the OMZ in the tropical oceans by changing vertical diffusivity in the model. Tropical Pacific Ocean exhibits a unique characteristic regulating the OMZ, which is different from other OMZ regions. Micronutrient limitation of biological productivity could be an important factor controlling the OMZ in the tropical Pacific Ocean. We need to improve the representation of wide range of physical and biogeochemical processes from micro- and macro-nutrient co-limitation of biological productivity to large-scale ocean dynamics.

An interdisciplinary, earth system approach would be necessary in order to fully understand the temporal spectrum of oceanic oxygen and other biogeochemical tracers. Atmospheric climate, ocean dynamics and biogeochemistry are coupled on multiple spatial and temporal scales, challenging to gain integrated understanding of the coupled system by studying individual components in isolation. Collaboration among climate scientists and marine biogeochemists would be fruitful to achieve deeper understanding in the mean state, variability and future projections of ocean biogeochemical systems.

APPENDIX A

DETAILED INFORMATION ON SAMPLING FREQUENCY FROM FLOAT OBSERVATION 5143STNP

This appendix includes detailed information on sampling frequency (time interval) from float observations 5143StnP in Gulf of Alaska. We have plotted Figure A1 to precisely evaluate the aliased inertial and tidal frequencies based on *Wunsch* [1996] formula (equation (2.3) in Chapter 2) using sampling intervals. From the detailed time interval information, we have calculated aliasing inertial and tidal frequencies based on the statistics (mean) sampling time interval shown here.

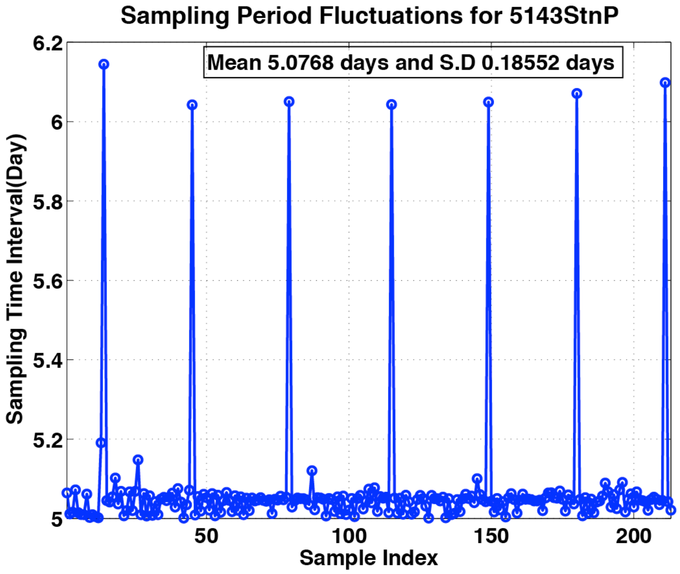

Figure A1. The observational sampling time interval for float 5143StnP deployed in the Gulf of Alaska.

REFERENCES

Amante, C. and B. W. Eakins (2009), ETOPO1 1 Arc-Minute Global Relief Model: Procedures, Data Sources and Analysis. NOAA Technical Memorandum NESDIS NGDC-24, 19 pp

Behrenfeld, M. J. and P. G. Falkowski (1997), Photosynthetic rates derived from satellite-based chlorophyll concentration, *Limnol. Oceanogr*., 42. 1-20.

Bianchi, D., J. P. Dunne, J. L. Sarmiento, and E. D. Galbraith (2012), Data-based estimates of suboxia, denitrification, and N_2O production in the ocean and their sensitivities to dissolved O_2, *Global Biogeochem. Cycles*, 26, GB2009, doi:10.1029/2011GB004209.

Bishop J. K. B. (2009), Autonomous Observations of the Ocean Biological Carbon Pump. *Oceanography, 22* (2). 182-193.

Bopp, L., et al. (2013), Multiple stressors of ocean ecosystems in the 21st century: projections with CMIP5 models, *Biogeosciences*, *10*(10), 6225-6245.

Boyer, T. P., et al. (2014), 2013 World Ocean Atlas Aids High‐Resolution Climate Studies, *Eos, Transactions American Geophysical Union*, *95*(41), 369-370.

Bretherton, C. S., M. Widmann, V. P. Dymnikov, J. M. Wallace, and I. Blade, (1999), The effective number of spatial degrees of freedom of a time-varying field. *J. Climate, 12,* 1990–2009.

Broecker, W. S., (1974), Chemical Oceanography, Harcourt Brace Jovanovich, New York, U.S.A.

Broecker, W. S. and T. H. Peng (1982), Tracers in the Sea, Lamont-Doherty Earth Observatory, Palisades, N. Y., U.S.A.

Bryan, K., and Lewis, L. J. (1979). A water mass model of the world ocean. *Journal of Geophysical Research: Oceans*, *84*(C5), 2503-2517.

Cabré, A., I. Marinov, R. Bernardello, and D. Bianchi (2015), Oxygen minimum zones in the tropical Pacific across CMIP5 models: mean state differences and climate change trends, *Biogeosciences*, *12*(18), 5429-5454.

Capotondi, A., M. A. Alexander, C. Deser, and A. J. Miller (2005), Low-frequency pycnocline variability in the northeast Pacific, *J. Phys.Oceanogr., 35*, 1403–1420.

Capotondi, A., M. A. Alexander, N. A. Bond, E. N. Curchitser, and J. D. Scott (2012), Enhanced upper ocean stratification with climate change in the CMIP3 models, *J. Geophys. Res.*, 117, C04031, doi:10.1029/2011JC007409.

Cocco, V., et al. (2013), Oxygen and indicators of stress for marine life in multi-model global warming projections, *Biogeosciences*, *10*(3), 1849-1868.

Codispoti, L. A. (1995), Biogeochemical Cycles - Is the Ocean Losing Nitrate, *Nature*, *376*(6543), 724-724.

Codispoti, L. A., J. A. Brandes, J. P. Christensen, A. H. Devol, S. W. A. Naqvi, H. W. Paerl, and T. Yoshinari (2001), The oceanic fixed nitrogen and nitrous oxide budgets: Moving targets as we enter the anthropocene?, *Scientia Marina*, *65*, 85-105.

Collins, W. J., et al. (2011), Development and evaluation of an Earth-System model - HadGEM2, *Geosci. Model Dev.*, 4(4), 1051–1075, doi:10.5194/gmd-4-1051-2011.

Cummins, P. F., and G. S. E. Lagerloef (2002), Low-frequency pycnocline depth variability at Ocean Weather Station P in the northeast Pacific, *J. Phys. Oceanogr., 32*, 3207–3215

Cummins, P. F., and D. Masson (2012), Wind-driven variability of dissolved oxygen below the mixed layer at Station P, *J. Geophys. Res., 117*, C08015, doi:10.1029/2011JC007847.

Czeschel, R., L. Stramma, and G. C. Johnson (2012), Oxygen decreases and variability in the eastern equatorial Pacific, *Journal of Geophysical Research: Oceans*, *117*(C11), C11019.

de Boyer Montégut, C., G. Madec, A. S. Fischer, A. Lazar, and D. Iudicone (2004), Mixed layer depth over the global ocean: an examination of profile data and a profile-based climatology, *J. Geophys. Res., 109*, C12003.

de Lavergne, C., Palter, J. B., Galbraith, E. D., Bernardello, R., & Marinov, I. (2014), Cessation of deep convection in the open Southern Ocean under anthropogenic climate change, *Nat. Clim. Change*, *4*(4), 278-282.

Deutsch, C., Brix, H., Ito, T., Frenzel, H., and Thompson, L. (2011), Climate-forced variability of ocean hypoxia, *Science*, *333*(6040), 336-339.

Deutsch, C., Emerson, S., and Thompson, L. (2006), Physical-biological interactions in North Pacific oxygen variability, *J. Geophys. Res., 111*(C9), 1-16.

Deutsch, C., et al. (2014), Centennial changes in North Pacific anoxia linked to tropical trade winds. *Science*, *345*(6197), 665-668.

Deutsch, C., Ferrel, A., Seibel, B., Pörtner, H. O., and Huey, R. B. (2015), Climate change tightens a metabolic constraint on marine habitats, *Science*, *348*(6239), 1132-1135.

Dore, J. E., Lukas, R., Sadler, D. W., Church, M. J., and Karl, D. M. (2009), Physical and biogeochemical modulation of ocean acidification in the central North Pacific, *Proc. Natl. Acad. Sci. U.S.A.*, 106(30), 12235-12240.

Dufresne, J. L., et al. (2013), Climate change projections using the IPSL-CM5 Earth System Model: From CMIP3 to CMIP5, *Clim. Dyn.*, 40(9–10), 2123–2165, doi:10.1007/s00382-012-1636-1.

Dunne, J. P., et al. (2012), GFDL's ESM2 global coupled climate–Carbon Earth System Models. Part II: Carbon system formulation and baseline simulation characteristics, *J. Clim.*, 26(7), 2247–2267, doi:10.1175/JCLI-D-12-00150.1.

Duteil, O., Koeve, W., Oschlies, A., Bianchi, D., Galbraith, E., Kriest, I., and Matear, R.: A novel estimate of ocean oxygen utilisation points to a reduced rate of respiration in the ocean interior, *Biogeosciences*, 10, 7723-7738, doi:10.5194/bg-10-7723-2013, 2013.

Duteil, O., and A. Oschlies (2011), Sensitivity of simulated extent and future evolution of marine suboxia to mixing intensity, *Geophys. Res.* Lett., 38, L06607, doi:10.1029/2011GL046877.

Dutkiewicz, S., Sokolov, A. P., Scott, J., and Stone, P. H. (2005). A three-dimensional ocean-seaice-carbon cycle model and its coupling to a two-dimensional atmospheric model: uses in climate change studies, Report 122, Joint Program of the Science and Policy of Global Change, M.I.T., Cambridge, MA.

Emerson, S. R., and Bushinsky, S. (2014), Oxygen concentrations and biological fluxes in the open ocean, *Oceanography*, *27*(1), 168-171.

Emerson, S. R., and Hedges, J. I. (2008), Chemical Oceanography and the Marine Carbon Cycle, Cambridge Univ Press, Cambridge, U. K.

Emerson, S., Stump, C., and Nicholson, D. (2008), Net biological oxygen production in the ocean: Remote in situ measurements of O_2 and N_2 in surface waters, *Global Biogeochem. Cycles*, 22, GB3023, doi:10.1029/2007GB003095.

Garcia, H. E., and Gordon, L. I. (1992), Oxygen solubility in seawater: Better fitting equations, *Limnol. Oceanogr*, *37*(6), 1307-1312.

Garcia, H. E., R. A. Locarnini, T. P. Boyer, J. I. Antonov, O. K. Baranova, M. M. Zweng, and D. R. Johnson, (2010), World Ocean Atlas 2009, Volume 3: Dissolved Oxygen, Apparent Oxygen Utilization, and Oxygen Saturation. S. Levitus, Ed. NOAA Atlas NESDIS 70, U.S. Government Printing Office, Washington, D.C., 344 pp.

Gent, P. R., and J. C. McWilliams (1990), Isopycnal Mixing in Ocean Circulation Models, *J Phys Oceanogr*, 20(1), 150-155.

Gillett, N. P., and J. C. Fyfe (2013), Annular mode changes in the CMIP5 simulations, *Geophys. Res. Lett.*, 40, 1189–1193, doi:10.1002/grl.50249.

Gilman, D. L., F. J. Fuglister, J. M. Mitchell, (1963), On the Power Spectrum of "Red Noise", *J. Atmos. Sci., 20,* 182–184.

Giorgetta, M. A., et al. (2013), Climate and carbon cycle changes from 1850 to 2100 in MPI-ESM simulations for the Coupled Model Intercomparison Project phase 5, *J. Adv. Model. Earth Syst.*, 5, 572–597, doi:10.1002/jame.20038.

Gnanadesikan, A., Russell, J. L., and Zeng, F. (2007), How does ocean ventilation change under global warming?, *Ocean Science*, 3(1), 43-53.

Gnanadesikan, A., J. P. Dunne, and J. John (2012), Understanding why the volume of suboxic waters does not increase over centuries of global warming in an Earth System Model, *Biogeosciences*, *9*(3), 1159-1172.

Green, R. E., Bower, A. S., and Lugo-Fernández, A. (2014). First autonomous bio-optical profiling float in the Gulf of Mexico reveals dynamic biogeochemistry in deep waters. *PloS one*, *9*(7), e101658.

Gruber, N. (2011), Warming up, turning sour, losing breath: Ocean bio- geochemistry under global change, *Philos. Trans. R. Soc. A*, 369, 1980–1996, doi:10.1098/rsta.2011.0003.

Hanawa, K, and Talley L. D. (2001), Mode Waters, Ocean Circulation and Climate: observing and modelling the global ocean, Siedler G, Church J, Gould WJ, Eds., :373-386., San Diego, Calif. London: Academic

Held, I. M., and Soden, B. J. (2006), Robust responses of the hydrological cycle to global warming, *J. Clim.*, 19(21), 5686-5699.

Helm, K. P., Bindoff, N. L., and Church, J. A. (2011). Observed decreases in oxygen content of the global ocean. *Geophys. Res. Lett.,* 38*, L23602, doi:*10.1029/2011GL049513.

Ito, T., A. Bracco, C. Deutsch, H. Frenzel, M. Long, and Y. Takano (2015), Sustained growth of the Southern Ocean carbon storage in a warming climate, *Geophys Res Lett*, *42*(11), 4516-4522.

Ito, T., and C. Deutsch (2010), A conceptual model for the temporal spectrum of oceanic oxygen variability, *Geophys. Res. Lett*., 37, L03601, doi:10.1029/2009GL041595.

Ito, T., and C. Deutsch (2013), Variability of the oxygen minimum zone in the tropical North Pacific during the late twentieth century, *Global Biogeochem. Cycles*, *27*(4), 1119-1128.

Ito, T., M. J. Follows, and E. A. Boyle (2004), Is AOU a good measure of respiration in the oceans? *Geophys. Res. Lett*., 31, L17305, doi:10.1029/2004GL020900.

Ito, T., and M. J. Follows (2005), Preformed phosphate, soft tissue pump and atmospheric CO2, *Journal of Marine Research*, 63(4), 813-839, doi:10.1357/0022240054663231.

Iwasaka, N., F. Kobashi, Y. Kinoshita, and Y. Ohno (2006), Seasonal variations of the upper ocean in the western north pacific observed by an argo float, *J. Ocean., 62*(4), 481–492, doi:10.1007/s10872-006-0070-6.

Jiang, S., P. H. Stone, and P. Malanotte-Rizzoli (1999), An assessment of the Geophysical Fluid Dynamics Laboratory ocean model with coarse resolution: Annual-mean climatology, *J Geophys Res-Oceans*, 104(C11), 25623-25645, doi:10.1029/1999jc900095.

Johnson, K.S., L.J. Coletti, H.W. Jannasch, C.M. Sakamoto, D.D Swift, and S.C. Riser. (2013). Long-term nitrate measurements in the ocean using the In Situ Ultraviolet Spectrophotometer: sensor integration into the Apex profiling float, *J. Atmos. Ocean. Technol., 30,* 1854–1866.

Johnson, K. S., S. C. Riser, and D. M. Karl (2010), Nitrate supply from deep to near-surface waters of the North Pacific subtropical gyre, *Nature, 465*(7301), 1062-1065.

Johnson, K.S., W.M. Berelson, E.S. Boss, Z. Chase, H. Claustre, S.R. Emerson, N. Gruber, A. Körtzinger, M.J. Perry, and S.C. Riser. (2009). Observing biogeochemical cycles at global scales with profiling floats and gliders: Prospects for a global array. *Oceanography 22*(3):216–225, http://dx.doi.org/10.5670/oceanog.2009.81.

Johnson, K.S., and L.J. Coletti (2002), In situ ultraviolet spectrophotometry for high resolution and long-term monitoring of nitrate, bromide and bisulfide in the ocean, *Deep-Sea Research Part I-Oceanographic Research Papers, 49,*1291-1305.

Kalnay, E., et al. (1996), The NCEP/NCAR 40-year reanalysis project, *Bulletin of the American meteorological Society*, 77(3), 437-471.

Karstensen, J., Stramma, L., and Visbeck, M. (2008), Oxygen minimum zones in the eastern tropical Atlantic and Pacific oceans, *Prog. Oceanogr*, 77(4), 331-350.

Keeling, R.F., Körtzinger A., and Gruber, N. (2010), Ocean deoxygenation in a warming world, *Annu. Rev. Mar. Sci.*, 2, pp. 199–229

Körtzinger, A., J. Schimanski, and U. Send (2005), High quality oxygen measurements from profiling floats: A promising new technique, *J. Atmos. Ocean. Technol., 22(*3), 302-308.

Large, W. G., J. C. Mcwilliams, and S. C. Doney (1994), Oceanic Vertical Mixing - a Review and a Model with a Nonlocal Boundary-Layer Parameterization, *Rev Geophys*, 32(4), 363-403, doi:Doi 10.1029/94rg01872.

Levitus, S., R. Burgett, T. Boyer (1994a), World Ocean Atlas 1994, Vol. 3: Salinity. NOAA Atlas NESDIS 3,U.S. Gov. Printing Office, Wash., D.C., 99 pp.

Levitus, S., T. Boyer (1994b), World Ocean Atlas 1994, Vol. 4: Temperature. NOAA Atlas NESDIS 4, U.S. Gov. Printing Office, Wash., D.C., 117 pp.

Long, M. C., C. Deutsch, and T. Ito (2016), Finding forced trends in oceanic oxygen, *Global Biogeochem. Cycles*., 30, doi:10.1002/2015GB005310.

Lovenduski, N. S., A. R. Fay, and G. A. McKinley (2015), Observing multidecadal trends in Southern Ocean CO2 uptake: What can we learn from an ocean model?, *Global Biogeochem. Cycles*, 29, 416–426, doi: 10.1002/2014GB004933.

Luyten, J. R., Pedlosky, J., and Stommel, H. (1983), The ventilated thermocline, *Journal of Physical Oceanography*, 13(2), 292-309.

Mahadevan, A., (2016), The Impact of Submesoscale Physics on Primary Productivity of Plankton, *Annu. Rev. Mar. Sci.*, *8*, 161-184.

Mahadevan, A., E. D'Asaro, C. Lee, and M.J. Perry (2012), Eddy-driven stratification initiates North Atlantic spring phytoplankton blooms, *Science, 337*, 6090, pp.54-58.

Marshall, G. J. (2003), Trends in the Southern Annular Mode from observations and reanalyses, *J. Clim.*, 16(24), 4134-4143.

Marshall, J., A. Adcroft, C. Hill, L. Perelman, and C. Heisey (1997a), A finite-volume, incompressible Navier Stokes model for studies of the ocean on parallel computers, *J Geophys Res-Oceans*, 102(C3), 5753-5766, doi:Doi 10.1029/96jc02775.

Marshall, J., C. Hill, L. Perelman, and A. Adcroft (1997b), Hydrostatic, quasi-hydrostatic, and nonhydrostatic ocean modeling, *J Geophys Res-Oceans*, 102(C3), 5733-5752, doi: 10.1029/96jc02776.

Matear, R. J., and A. C. Hirst (2003), Long-term changes in dissolved oxygen concentrations in the ocean caused by protracted global warming, *Global Biogeochem. Cycles*, 17, 1125, doi:10.1029/2002GB001997, 4.

McGillicuddy, D.J., (2016), Mechanisms of physical-biological-biogeochemical interaction at the oceanic mesoscale, *Annu. Rev. Mar. Sci*, 8, 125-159

McGillicuddy, D. J., L. A. Anderson, S. C. Doney, and M. E. Maltrud (2003), Eddy-driven sources and sinks of nutrients in the upper ocean: Results from a 0.1 degrees resolution model of the North Atlantic, *Global Biogeochem. Cycles, 17*(2), 1035, doi:10.1029/2002GB001987..

McGillicuddy, D. J., A. R. Robinson, D. A. Siegel, H. W. Jannasch, R. Johnson, T. Dickeys, J. McNeil, A. F. Michaels, and A. H. Knap (1998), Influence of mesoscale eddies on new production in the Sargasso Sea, *Nature, 394*(6690), 263-266.

Meinshausen, M., et al. (2011), The RCP greenhouse gas concentrations and their extensions from 1765 to 2300, *Climatic Change*, 109(1-2), 213-241.

Moore, J. K., K. Lindsay, S. C. Doney, M. C. Long, and K. Misumi (2013), Marine Ecosystem Dynamics and Biogeochemical Cycling in the Community Earth System Model [CESM1(BGC)]: Comparison of the 1990s with the 2090s under the RCP4.5 and RCP8.5 scenarios, *J. Clim.*, 26(23), 9291–9312, doi:10.1175/JCLI-D-12-00566.1.

Morel, F. M. M., and Price, N. M. (2003),The biogeochemical cycles of trace metals in the oceans, *Science*, *300*(5621), 944-947, doi:10.1126/science.1083545.

Nicholson, D., S. Emerson, and C. C. Eriksen (2008), Net community production in the deep euphotic zone of the subtropical North Pacific gyre from glider surveys, *Limnol. Oceanogr., 53*(5), 2226-2236.

Oschlies, A., K. G. Shulz, U. Riebesell, and A. Schmittner (2008), Simulated 21st century's increase in oceanic suboxia by CO2-enhanced biotic carbon export, *Global Biogeochem. Cycles*, 22, GB4008, doi:10.1029/2007GB003147.

Ono, T., T. Midorikawa, Y. W. Watanabe, K. Tadokoro, and T. Saino (2001), Temporal increases of phosphate and apparent oxygen utilization in the subsurface waters of western subarctic Pacific from 1968 to 1998, *Geophys. Res. Lett., 28*(17), 3285–3288, doi:10.1029/2001GL012948.

Parekh, P., Follows, M. J., and Boyle, E. A. (2005). Decoupling of iron and phosphate in the global ocean. *Global Biogeochem. Cycles*, 19(2).

Pytkowicz, R. M. (1971). On the apparent oxygen utilization and the preformed phosphate in the oceans. *Limnol. Oceanogr*, *16*(1), 39-42.

Pörtner, H. O., and Knust, R. (2007), Climate change affects marine fishes through the oxygen limitation of thermal tolerance, *Science*, *315*(5808), 95-97, doi:10.1126/science.1135471.

Ravichandran, M., M. Girishkumar, and S. Riser (2012), Observed variability in chlorophyll-a using profiling floats in the southwestern Arabian Sea. *Deep-Sea Research Part I Oceanographic Research Papers, 65*, 15-25.

Redfield, A. C. (1958), The biological control of chemical factors in the environment. *American Scientist*, *46*(3), 230A-221.

Redi, M. H. (1982), Oceanic isopycnal mixing by coordinate rotation, *J Phys Oceanogr*, 12(10), 1154-1158.

Ridder, N. N., and England, M. H. (2014), Sensitivity of ocean oxygenation to variations in tropical zonal wind stress magnitude, *Global Biogeochem. Cycles*, 28(9), 909-926.

Riser, S. C., et al. (2016), Fifteen years of ocean observations with the global Argo array, *Nature Climate Change*, *6*(2), 145-153.

Riser, S. C., and K. S. Johnson (2008), Net production of oxygen in the subtropical ocean, *Nature, 451*(7176), 323-U325.

Roemmich, D., S. Riser, R. Davis, and Y. Desaubies (2004), Autonomous profiling floats: Workhorse for broad-scale ocean observations, *Mar. Technol. Soc. J., 38*(2), 21-29.

Ross, A., Matthews, H. D., Schmittner, A., and Kothavala, Z. (2012), Assessing the effects of ocean diffusivity and climate sensitivity on the rate of global climate change, *Tellus B*, 64.

Sakamoto, C. M., K. S. Johnson, and L. J. Coletti (2009), Improved algorithm for the computation of nitrate concentrations in seawater using an in situ ultraviolet spectrophotometer, *Limnol. Oceanogr. Meth., 7*, 132-143.

Schlesinger, W. H., and E. S. Bernhardt (2013), Biogeochemistry: An Analysis of Global Change, 3rd ed., Academic Press, Waltham, Mass, U.S.A.

Schneider, T., P. A. O'Gorman, and X. J. Levine (2010), Water vapor and the dynamics of climate changes, *Rev. Geophys.*, 48, RG3001, doi:10.1029/2009RG000302.

Seibel, B. A. (2010), Critical oxygen levels and metabolic suppression in oceanic oxygen minimum zones, *Journal of Experimental Biology*, *214*(2), 326-336.

Stramma, L., Bange, H. W., Czeschel, R., Lorenzo, A., and Frank, M. (2013). On the role of mesoscale eddies for the biological productivity and biogeochemistry in the eastern tropical Pacific Ocean off Peru. *Biogeosciences*, *10*(11), 7293-7306.

Stramma, L., G. C. Johnson, J. Sprintall, and V. Mohrholz (2008), Expanding oxygen-minimum zones in the tropical oceans, *Science*, 320(5876), 655–658, doi:10.1126/science.1153847.

Suga, T., Y. Takei, and Hanawa, K. (1997), Thermostad Distribution in the North Pacific Subtropical Gyre: The Central Mode Water and the Subtropical Mode Water, *J. Phys. Oceanogr.*, 27, 140–152.

Sverdrup, H. U., (1938), On the explanation of the oxygen minima and maxima in the oceans, *J. Cons. Int. Bxplor. Mer.*, 13, 163-172.

Taylor, J. R. and R. Ferrari (2011), Ocean fronts trigger high latitude phytoplankton blooms, *Geophys. Res. Lett., 38*, L23601, doi:10.1029/2011GL049312.

Taylor, K. E., Stouffer, R. J., and Meehl, G. A. (2012), An overview of CMIP5 and the experiment design, *Bulletin of the American Meteorological Society*, *93*(4), 485-498.

Talley, L. D., G. L. Pickard, W. J. Emery, and J. H. Swift (2011), Descriptive Physical Oceanography: An Introduction, 6th ed., 560 pp., Elsevier, Boston, U.S.A.

Thompson, D. W., Wallace, J. M., and Hegerl, G. C. (2000), Annular modes in the extratropical circulation, Part II: Trends. *J. Clim.*, 13(5), 1018-1036.

Tokinaga, H., Xie, S. P., Deser, C., Kosaka, Y., and Okumura, Y. M. (2012), Slowdown of the Walker circulation driven by tropical Indo-Pacific warming, *Nature*, *491*(7424), 439-443.

Trenberth, K., J. Olson, and W. Large, (1989), A global wind stress climatology based on ECMWF analyses, Tech. Rep. NCAR/TN-338+STR, National Center for Atmospheric Research, Boulder, Colorado.

Vallis, G. K., Zurita-Gotor, P., Cairns, C. and Kidston, J. (2015), Response of the large-scale structure of the atmosphere to global warming. *Q.J.R. Meteorol. Soc.*, 141: 1479–1501. doi: 10.1002/qj.2456

Vaquer-Sunyer, R., and Duarte, C. M. (2008), Thresholds of hypoxia for marine biodiversity, *Proc. Natl. Acad. Sci. U.S.A.*, *105*(40), 15452-15457.

Vecchi, G. A., Soden, B. J., Wittenberg, A. T., Held, I. M., Leetmaa, A., and Harrison, M. J. (2006). Weakening of tropical Pacific atmospheric circulation due to anthropogenic forcing. *Nature*, 441(7089), 73-76.

Watanabe, Y. W., M. Shigemitsu, and K. Tadokoro (2008), Evidence of a change in oceanic fixed nitrogen with decadal climate change in the North Pacific subpolar region, *Geophys. Res. Lett.*, 35, L01602, doi:10.1029/2007GL032188.

White, W. B., and S. Tabata (1987), Interannual Westward-Propagating Baroclinic Long-Wave Activity on Line P in the Eastern Midlatitude North Pacific, *J. Phys. Ocean., 17*(3), 385–396, doi:10.1175/1520-0485(1987)017<0385:IWPBLW>2.0.CO;2.

Whitney, F. A., H. J. Freeland, and M. Robert (2007), Persistently declining oxygen levels in the interior waters of the eastern subarctic Pacific, *Prog. Oceanogr.*, 75(2), 179–199, doi:10.1016/j.pocean.2007.08.007.

Williams, R. G., and M. J. Follows (2011), Ocean Dynamics and the Carbon Cycle: Principles and Mechanisms, 404 pp., Cambridge Univ. Press, Cambridge, U. K.

Wunsch. C (1996), The Ocean Circulation Inverse Problem, Cambridge University Press, Cambridge, U.K.

Wyrtki, K. (1962), The oxygen minima in relation to ocean circulation, *Deep Sea Res.*, 9, 11–23, doi:10.1016/0011-7471(62)90243-7.

Xu, L., Xie, S. P., Liu, Q., and Kobashi, F. (2012), Response of the North Pacific subtropical countercurrent and its variability to global warming, *Journal of Oceanography*, 68(1), 127.